Mechanochemically alloyed Si-TM (TM=Fe, Cr) and Quantitative Composition Determination by Mössbauer Spectroscopy

By

Benjamin Scott

Submitted in partial fulfilment of the requirements
for the degree of Master of Science

at

Dalhousie University
Halifax, Nova Scotia
March 2020

Table of Contents

List of Tables

List of Figures

Abstract

Si as a negative electrode material in Li-on batteries has garnered considerable research interest because of its volumetric capacity, thermal stability, and relative low cost[1]. However, because Si does not store Li via an intercalation mechanism, rather by an .alloying mechanism; Li storage in Si results in a volume expansion of up to 280%.[2] Such large volume expansions are detrimental to cell cycling,[3,4] and therefore must be limited to some tolerable amount.

One method of limiting volume expansion is by alloying Si with a transition metal (TM) forming an inert TM silicide, effectively reducing the amount of active Si; therefore, reducing the total volume expansion.[1] Fe, because of its abundance in the earth's crust and relative low cost, is an ideal candidate. Cr was additionally explored as the mechanical properties of Cr are different than those of Fe. SiTM alloys were generated by a commercially relevant mechanochemical synthesis and evaluated in Li metal half cells.

It was found that in the case of Fe, the mechanochemical reaction was complete after 4 hours when evaluated by XRD and Mössbauer spectroscopy. However, it was found that further milling was required to achieve improved cycling performance when evaluated in Li-metal half cells. Following 16 hours of milling a $Si_{85}Fe_{15}$ alloy was found to cycle at a reversible capacity of 1428 Ah/L, with an irreversible capacity of 488 Ah/L (25.4%) and a capacity retention of 83.7% after 100 charge discharge cycles. In the case of Cr it was found that the mechanochemical reaction did not reach completion even after 16 hours of milling and some metallic Cr remained. Cycling performance of Si-Cr alloys was poor as compared to Fe. There was additionally evidence that Cr may be catalytically reducing electrolyte as increases in polarization and impedance as a function of cycle number were observed.

A method for quantitative determination of the Fe content of powders by Mössbauer spectroscopy was then described. In this method, powder samples and an internal standard are combined homogeneously in a plastic film. This method was verified by using Mössbauer Spectroscopy to quantify the Fe content of a series of mixtures of iron (III) citrate diluted by calcium acetate. These results were additionally confirmed by ICP-OES. The method was then used to determine for the first time the amount of Fe contamination in ball milled Si as a function of milling time. It was found that the amount of Fe contamination increased with time, but surprisingly became steady-state at 1.12 ± 0.04 at. % Fe. Fe content was then evaluated in two series of ball milled Si-TM alloys (TM = V, Cr) as a function milling time. When compared to Si precursor milled alone, the addition of a TM was found to roughly double Fe contamination. A number of ball milled Si-TM alloys (TM = V, Cr, Ni, Ti) were subject to Fe content determination by Mössbauer spectroscopy to determine which Si-TM alloy resulted in the lowest Fe contamination from milling tools. It was found that Ti introduced the least Fe contamination at 0.75±0.02 at. % Fe after 16 hours of high energy ball milling.

List of Abbreviations Used

CMC	Carboxy Methyl Cellulose
EFG	Electric Field Gradient
LIB	Lithium-ion Battery
LP	Lorentz Polarization
MCA	Multi-Channel Analyser
PHES	Pumped Hydro Energy Storage
PVDF	Polyvinylidene Fluoride
SBR	Styrene-Butadiene Rubber
SCA	Single-channel Analyser
TEM-SAED	Transmission Electron Microscopy Selected Area Electron Diffraction
V2G	Vehicle to Grid
XRD	X-Ray Diffraction

Acknowledgements

I would like to firs acknowledge Dr. Mark Obrovac, for continued support and always pointing me in the right direction. I would like to also thank my examining committee, Dr. Mita Dasog and Dr. Michael Freund, for taking the time to consider and evaluate my work.

I would like to thank Tim Hatchard for support and training with all equipment within our lab. I would also like to thank Alisha Oickle for help with ICP-OES, and Rich Dunlap for help with Mössbauer spectrometers and interpreting Mössbauer spectra.

I would also like to thank all members of the Obrovac lab. First and Foremost, Clarke Brown who worked with me as a summer student. I would like to thank those who helped me with lab equipment and data analysis who were, in the order they have sat around the office clockwise from the door, Yidan Cao, Scott Young, Simeng Cao Jun Wang, Ryan Fielden, Lituo Zhang, Roy (Leyi) Zhao, Conxiao Wei, Zilai Yan, Leo (Yukun) Wang, Annie (Yija) Liu, Michael Charlton, Rebecca Boyd, and Haonan Yu. In addition to our lab I would also like to thank Chelsi Wicks and Steve Driscoll insight on data analysis using Matlab and continued help debugging code.

Finally I would like to thank my friends and family, and last but not least my dog Ripley.

Chapter 1 **Introduction**

The discussion of global warming, CO_2 emissions, and renewable energy sources, have, in recent times, become popular topics of household conversation as a result of increasing global temperature and depleting fossil fuel resources. As the energy required by todays society is continually increasing, it is predicted that the rate of energy production must increase by ~30% in the next 20 years (by 2040), and must be done without increasing CO_2 production or relying on finite fossil-fuel resources provided atmospheric carbon cannot be sequestered to maintain net-zero carbon emissions.[5] This has made harvesting energy from renewable resources a global imperative; and, because of the intermittent nature of renewable energy (wind, solar, tidal) the matter of energy storage has additionally become increasingly important. Energy storage not only enables continuous energy supply from intermittent renewable energy sources; but, can also allow load leveling. Energy can be stored during night time hours when energy consumption is at a minimum in order to compensate for day time hours when energy consumption is at a maximum; energy production, therefore, remains constant improving grid reliability, stability, and cost.[6]

Currently ~99% of energy stored globally is stored via pumped hydro energy storage (PHES).[6–8] Water is pumped from a lower reservoir to an upper reservoir therefore storing electrical energy as potential energy. PHES currently dominates grid energy storage because it is cost effective, efficient (71%-85%) and has a lifetime of ~30 years.[9,10] PHES is, however, limited by geological and geographic specifications,[7,11] therefore, in order to accommodate increasing renewable energy resources alternative energy storage methods must be applied.

The lithium-ion battery (LIB) was commercialized by Sony in 1991, and, because of the massive increase in energy density relative battery technology of the time,[12,13] has grown to monopolize energy storage for the portable electronics, electric vehicle, and plug-in hybrid-electric vehicle markets. This is shown in Figure 1.1 which serves as a relative comparison of commercial battery technology. LIBs have, however, been limited to applications where energy density is paramount because of their relatively high cost and limited lifetime (5-10 years).[9] Large-scale stationary energy storage devices favor less energy dense, but more cost-effective energy storage technologies. This, however, does not completely rule out the use of LIBs for grid energy storage.

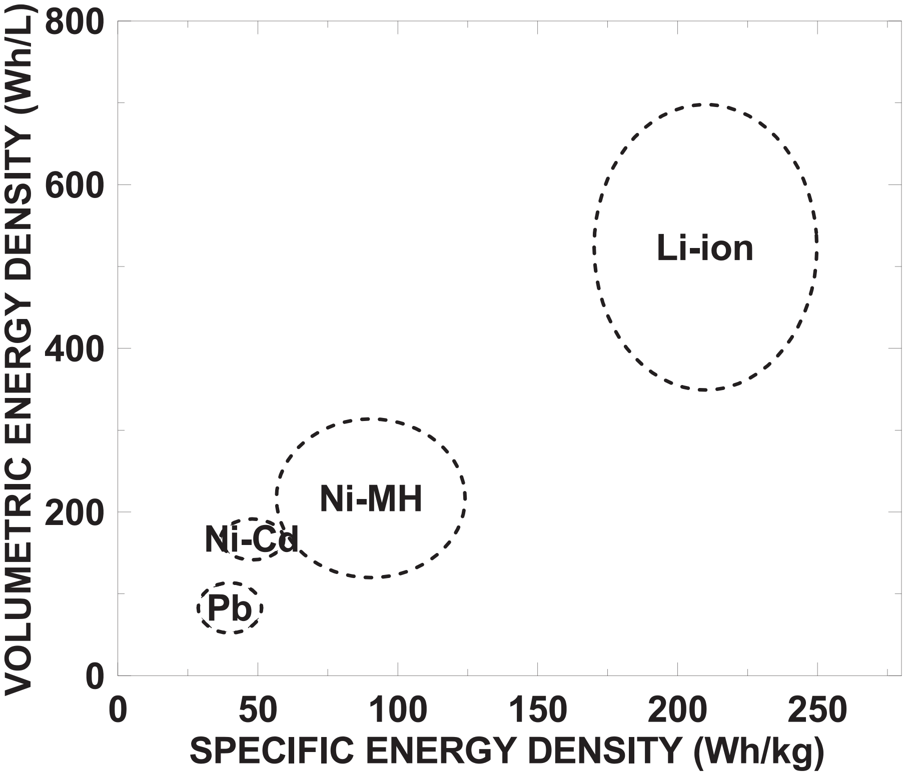

Figure 1.1 Plot of specific and volumetric energy density ranges for different battery technologies; data taken from reference 14.

Considering the widespread proposals to ban the sale of fossil fuel burning vehicles by cities and countries around the world (In the case of the City of Vancouver, they have set a goal of 100% renewable powered transportation by 2050[15]); and, given that LIBs are the prime energy storage technology for electric vehicles, a large fleet of non-stationary LIBs could potentially become available in the near future for vehicle to grid (V2G) energy storage.

Bidirectional V2G energy storage relies on batteries in electric and plug-in hybrid electric vehicles supplying energy to the grid during peak hours; and, vehicle batteries being charged during off-peak hours.[16,17] Additionally, in an ideal system, vehicle batteries would be used to store renewable energy, especially in the case of wind energy where the intermittent nature is considerably less predictable than solar or tidal energy. It has been shown that the use of V2G energy storage could increase the penetration of wind energy from 41% to 59%.[18]

As an example, in the case of Nova Scotia, Canada; the energy generation capacity by electric utilities is currently 2488 MW;[19] comparing this to the fleet of light vehicles, the 2016 census reported 310240 light vehicles commuting to their place of employment daily.[20] If one quarter of the fleet were electric vehicles with a 15 KW battery installed, the total capacity would be 1163 MW. This is roughly equivalent to the daily peak load,[21] and roughly one half the total generation capacity. Therefore, in the event that LIBs are too expensive for stationary grid energy storage and less energy dense methods are employed, given the requirement for energy dense LIBs in electric and plug-in hybrid electric vehicles and the proposed shift to ban the sale of fossil fuel burning vehicles, there is a likely scenario where V2G energy storage could comprise a large portion of grid energy storage as well as renewable energy storage. LIBs then, are important not only for electrified vehicles but could play a very important role in grid energy storage.

1.1 Lithium-ion Battery Chemistry

An electrochemical cell relies on redox reactions in order to convert chemical energy to electrical energy. In a metal-ion cell difference in the chemical potential of reduction and oxidation reactions results in the oxidation of a chemical species at the negative electrode (oxidation, $A \rightarrow A^+ + e^-$) Electrons are transferred through an external circuit while a positive counter-ion travels through electrolyte solution (from negative to positive electrode) maintaining charge neutrality. After passing through the external circuit the electron arrives at the cathode where a reduction reaction occurs (reduction, $C^+ + e^- \rightarrow C$).

A lithium-ion battery relies on the difference in the chemical potentials of lithium in one host structure versus another host structure. Batteries of this type can be described as “rocking chair” batteries; lithium-ions rock back and forth between the positive and negative electrode materials during charge and discharge. The positive electrode is typically a layered transition metal oxide (e.g. $LiCoO_2$, $LiNi_{1/3}Mn_{1/3}Co_{1/3}O_2$) coated onto aluminum foil and the negative electrode is typically graphite coated on copper foil. Both electrodes are adhered to their respective foils with a binder, typically poly-vinylidene fluoride (PVDF), carboxymethyl cellulose (CMC), and/or styrene butadiene rubber (SBR), and contain a conductive additive, typically a high surface area nanostructured carbon black, in order to maintain electrical contact between electrode particles. A porous separator, typically a multilayer polypropylene/polyethylene membrane, lies between the two electrodes, preventing their contact, although allowing lithium-ions to travel back and forth between them. A schematic diagram of a LIB can be seen in Figure 1.2.

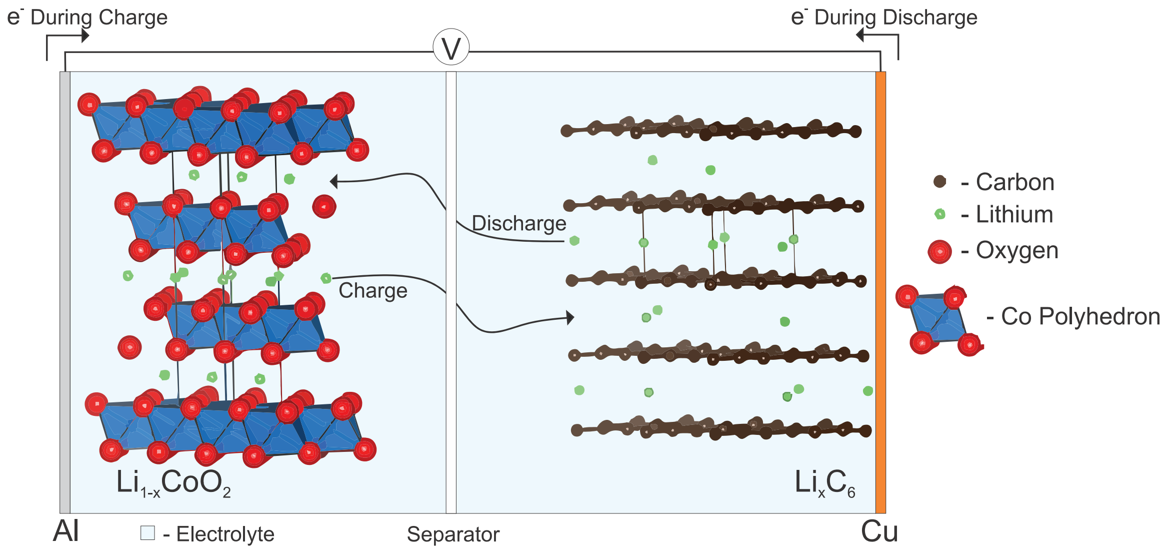

Figure 1.2 Schematic diagram of a lithium-ion battery.

Since their introduction in 1991, LIBs have, for the most part, relied exclusively on intercalation chemistry. Intercalation materials are limited in their ability to store lithium-ions by the number of crystallographic sites available in which lithium-ions can be hosted. This, therefore, imposes a limitation on energy density. Increases in energy density have primarily been achieved through cell engineering. Components of the LIB that do not contribute to energy density (current collecting foils, separators, and even the cell casing) have been reduced in size; and, binder and conductive additive have been reduced to the smallest percentage of the coatings as possible. Figure 1.3 shows the evolution of energy density of 18650 (cylindrical, 18 mm in diameter, 65.0 mm in length) cells since their commercialization. A plateau in energy density indicates that a shift in cell chemistry is required in order to continue increasing energy density of LIBs.

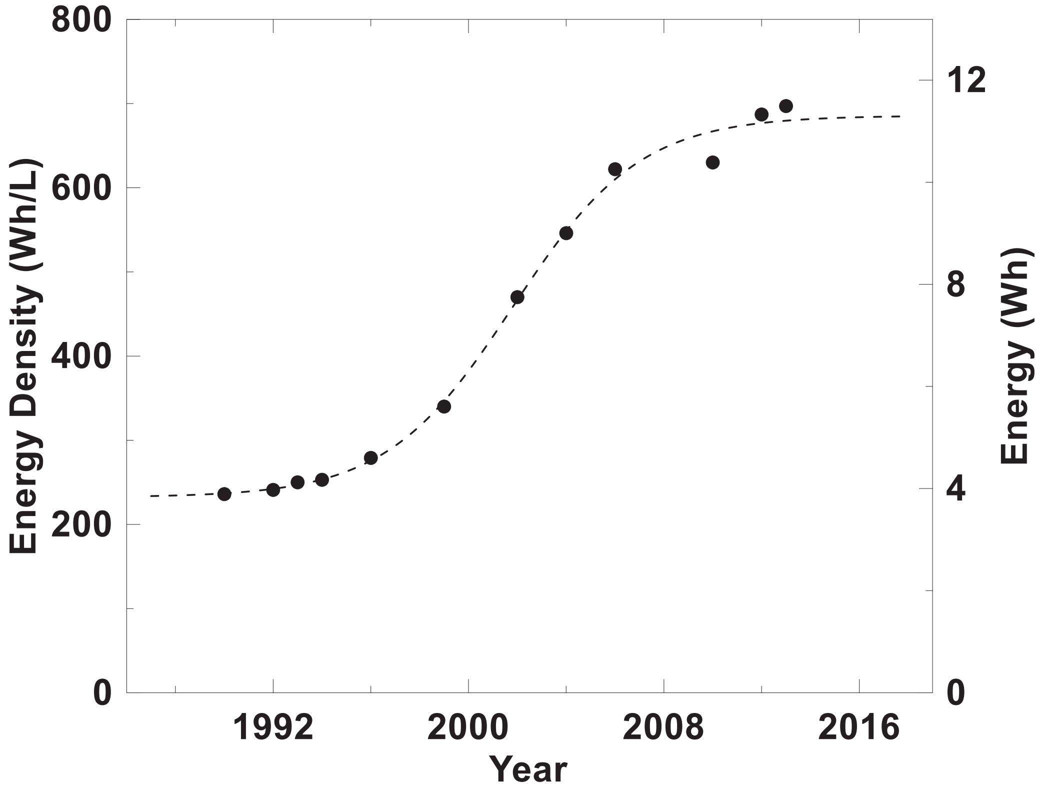

Figure 1.3 Evolution of volumetric energy density of commercial 18650 lithium-ion cells. Reproduced from Reference 22 with permission from the author.

1.2 Alloying Negative Electrodes

LIB electrode materials are not, however, limited to intercalation chemistry. Any element that forms alloys with lithium can be employed as an electrode material. The fully lithiated phase of an alloying material is then no longer limited by the initial structure as it is in the case of intercalation materials, where there are comparatively few crystallographic sites for Li-ions. Instead, the structure of alloying electrodes and their fully lithiated phases can vary considerably, allowing more Li-ions to be stored per host atom than intercalation materials. The specific capacity of a given material can be calculated according to the composition of the fully lithiated phase, as shown in Equation 1.1: where e is the elementary charge, N_A is Avogadro's number, z is the number of Li per host atom, and M is the formula weight of the active material. The calculated specific capacity for some of the alloys of lithium are shown in Figure 1.4, additionally the stoichiometry of the fully lithiated phase is shown.

$$Q = \frac{eN_A}{3.6zM} \tag{1.1}$$

Most any of the alloying materials in Figure 1.4 offer a massive increase in specific capacity over graphite. Specific capacity is an easily measured and calculated quantity; and, is often used to compare electrode materials; however, it has very little practical value in predicting how that material will affect energy density in a real LIB. The energy density of a LIB has several contributing factors in addition to specific capacity; therefore, in order to practically compare different electrode materials, it is important to develop a full cell model.

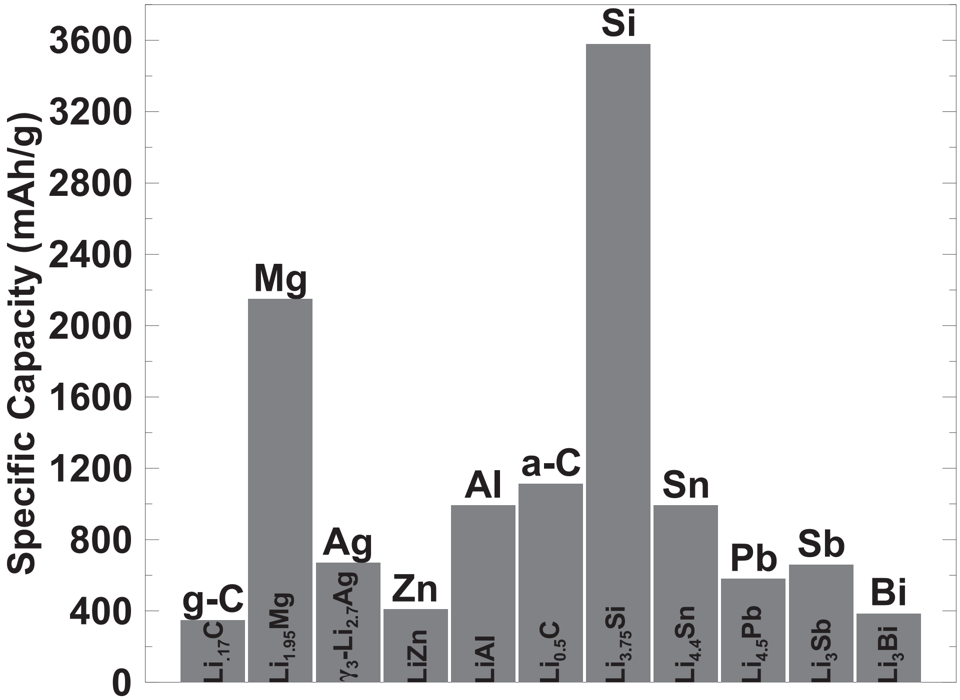

Figure 1.4 Calculated specific capacity of different alloying electrodes based on the fully lithiated phase, with graphite (g-C) for comparison. a-C denotes amorphous carbon.[23]

A simple method of estimating the impact of electrode materials on full cell energy density has been proposed in Reference 19.[23] In this model, a cell stack is used which acts the smallest repeatable unit necessary to replicate any commercial cell format, shown in Figure 1.5. Cell parameters were selected in order to model a typical commercial energy cell. The positive electrode was selected to be 70% by volume $LiCoO_2$, at a thickness of 55 µm. Current collector thickness was fixed at 15 µm, and separator thickness was fixed at 20 µm. Negative electrode thickness is, however, variable. The negative electrode must be balanced in order to accommodate the number of lithium ions stored in the cathode, considering the irreversible capacity of both electrodes, while still having 10-20% excess capacity in order to prevent lithium metal plating. Additionally, in this model, the negative electrode is considered to be a pure thin film with zero porosity.

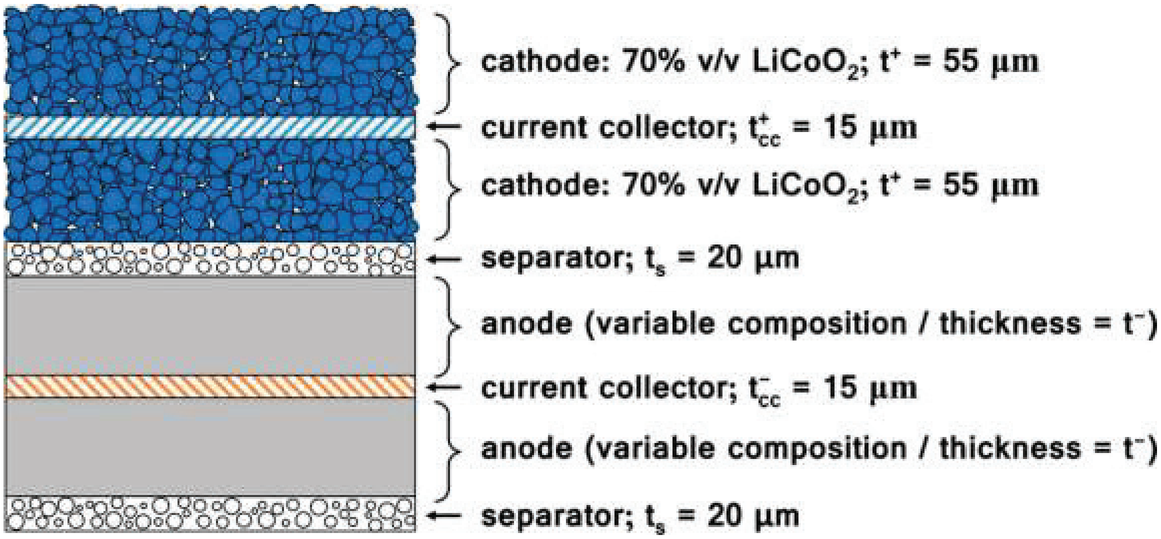

Figure 1.5 Cell stack model for lithium-ion battery full cell model, where t^+, t^+_{cc}, t_s, t^-, t^-_{cc} are the thickness of the cathode, cathode current collector, separator, anode, and anode current collector respectively. Reprinted with permission from Reference 23. Copyright American Chemical Society 2014.

Energy density based on this cell stack model can therefore be calculated according to Equation 1.2, where U is energy density in Wh/L, q_R^- is the anode volumetric capacity, and V^-_{avg} is the average potential of the negative electrode.[23]

$$U = \frac{58327.5\,\frac{\mathrm{Ah}}{\mathrm{L}}}{70+(110)\left[1+\frac{583.275\frac{\mathrm{Ah}}{\mathrm{L}}}{q_R^-}\right]}\left[3.9\mathrm{V} - V_{avg}^-\right] \tag{1.2}$$

The calculated values for stack energy density are shown in Figure 1.6. An additional scale bar depicts cell energy if the stack model were extended to the volume of an 18650 cell, and the secondary y-axis shows percent improvement over a graphite anode. According to this model, at best, a modest (42%) increase in energy density can be achieved with an alloying negative electrode. Figure 1.6 also highlights the importance of considering the stack model rather than the specific capacity alone. When compared with Figure 1.4, the massive increase in specific capacity of Si does not translate to as large of an improvement in cell energy; whereas the much smaller increase in specific capacity of Ag and Sn translates to a much larger increase in cell energy. Again, this is because energy density is also related to average lithiation potential as well as the density of the material.

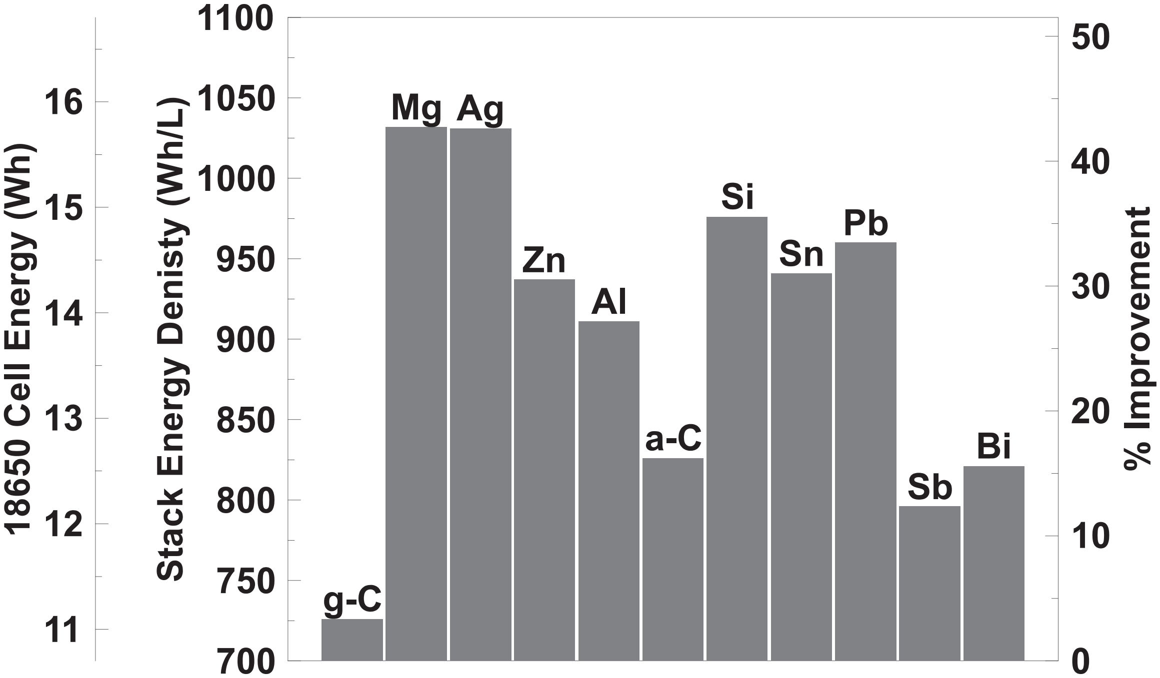

Figure 1.6 Energy density calculation from the cell stack model for different alloying electrodes, including a scale bar for the common 18650 cell format, data taken from Reference 23.

Any of the alloying materials presented in Figure 1.6 show some percent improvement over graphite; therefore, producing a LIB with increased cell energy is seemingly facile. Figure 1.6 may be misleading in this respect. Though these materials show improvement in the cell stack model; this has no bearing on functionality nor applicability. For example, Mg has been shown to have poor rate capability (unable to lithiate and de-lithiate fully at high current densities) this leads to slow charge and discharge cycles in order to achieve full capacity. Additionally, the average lithiation potential of Mg is very close to zero (vs Li/Li^+) and therefore Mg electrodes are susceptible to lithium plating,[24,25] which compromises safety. Ag is far too expensive to be considered as the main substituent in a commercial electrode. Pb is toxic and therefore undesirable. Zn has been found to catalytically decompose electrolyte and is not a promising candidate as a negative electrode.[26] Al shows rapid capacity fade as a result of cycling over a 2 phase region.[23,27]

Both Si and Sn have been explored extensively as possible alloying negative electrodes. Because of the Co requirement for a functioning Sn electrode, this has severe implications on electrode cost.[28] This is especially apparent in Table 1.1, where, pure Sn (without considering stoichiometric addition of Co) is more expensive than graphite on a cents/Ah basis. Silicon, however, is by far the cheapest electrode material As a result Si is the material of interest in this work; therefore, the following sections will discuss the lithiation behaviour of Si electrodes.

Table 1.1 Cost analysis of different electrode materials on a price per Ah basis. Reproduced from Reference 29 with permission from the author.

Material	$/kg	Ah/kg	¢/Ah
g-C	5	372	1.3
Si	2	3579	0.06
Sn	20	993	2.0

1.3 Electrochemical Lithiation of Silicon

The electrochemical lithiation of silicon does not follow an intercalation mechanism. Initial studies of the lithiation of silicon were done at high temperatures (400-450 ºC) and it was found that phase formation followed the binary phase diagram, forming progressively more lithium rich phases from $Li_{12}Si_7$, Li_7Si_3, $Li_{13}Si_4$, to $Li_{22}Si_5$.[30] Because of this, the theoretical capacity of silicon is often miscalculated as 4200 mAh/g; this is incorrect because the room temperature lithiation of silicon differs significantly. Limthongkul et. al showed that the room temperature lithiation of silicon did not follow the binary phase diagram, rather forming an increasingly lithium rich amorphous alloy.[31] Obrovac and Christensen later showed the formation of a new metastable $Li_{15}Si_4$ phase.[2] The lithiation behaviour of Si can be described, in part, by its potential profile.

The potential profile measures the potential of the electrode (vs Li/Li^+) as ordinate and capacity as abscissa. Capacity can be correlated directly to composition as one mole of Li-ions in the Si structure corresponds to 954.3 mAh/g; therefore, the potential profile can then be used to indicate phase formation as a function of Li content by considering Gibbs' phase rule. The potential profile for the room temperature lithiation of Si is shown in Figure 1.7.

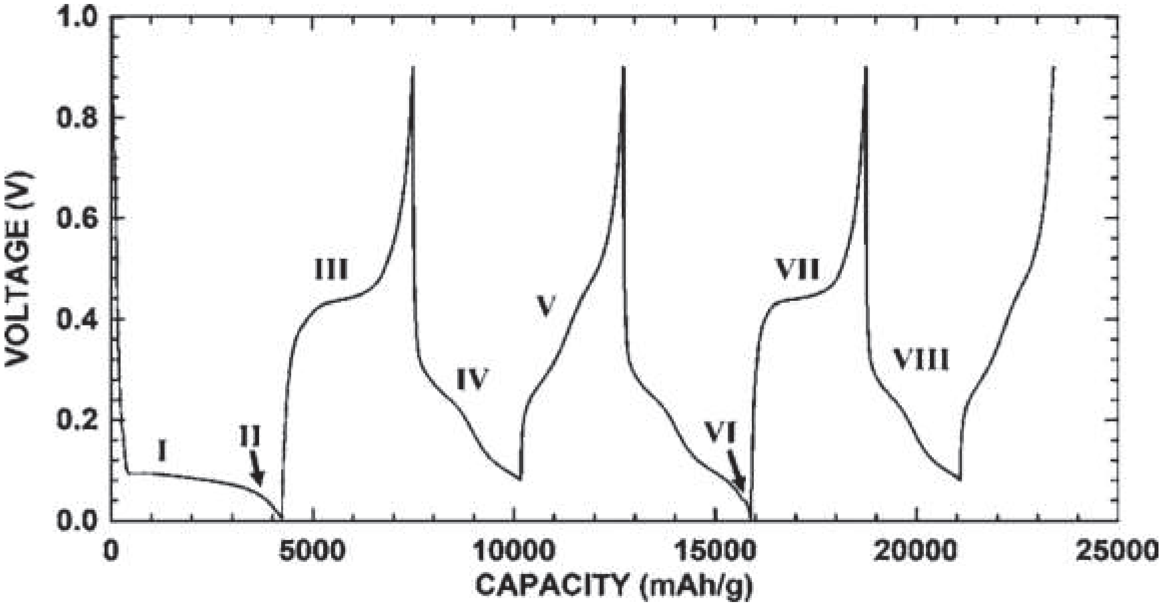

Figure 1.7 Room temperature electrochemical lithiation of bulk Si powder voltage curve. Reproduced with permission from Reference 32. Copyright Electrochemical Society 2007.

The Gibbs' phase rule describes the number of degrees of freedom of a system, *F*, where *c* is the number of chemical species required to fully describe the system, *p* is the number of homogeneously separated phases, and *n* is any other variable required to describe the state of the system (typically pressure and temperature), this is shown in Equation 1.3.

$$F = c - p + n \tag{1.3}$$

In the case of the electrochemical lithiation of Si, there are two components (Li and Si) and *n* is zero (pressure and temperature are constant); therefore, the variation in potential with composition will depend entirely on the number of phases. Given a single phase lithiation reaction, potential will decrease as Si is continually reduced by the addition of Li. However, in the case of a two-phase reaction, *F* for the system is reduced to zero and the potential must remain invariant.

The initial sloping potential profile, denoted “I” in Figure 1.7, is consistent with the formation of a progressively Li rich amorphous Li_xSi (a-Li_xSi) alloy by the addition of Li to crystalline Si (c-Si), as determined by Limthongkul et. al. The variable composition, x, of the a-Li_xSi alloy formed results in a sloping plateau as Si is continually reduced by the addition of Li. The crystallization of $Li_{15}Si_4$, as determined by Obrovac and Christensen, is observed as a very small potential plateau, denoted “II”, found near 50 mV. $Li_{15}Si_4$ is a metastable phase observed only in the room temperature lithiation of Si. More Li rich phases observed in the Li-Si binary phase diagram are not formed as the result of energetic barriers preventing the rearrangement of Si atoms. The de-lithiation of $Li_{15}Si_4$, denoted “III”, can be observed as a potential plateau at 450 mV indicating a two-phase reaction where a-Li_2Si is formed. This is followed by the uniform de-lithiation of a-Li_2Si forming a-Si.

The following lithiation and de-lithiation cycles are therefore independent of the initial c-Si structure as only a-Si remains. The lithiation of a-Si follows a solid-solution type reaction as a-Si is homogenously lithiated a sloping potential profile is observed, denoted “IV” in Figure 1.7. Two quasi-plateaus are observed in region “IV”, the first is the result of Li entering an environment dominated by Si nearest neighbours. This continues until there are ~2.3 Li per Si and the first nearest neighbour shell of Si is fully occupied.[33] The second quasi-plateau is the result Li entering an environment dominated by Li nearest neighbours as the Si nearest neighbour shell is fully occupied, this quasi plateau is therefore at a lower potential. This result was discovered by Li et. al using *in-situ* ^{119}Sn Mössbauer spectroscopy of Si with an Sn probe.[33] The de-lithiation of a-Si is, however, dependant on the lithiation history. If a-Si is not lithiated beyond ~70 mV, $Li_{15}Si_4$ does not form and the de-lithiation follows the reverse solid-state reaction such that a-Li$_x$Si forms a-Si, this is observed in the region of the voltage curve denoted “V”. However, if lithiation proceeds below ~70 mV and Li$_{15}$Si$_4$ crystalizes, observed in the region denoted “VI”, the 450 mV plateau is observed and de-lithiation follows a two-phase reaction forming a-Li$_2$Si followed by the solid-solution reaction forming a-Si, observed in the region denoted “VII”. The entire reaction scheme of c-Si and a-Si is summarized in the following Equations 1.4-1.8.

I)
$$\text{c-Si} + \text{Li} \xrightarrow{\text{170 mV plateau}} \text{a-Li}_\text{x}\text{Si} \tag{1.4}$$

II & VI)
$$\text{a-Li}_\text{x}\text{Si} + \text{Li} \xrightarrow{\text{50 mV plateau}} \text{c-Li}_{15}\text{Si}_4 \tag{1.5}$$

III & VII)
$$\text{c-Li}_{15}\text{Si}_4 \xrightarrow{\text{450 mV plateau}} \text{a-Li}_2\text{Si} + \text{Li} \rightarrow \text{a-Si} + \text{Li} \tag{1.6}$$

IV & VIII)
$$\text{a-Si} + \text{Li} \rightarrow \text{a-Li}_\text{x}\text{Si} \tag{1.7}$$

V)
$$\text{a-Li}_\text{x}\text{Si} \rightarrow \text{a-Si} + \text{Li} \tag{1.8}$$

1.4 Binders and Electrolyte Additives

Up until this point, the discussion of alloying negative electrodes has entirely neglected volume expansion. When Li-ions are inserted between the layers of graphite, there is very little expansion: ~10% along the c-axis perpendicular to the graphene layers. Si, however, behaves very differently. The ability to store such a large number of Li-ions per host atom leads to a volume expansion as large as 280%,[1] shown schematically in Figure 1.8.

Volume expansion is detrimental to cycling performance at all levels of cell construction and is one of the factors that has prevented the widespread commercialization of alloying negative electrodes despite their obvious increases in cell energy. From a macroscopic scale there has been observed: crushed separators, current collector distortion, and cell case bulging. At the particle level the repeated expansion and contraction of particles has led to loss particle-particle contact and therefore cell fade.[3,34] Additionally, repeated expansion and contraction causes continuous solid electrolyte interphase (SEI) growth, again, leading to cell fade and increased potential polarization.[35,36] At the sub particle level internal stress can lead to particle fracture, mechanical disconnection resulting in the loss of electrical contact and therefore cell fade.[3,35,37]

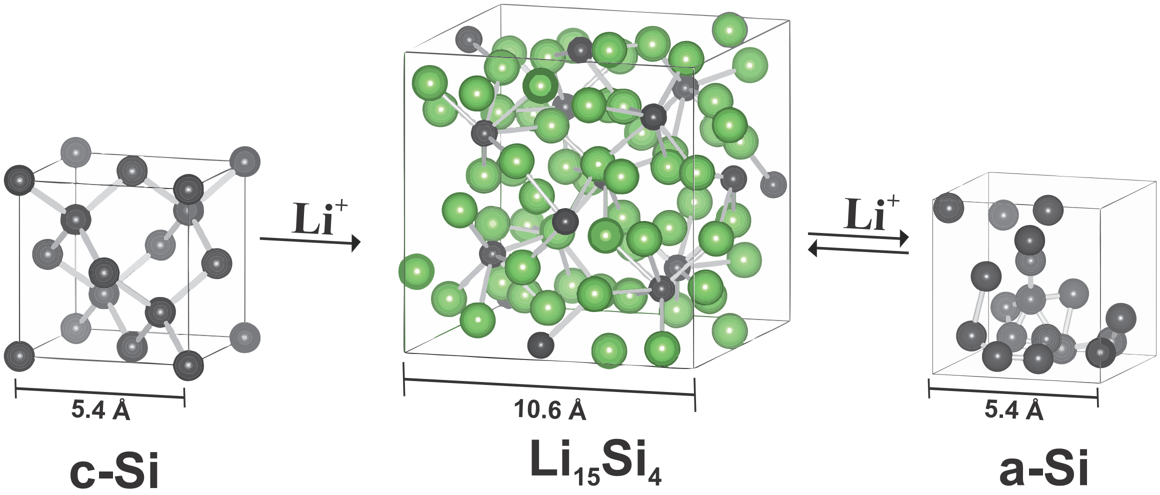

Figure 1.8 Schematic diagram of the electrochemical lithiation of silicon on the scale of the unit cell.

The presence of a binder in LIB electrode coatings ensures good cohesion and adhesion strength to the current collecting foil during the handling and manufacturing process; but, is also responsible for good electrochemical performance. This is especially true for alloying negative electrodes where repeated lithiation and de-lithiation cycles cause a large expansion and contraction of the active material particles. Given lithiation has been limited such that an identical capacity to graphite has been achieved, the resultant volume expansion (in the case of Si) is still 36%. This is more than triple the expansion observed in fully lithiated graphite and cannot be tolerated by binders conventionally used for intercalation materials. Figure 1.9 shows the voltage curve of a pure Si electrode coated using a PVDF binder.[38] The first half cycle shows lithiation to roughly 2650 mAh/g; however, when lithium is removed a reversible capacity of only 250 mAh/g is observed. A high degree of lithiation is achieved in the first half cycle, this is because as Li is added particles expand and maintain good electrical contact. However, as Li is removed particles contract, fracturing and losing electrical contact preventing further de-lithiation; and a small reversible capacity is therefore observed.

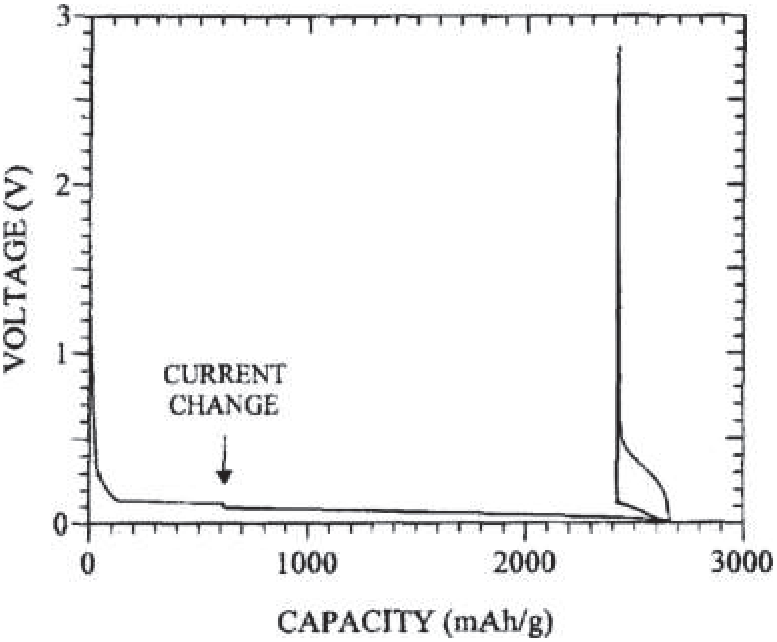

Figure 1.9 Voltage curve: lithiation of pure Si anode using PVDF binder. Reproduced with permission from Reference 38. Copyright Electrochemical Society 1995.

Poor electrochemical performance can be directly related to the properties of the PVDF binder. In a conventional PVDF coating, PVDF forms a polymer fiber (<30 nm) network surrounding active material particles.[39] The majority of the particle surface therefore remains exposed to electrolyte allowing substantial electrolyte decomposition, SEI growth, increased electrode impedance, and isolation of electrode particles.[36] Additionally, PVDF does not chemically bond to the surface of the active material particles, and experiences severe swelling when exposed to electrolyte compromising the mechanical integrity of the electrode.[36,40] The combination of these effects allows electrode particles to become disconnected easily, especially when a large volume expansion is experienced by the active material particles.

A suitable binder for alloying negative electrodes should then have the following properties: good adhesion and cohesion strength to active material particles and current collector; the ability to coat the entire surface of active material particle inhibiting continuous SEI growth; the ability to tolerate volume expansion by stretching. In order to achieve these properties research has been focused on water-based poly(carboxylic acid) binders, including poly(acrylic acid) (PAA)[36,40–42] and CMC.[43–49] Poly(carboxylic acid) binders have been shown to have good adhesion to Si particles, forming a ester-like covalent bond with the native surface of Si composed of silicon oxide (Si-O-Si) and silanol (Si-OH). Additionally, poly(carboxylic acid)s are able to cover the entire surface of the active material particles, do not swell when in contact with electrolyte, and can withstand repeated volume expansion of Si as a result of their mechanical properties when composed of a small number of polymer chains. Though it has been shown that bulk poly(carboxylic acid)s are brittle, polymers can behave quite differently on a much smaller scale.[40] When using appropriate binders to tolerate volume expansion upon lithiation, acceptable cycling performance can be achieved at capacities considerably higher than that of graphite, with excellent capacity retention over a large number of cycles.[41]

In addition to binder chemistry, the role of electrolyte additives has been equally important in the advancement of alloying negative electrodes. Repeated volume expansion can lead to continual formation of SEI depleting electrolyte salt and solvent, irreversibly trapping Li in the SEI layer, isolating active material particles, and generally leading to poor electrochemical performance.[40,50] When no electrolyte additives are present to control SEI formation, SEI is formed from electrolyte salt (typically $LiPF_6$) and solvent (carbonates) leading to the formation of a porous and unstable SEI layer primarily composed of LiF, Li_xF_y, or $Li_xPO_yF_z$[51–55] and alkyl carbonates.[52,54,56,57] Electrolyte additives, however, consist of a species more reactive than the electrolyte salt or solvent that will readily reduce forming a more stable SEI layer. Fluoroethylene carbonate (FEC) is one such additive, that has been shown to reduce to form an SEI composed predominantly of LiF,[58–60] therefore preventing the reduction of $LiPF_6$ and or electrolyte solvents, then forming an SEI layer that is thinner, more stable and does no grow continually.

1.5 Two-Phase Regions and Volume Expansion

The negative effects of volume expansion are especially apparent when alloying electrode materials are cycled over a two-phase region. In the case of a single-phase reaction, lithium is added or removed homogeneously in a solid-solution type reaction and volume expansion is therefore experienced by the particle homogenously. However, in the case of a two-phase reaction stress is observed at the reaction front as a result of the difference in molar volume of the lithiated and un-lithiated phases.[4] The stress at the phase boundary has been shown to cause plastic deformation and fracture in alloying electrode particles resulting in the loss of electrical contact and cell fade.[61–64] Two phase regions should therefore, in most cases, be avoided. This is why the use of Co was vital in Sony's Nexelion, $Sn_{30}Co_{30}C_{40}$, anode material. Co prevented the aggregation of Sn grains, therefore maintaining an amorphous microstructure allowing $Sn_{30}Co_{30}C_{40}$ to cycle over a single-phase region. Preventing two-phase regions during the cycling of Si, however, does not require Co as in the case of Sn. Given the structure of Si is amorphous, and the lower cut-off potential is greater than ~70 mV, as described in section 1.3, $Li_{15}Si_4$ does not crystallize and two-phase regions are avoided.

Avoiding two-phase regions prevents particle fracture but does not render the electrode material immune to the additional effects of volume expansion. In order to achieve acceptable cycling performance, volume expansion must be limited to some tolerable quantity. Two methods for limiting volume expansion will be discussed. The first method is limiting volume expansion by imposing a lower-potential limit. The second method is decreasing the total amount of active Si by alloying with an inactive element, therefore forming an inactive silicide. For the purpose of this discussion, both methods will be compared assuming total volume expansion is restricted to 100%. The resultant voltage curves, considering each method of limiting volume expansion, are shown in Figure 1.10.[23]

By imposing a lower cut-off potential such that volume expansion does not exceed 100%, a large portion of the potential range is unused, represented by a dashed line in Figure 1.10. By not accessing this part of the potential range the average potential is 0.57 V. In the case of a Si/inactive alloy the entire potential range can be utilized, and volume expansion can be controlled strictly by the quantity of inactive phase that has been added and the average potential is therefore the same as a-Si, 0.41 V, given the same capacity. According to the cell stack model calculation for energy density, shown in Equation 1.2, energy density increases linearly as the potential of the negative electrode is decreased. Therefore, a Si/inactive alloy will achieve increased energy density compared to pure Si, when cycling is restricted to a given volume expansion.

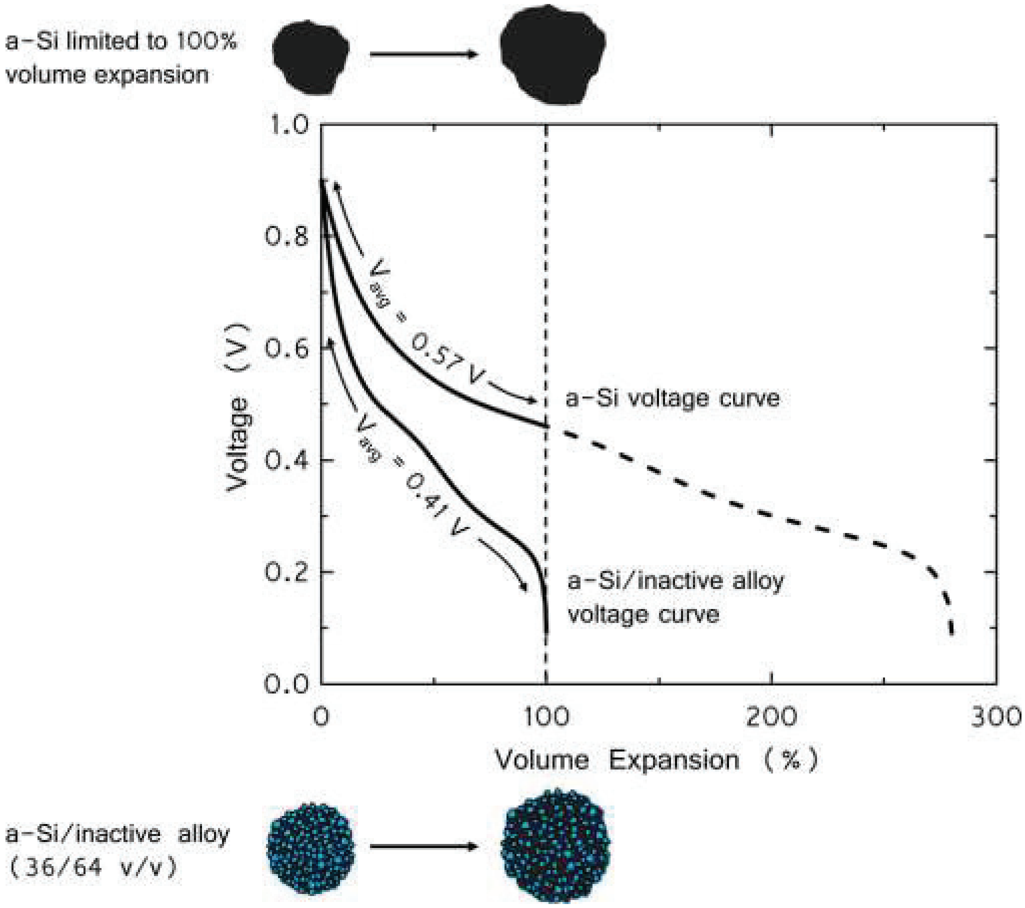

Figure 1.10 Voltage curve for Si limited to 100% volume expansion by imposing a lower-potential limit and by forming a Si/inactive alloy. Reproduced with permission from Reference 32. Copyright Electrochemical Society 2007.

The use of Si/inactive alloys as a negative electrode is additionally advantageous in that Si/inactive alloys have been shown to suppress the formation of $Li_{15}Si_4$ when Si is present as nano-meter sized grains in an inactive matrix, therefore avoiding the two-phase reaction front and improving cycling performance.[65–67] The stress experienced by the Si grains upon lithiation, when present in an inactive matrix, decreases the potential at which lithium will alloy,[68,69] therefore decreasing the potential at which $Li_{15}Si_4$ will crystalize, in turn decreasing the average potential of the Si/inactive alloy negative electrode and increasing energy density.

A number of Si/inactive alloy negative electrodes have been previously explored using mechanochemical synthesis summarized in Table 1.2. Most often Si-TM intermetallic phases are inactive, as a result the electrochemistry of such materials is similar, and the potential profile reflects that of the active Si phase. Increasing inactive phase content decreases volume expansion thereby improving cycling performance.

Table 1.2 Review of ball milled Si-TM alloys.

System	Selected Composition	Alloyed Phase	Capacity (mAh/g)	Alloyed Phase active/inactive
Si-Fe-Zn[70]	$Si_{75}Fe_{20}Zn_5$	α or β-$FeSi_2$	1115	Inactive
Si-Ni[71]	$Si_{85}Ni_{15}$	$NiSi_2$	1374	Active
Si-Cu[72]	$Si_{80}Cu_2$	Cu_3Si	1681	Active
Si-Fe-O[73]	$Si_{80}Fe_8O_{12}$	α-$FeSi_2$ and Si-O	1938	Active
Si-Ti[74]	$Si_{85}Ti_{15}$	$TiSi_2$	1377	Inactive
Si-Fe-Mn[75]	$Si_{83}Fe_{12}Mn_5$	α and β-$FeSi_2$	1406	Inactive
Si-W[76,77]	$Si_{85}W_{15}$	WSi_2	757	Inactive

Si/inactive alloys will be explored in this work, where the inactive component comprises Fe and Cr. Mechanochemical synthesis will be employed as a commercially relevant technique to generate Si/inactive alloys with an amorphous microstructure. Microstructure of these alloys will be characterized by X-ray diffraction (XRD), Mössbauer spectroscopy, and electrochemical performance evaluated in half cells with a Li-metal counter electrode.

1.6 Organization of Thesis

Chapter 2 highlights the experimental techniques used in this work as well as relevant background information for each experimental technique.

Chapter 3 highlights the kinetics of the mechanochemical alloying of the Si alloys as well as electrochemical characterization.

Chapter 4 focuses on a new technique for quantitative composition determination by Mössbauer spectroscopy, which allows quantification of Fe contamination in mechanically alloyed Si alloys which has previously never been reported.

Chapter 2 **Experimental Techniques**

2.1 Mechanical Alloying

Mechanical alloying is a solid-state powder processing technique developed in the 1960's by the International Nickel Company in order to generate oxide dispersed strengthened nickel and iron alloys.[78] The underlying principles by which the mechanical alloying of two powders occurs relies on rudimentary mechanical properties of materials, and so time will be taken to adequately define the necessary terms.

Figure 2.1 shows the typical stress strain curve of a ductile material. As stress is applied, that is, force per unit area, the strain increases proportionately, that is, the relative length that the material is elongated (in tension). Stress and strain remain proportional so long as the yield strength is never exceeded, and the stress/strain behaviour remains elastic. However, when the yield strength is exceeded, and the stress/strain behaviour is in a plastic regimen, hysteresis is observed. The material does not return to its original shape and remains elongated to some degree.[79]

Mechanical alloying takes advantage of the plastic deformation of a material. As a material continually undergoes plastic deformation, dislocations in the crystal structure are frozen in place and the material transitions from ductile to brittle; this is referred to as work hardening.[79] A brittle material behaves identically to a ductile material in an elastic regimen; however, when the yield strength of a brittle material is exceeded there is no plastic deformation and instead the material fractures.[79]

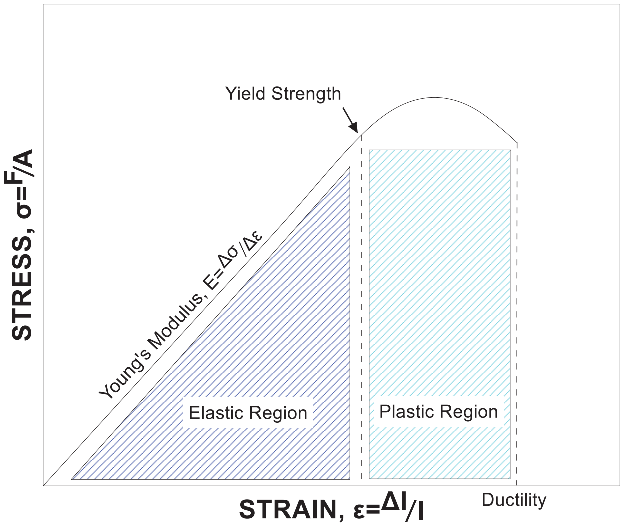

Figure 2.1. Stress strain curve of a ductile material where stress, σ, is proportional to force, F, per unit area, A, and strain, ε, is proportional to the change in length, l, over the initial length.

Mechanical alloying uses milling media (typically balls) contained within a milling vessel with the addition of precursor powders. The vessel is agitated such that there are high energy collisions amongst the milling media. In every collision some quantity of powder is trapped between the milling media and is plastically deformed. After repeated plastic deformation, particles fracture forming fresh reactive surfaces. Fresh reactive surfaces of newly fractured particles cold weld, thereby forming an alloy. Particle fracture results in a net decrease in particle size while cold welding results in a net increase in particle size. These two processes initially occur at differing rates until equilibrium is established and all particles contained in the vessel are homogeneous and refined to some intermediate size.[78]

In this work SPEX 8000 (SPEX model 8000-D, Spex CertiPrep, Metuchen, NJ) shaker mills are used to generate mechanically alloyed powders. The SPEX 8000 shaker mill is considered a high energy variety of ball mill with a vibrational amplitude in a “figure eight” motion of roughly five centimeters and a frequency of 16.7±0.8 Hz. It was previously believed that true mechanical alloying could only occur with large milling media providing sufficient impact energy for plastic deformation to occur;[80] however, it was recently shown that using a larger quantity of small milling media can produce a more amorphous alloy in a shorter amount of time.[81] By optimizing the impact frequency of lower energy impacts with small milling media, amorphous mechanically alloyed powders can be produced more efficiently than using large milling media and optimizing impact energy.[81]

In this work all mechanochemical reactions were carried out under the same conditions. A 65 mL hardened steel vessel (Spex CertiPrep, Metuchen, NJ), loaded with 180 grams of 1.6 mm in diameter stainless steel milling balls, and 0.5 mL of precursor powder were sealed under argon and milled with a SPEX 8000D shaker mill. As described by Hatchard et al. these conditions optimize the formation of amorphous alloys with improved microstructure as indicated by their electrochemical performance.[81]

2.2 X-Ray Diffraction

2.2.1 X-Ray Diffraction Theory

X-Ray diffraction (XRD) is one of, if not, the most valuable non-destructive characterization techniques for crystalline solids available to materials scientists. Using an incident X-Ray beam, XRD probes the crystal structure of a material by observing the intensity of the diffracted X-Ray beam. As seen in Figure 2.2, when incident X-rays strike a series of atoms on lattice planes separated by a distance, d (referred to as d-spacing), the diffracted X-rays will interfere constructively when the path difference is equal to an integer number of wavelengths. This is known as Bragg's law for which the Bragg father and son team won the Nobel prize in 1915.[79] Therefore, by measuring the intensity of the diffracted X-Ray beam as a function of the incident angle, the angle at which each Bragg peak is located is directly related to the d-spacing of the responsible lattice planes in the crystal structure.

Bragg's law is able to describe at what incident angles diffraction may occur, however, it does not describe the intensity of the diffracted beam. The intensity of the diffracted beam relies on several factors as seen in Equation 2.1.

$$I(2\theta) = P(2\theta)L(2\theta)[F(hkl)]^2 m(hkl)DW(2\theta) \tag{2.1}$$

Where I is the measured intensity of the diffracted beam, P is the polarization factor, L is the Lorentz factor, F is the atomic structure factor, m is the multiplicity, and DW is the Debye-Waller factor.

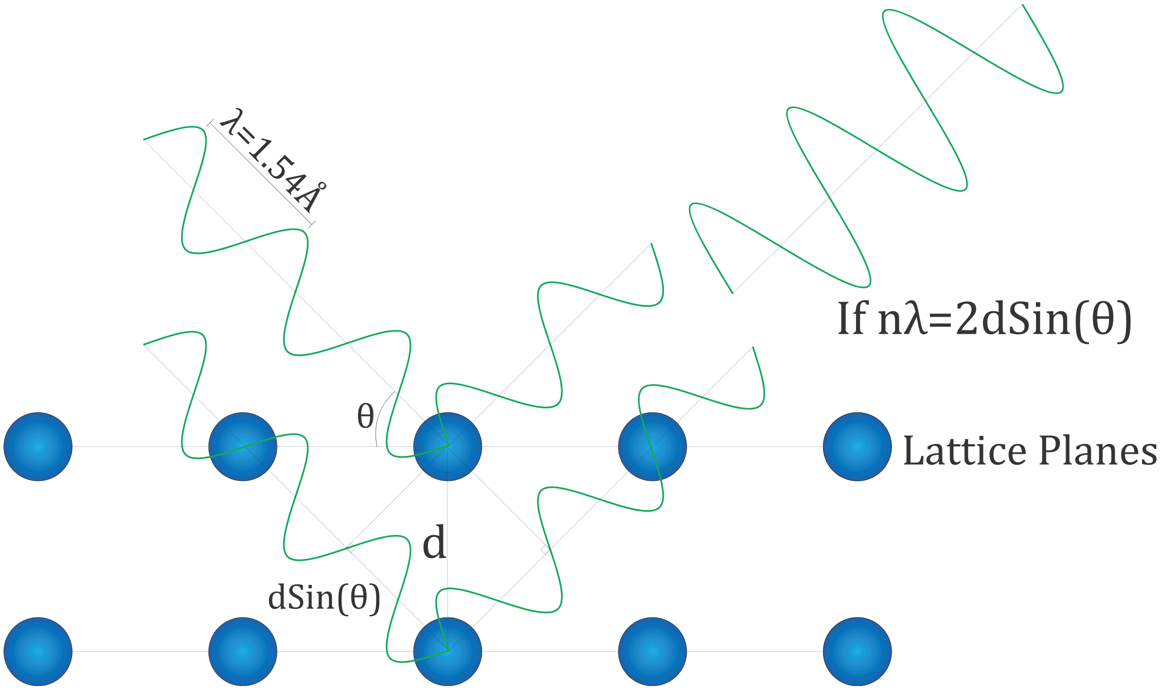

Figure 2.2. Schematic diagram of Bragg's law and the conditions required for constructive interference of diffracted X-rays.

The polarization factor is an intensity correction that considers the decrease in intensity of a diffracted X-Ray polarized in the plane of diffraction. Considering the two scenarios: when an X-Ray is polarized in the plane of diffraction there is a reduction in intensity by a factor of $\cos^2(2\theta)$; though, when the X-Ray is polarized perpendicular to the plane of diffraction intensity is unaffected. Therefore, the total reduction in intensity can be considered as the average of the two scenarios The total expression for the polarization factor can be seen in Equation 2.2, in this expression θ_M is the angle at which the monochromator is held (monochromators will be discussed in section 2.2.3.

$$P(2\theta) = \frac{(1+cos^2(2\theta)cos^2(2\theta_M))}{(1+cos^2(2\theta_M))} \tag{2.2}$$

The Lorentz factor is an intensity correction that considers the probability of finding a crystallite with the correct orientation for diffraction as a function of the incident angle. A powder sample is composed of many crystallites, though their orientation is random, there will be a dependence of intensity upon the angle of incidence, as seen in Equation 2.3.

$$L(2\theta) = \frac{1}{\sin(\theta)\sin(2\theta)} \tag{2.3}$$

The polarization and Lorentz factors are independent of the crystalline structure and related only to the angle of incidence. Because of this they are sometimes grouped together as the Lorentz-Polarization (LP) factor.

The atomic structure factor is typically expressed as relying on the Miller index of the lattice planes responsible for constructive interference. Miller indices are a convenient way of describing lattice planes in a crystal lattice summarized by three integers, h, k, and l. The plane specified by a given set of h, k, and l, intersects the unit cell at a/h along side a, b/k along side b, and c/l along side c. For example, the plane (100) is perpendicular to side a, and parallel to sides b and c. The plane (111) intersects at the three corners of the unit cell closest to the origin. Based on the lattice type of the unit cell the distance between each set of equivalent planes can be calculated, that is, the $d_{(hkl)}$ spacing of that set of planes. Therefore, given that the positions of all of the atoms in the unit cell are known then the atomic structure factor can be calculated for every set of lattice planes as seen in Equation 2.4, where n represents all of the atoms in the unit cell, and x, y, and, z are the fractional atomic coordinates.

$$F(hkl) = \sum_n f_n e^{i2\pi(hx_n+ky_n+lz_n)} \tag{2.4}$$

In Equation 2.4 f is the atomic scattering factor. Given that X-rays are scattered by electrons, each atom will scatter X-rays differently depending on the number of electrons and how electron density is distributed about the nucleus. Atomic scattering factors have been computed as a function of incident angle, as f will vary as a function of incident angle, for all atoms in all oxidation states using quantum-mechanical methods, and are available in the International Tables for Crystallography Volume C.[82]

The multiplicity of a set of lattice planes is the number of lattice planes with a different Miller index, but, having equivalent d-spacing. For example, the set of planes {hkl} (h≠k≠l≠0) in a cubic unit cell has a multiplicity of 48. Because the three lattice parameters a, b, and c are equal, all permutations of positive or negative values in all three positions h, k, and l, produce the same plane. However, if the symmetry of the unit cell is reduced from cubic to orthorhombic (a≠b≠c) then the set of planes {hkl} (h≠k≠l≠0) has a multiplicity of 8. In this case exchanging h, k or l will result in a different plane because the lattice parameters are not equal.

The final parameter described in Equation 2.1 is the Debye-Waller factor. The Debye-Waller factor considers the effect of temperature on intensity as a function of incident angle. Atoms are constantly vibrating about their mean lattice position, and vibrational amplitude and frequency will increase with increasing temperature or decrease with increasing atomic mass. Therefore, measured intensity will decrease as a result of increased displacement from lattice positions as seen in Equation 2.5, where B is a parameter related to the mean square amplitude of an atoms vibration about its mean position.

$$DW(2\theta) = e^{-B\frac{sin^2(\theta)}{\lambda^2}} \tag{2.5}$$

Therefore, considering all of the terms presented in Equation 2.1, given the crystal structure is known, the diffraction pattern as a function of incident angle can be calculated. Alternatively, crystal structure convolution is possible given the diffraction pattern.

2.2.2 X-Ray Diffraction: Phase Analysis

The relative intensity of each phase in a diffraction pattern can be used as a qualitative analysis of composition. Integrated intensity is not directly related to composition as intensity of each phase will be additionally modulated by the atomic scattering factor. One method for quantitative phase analysis of XRD patterns is Rietveld refinement. Rietveld refinement uses Equation 2.1 to calculate a theoretical diffraction pattern based on the crystal structure of the phases present. Depending on the factor required to scale the intensity of the calculated diffraction pattern, an atomic and/or weight fraction of each phase can be determined.

Quantitative phase analysis by Rietveld refinement in this case, however, is not suitable. The diffraction patterns of phases formed by mechanochemical reactions often vary from the calculated diffraction patterns in unpredictable ways as the result of disorder introduced by high energy collisions of milling media and cannot be modeled well by the expected crystal structures. In this work, a qualitative phase analysis is considered in lieu of Rietveld refinement, simply by fitting pseudo-Voigt curves to the diffraction pattern in order to determine the relative integrated intensity of each phase. A pseudo-Voigt curve is a linear combination of a Lorentzian and a gaussian, show in Equation 2.6, where γ is a shape parameter modulating the curve from Lorentzian (γ=1) to Gaussian (γ=0), *FWHM* is the peak full width at half maximum (in 2θ units), and $2\theta_i$ is the diffraction angle of the peak maximum, and A is the area of the phase.

$$PV(2\theta) = A\left[\gamma \frac{2}{FWHM*\pi}\left[1+4\left[\frac{(2\theta_i-2\theta)}{FWHM}\right]^2\right]^{-1} + (1-\gamma)\frac{\sqrt{4\ln(2)}}{FWHM\sqrt{\pi}}e^{-\sqrt{4\ln(2)}\left[\frac{(2\theta_i-2\theta)}{FWHM}\right]^2}\right] \quad (2.6)$$

Peak fitting additionally enables the computation of grain size from the measured *FWHM*. The Scherrer equation is an extension of Bragg's law correlating *FWHM* to grain size, shown in Equation 2.7, where L is the average grain size and K is an empirical constant.

$$L = \frac{K\lambda}{FWHM(2\theta)cos\theta} \quad (2.7)$$

In order to determine the error associated with the pseudo-Voigt fitting procedure, Error bars were calculated according to the standard error of the fitting parameters across 50 data sets generated by a Monte Carlo simulation.

An error vector was calculated by subtracting the initial fit from the raw data. Taking the outer product of the error vector results in the error covariance matrix shown in Figure 2.3 a). A singular value decomposition of the error covariance matrix can then be used to simulate noise with the same characteristics as the initial signal by $S^{1/2}V^T$, where V is an orthonormal basis of the directions of highest variance in the error covariance matrix, and S is a diagonal matrix of the magnitudes of variance in V. A simulated noise vector can then be generated by $e_{iid}S^{1/2}V^T$,[83] where e_{iid} is the independent identically distributed error; a vector of random values between zero and one generated by the Monte Carlo simulation. The simulated noise can then be added to the fit therefore constructing a simulated data set. This process was repeated 50 times, shown in Figure 2.3 b). In the portions of the diffraction pattern where there is a large discrepancy between the fit and the raw data, there is more variance in the simulated data, therefore an increased variance in the area and peak width of the phases contributing to that portion of the diffraction pattern. Figure 2.3 c) shows the mean fit across the 50 simulated data sets. Though the mean fit remains relatively unchanged the variance across all 50 fits allows for the determination of uncertainty attributed to the fitting procedure.

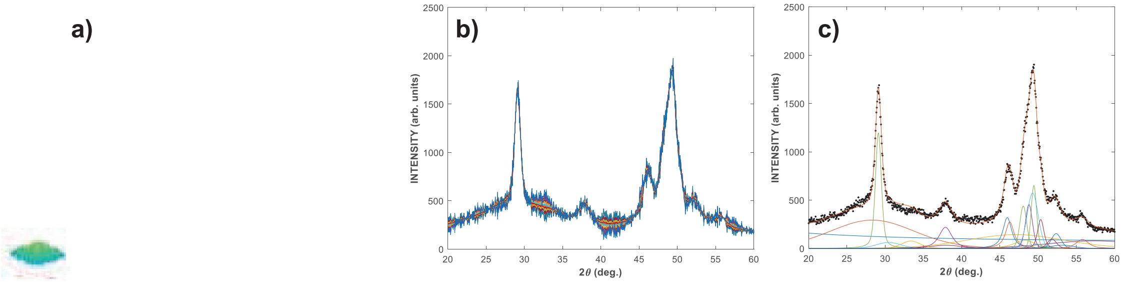

Figure 2.3 Example of Monte Carlo simulation of fitted XRD pattern to predict error a) error covariance matrix b) simulated data, c) mean fit of the 50 simulated data sets.

2.2.3 X-Ray Diffraction Instrumentation

In a laboratory setting, X-rays are generated using a sealed diode vacuum tube, this can be seen in Figure 2.4. Current is passed through a tungsten filament (cathode) generating electrons. Electrons are accelerated through a potential difference, on the order of kilovolts, and strike a metallic anode (typically copper) with kinetic energy on the order of kiloelectronvolts. If there is sufficient kinetic energy an electron is removed from the K-shell (1s orbital) of a copper atom. An electron from an outer shell of the copper atom decreases in energy in order to occupy the vacancy in the 1s orbital. Because energy is conserved a photon of equal energy must be emitted as a result of the electronic transition. Selection rules dictate that an electronic transition from the upper s and d orbitals to the 1s orbital is forbidden; therefore, two characteristic X-rays are emitted as the result of a transition from upper 2p (L shell) and 3p (M shell) orbitals to the 1s orbital (in copper). In Siegbahn notation these transitions are referred to as Kα (2p→1s) and Kβ (3p→1s, 1.39217Å).[84] However, because of spin-orbit coupling the degeneracy of the three 2p orbitals is split such that two degenerate $2p_{3/2}$ orbitals exist higher in energy than one $2p_{1/2}$ orbital, resulting in two Kα transitions referred to as $K\alpha_1$ ($2p_{3/2}$→1s, 1.54051Å)[84] and $K\alpha_2$ ($2p_{1/2}$→1s, 1.54433Å)[84]. Because there are two $2p_{3/2}$ orbitals the $K\alpha_1$ transition is twice as likely, and therefore $K\alpha_1$ radiation is twice as intense. Kβ radiation is less intense by roughly a factor of 5 (for copper),[84] therefore experimental apparatus are optimized to utilize Kα radiation rather than Kβ.

Kβ radiation is typically removed by one of two methods. The energy of the absorption edge of nickel lies between the Kα and the Kβ transition in copper such that a nickel filter will effectively absorb Kβ radiation and allow Kα radiation to pass through unabsorbed. The second method to eliminate Kβ radiation is a diffracted beam monochromator, shown Figure 2.4. A diffracted beam monochromator is a single crystal held at a constant angle such that the Bragg condition is satisfied only for the desired wavelength of radiation, in this case Kα radiation. However, because of the minute difference in energy, a diffracted beam monochromator is not able to discriminate $K\alpha_1$ and $K\alpha_2$ and both are simultaneously detected resulting in two sets of Bragg peaks. Additionally, a diffracted beam monochromator lessens the X-Ray fluorescent background. By the same process employed to generate X-rays in the sealed diode vacuum tube; incident X-rays can excite core electrons in elements (first row transition metals) present in a sample generating fluorescent X-rays. Because the diffracted beam monochromator discriminates X-rays in terms of energy a large portion of X-Ray fluorescence is eliminated, therefore reducing the detected background.

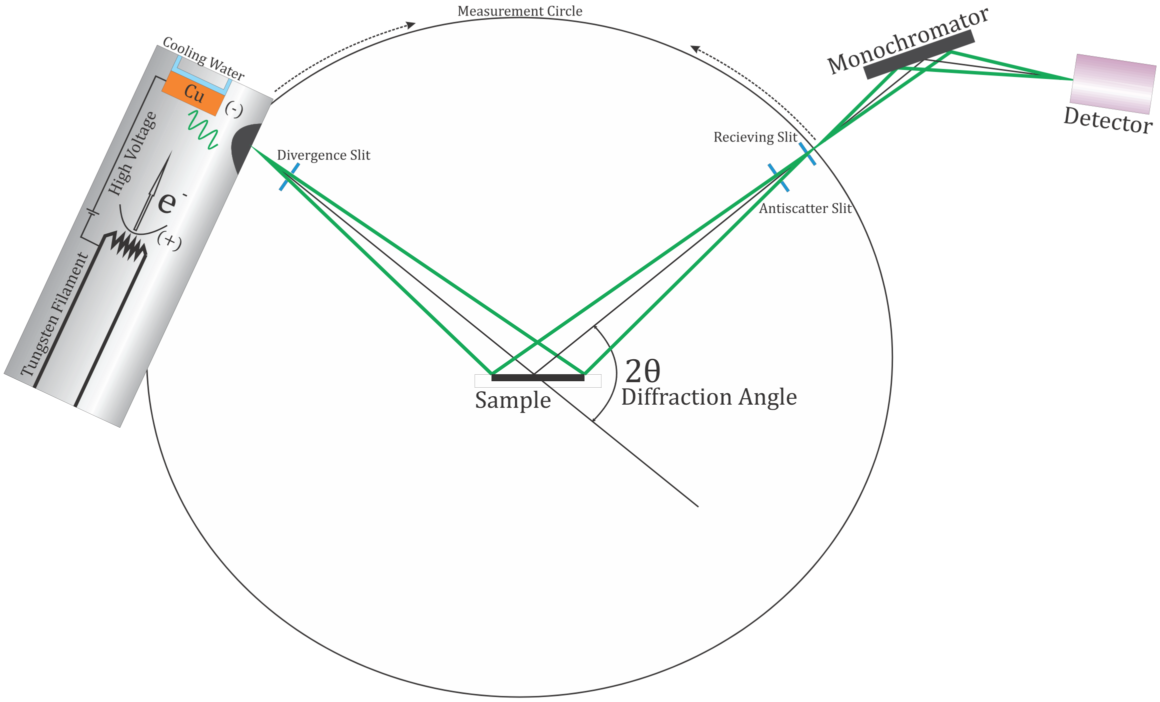

Figure 2.4 Schematic diagram of Bragg-Brentano geometry commonly used in X-Ray diffractometers.

Figure 2.4 shows the Bragg-Brentano geometry commonly used in laboratory X-Ray diffractometers. Both the X-Ray tube and the detector move simultaneously in equal increments along the measurement circle, data is therefore collected as a function of the diffraction angle, 2θ.

In this work all XRD patterns were collected using a Rigaku Ultima-IV X-ray diffractometer with Cu Kα radiation and a diffracted beam monochromater. Samples were compressed into a stainless-steel sample well of dimensions 25mm by 20mm by 3mm using a glass microscope slide. The X-ray tube was operating at 45 kV and 40 mA, and data collected at 0.05° (2θ) increments for 3-8 seconds per data point using a scintillation counter detector.

2.3 Mössbauer Spectroscopy

Mössbauer spectroscopy is a spectroscopic technique based on the recoilless absorption and emission of γ-rays by atomic nuclei and was developed by Rudolf Mössbauer in 1958 for which he received the Nobel prize in physics in 1961. The Mössbauer effect was initially observed in ^{191}Ir; since then, 100 nuclear transitions have been observed in roughly 80 nuclei, across 43 elements, of which roughly 20 elements have practical applications for analysis by Mössbauer spectroscopy.[85] Those elements include Fe, Sn, Ni, Zn, Tc, Ru, Hf, Ta, W, Os, Ir, Pt, Au, and Hg; however, the majority of publications in the field of Mössbauer spectroscopy (as well as the work presented here) focus on the characterization of Fe containing materials. Therefore, the introductory material will focus on the theory and experimental apparatus required to conduct ^{57}Fe Mössbauer spectroscopy.

^{57}Co is a radioactive isotope of Cobalt with a half life of ~270 days and is used as the radioactive source in ^{57}Fe Mössbauer spectroscopy. ^{57}Co decays by electron capture, this is a process by which a core shell electron is absorbed by a proton forming a neutron; therefore, ^{57}Co decays to an excited state of ^{57}Fe. The excited ^{57}Fe nuclei undergo a transition to the ground nuclear state emitting γ-photons with energy proportional to the nuclear transition. Using the Doppler effect, γ-photons generated by ^{57}Co are modulated such that they match the energy of the nuclear transitions of the sample ^{57}Fe nuclei. The radioactive source is moved at controlled velocities, v, (by constant acceleration) toward and away from the sample varying the energy of the γ-ray, E_γ, to match the energy of the nuclear transition of the sample shown in Equation 2.8, where E is the modulated γ-ray energy and c is the speed of light.

$$E = E_\gamma \left(1 + \frac{v}{c}\right) \tag{2.8}$$

When a nuclear transition is induced, incident γ-rays are absorbed then emitted in all directions scattering γ-photons, when in transmission geometry, away from the detector. This is observed as a decrease in counts measured by the detector. Mössbauer spectra are, therefore, typically recorded as relative intensity as a function velocity, where a decrease in intensity indicates a nuclear transition.

The observation of the Mössbauer effect is additionally enabled by the recoil free fraction (RFF). When a γ-ray is absorbed or emitted by a nucleus that nucleus recoils and some energy is lost upon absorption and emission. As a result, there is not sufficient overlap of absorption and emission energies thereby preventing the observation of nuclear resonance fluorescence. This is especially important in liquid and gaseous phases where recoil energy is large and imparted entirely on a single nucleus. In solid phases, however, recoil energy is imparted upon the entire crystallite as the nucleus resides within a rigid crystal structure and there is sufficient overlap of absorption and emission energies; though, it is important to consider that the nucleus is not stationary within the crystal structure. When a γ-ray is absorbed or emitted by a nucleus, nuclear recoil energy is transferred to a phonon (quantized periodic motion of an arrangement of atoms), thereby preventing the observation of nuclear γ-resonance fluorescence. The RFF represents a finite probability of a zero-phonon process, therefore allowing nuclear resonance fluorescence to occur.[85] Specifically, the RFF, $f=\exp(-\boldsymbol{k}^2\langle x^2\rangle)$, is the mean square vibrational amplitude of the resonating nucleus in the direction of observation for gamma rays of a wave vector $\boldsymbol{k}$. The RFF will then be a value between 0 and 1 and will proportionately scale the observed intensity of the given phase in the Mössbauer spectrum.

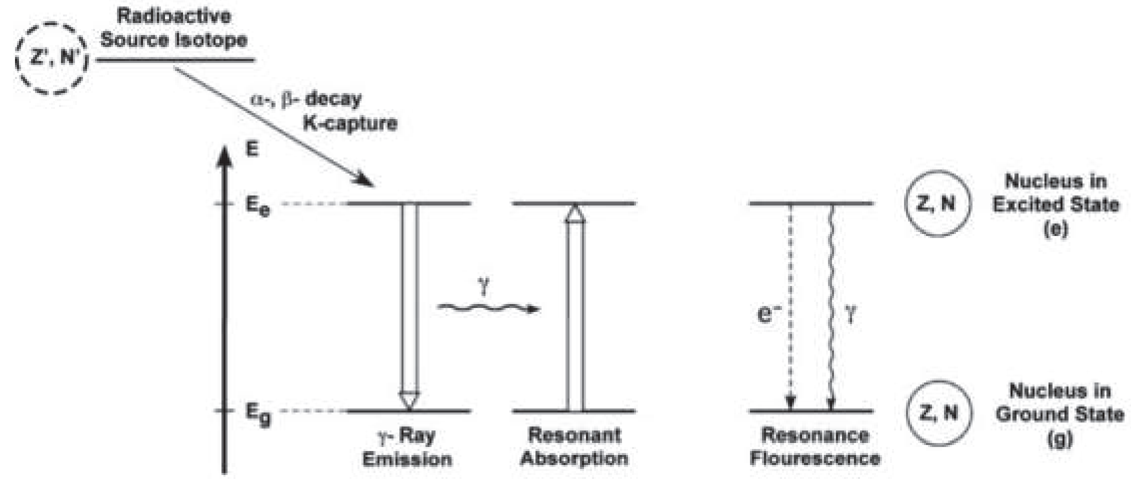

Figure 2.5 Nuclear energy levels of the source and absorber in a typical ^{57}Fe Mössbauer spectrometer. Reprinted by permission from Springer: Reference 85. Copyright 2011.

2.3.1 Mössbauer Spectroscopy Hyperfine Interactions

The utility of Mössbauer spectroscopy is the dependence of the nuclear transition energies on local electronic and magnetic environment, the hyperfine interactions.

Hyperfine interactions can be summarized by: the electric monopole interaction, changing the energy between ground and excited state such that the resonance line shifts to the left or the right; and, the electric quadrupole and magnetic dipole interactions which split the degeneracy of the nuclear energy levels leading to multi-lined spectra, each interaction will be described in detail below.

2.3.1.1 Electric Monopole Interaction

The electric monopole interaction is commonly referred to as the center shift and is the result of the coulombic interaction of the nuclear charge distribution with the electronic charge distribution at the nucleus. Over the course of a nuclear transition a change in effective size of the nucleus alters the electron-nucleus interaction energy. This change in energy cannot be measured directly; however, is typically measured relative to the 14.4 keV transition line in metallic ^{57}Fe. The isomer shift varies linearly with the electron charge density at the nucleus, shown in Equation 2.9, where δ is the isomer shift, ΔR is the change in nuclear radius following a transition from excited to ground state, R is the ground state nuclear radius, $|\psi(0)|_A{}^2$ is the electron density at the nucleus of the absorber, and C is a constant depending on the reference standard.[85]

$$\delta = const \left(\frac{\Delta R}{R}\right) \{|\psi(0)|_A^2 - C\} \tag{2.9}$$

Therefore, given $\Delta R/R$ is negative (as it is for ^{57}Fe), an increase in the observed isomer shift implies a decrease in electron density at the nucleus. Similarly, a decrease in the observed isomer shift implies an increase in electron density at the nucleus. The electron density at the nucleus originates entirely from s-electrons, as s-orbitals do not have a node at $R = 0$ and can penetrate the nucleus. By contrast p, d, and f orbitals contain a node at $R = 0$ and do not contribute directly to isomer shift; however, shielding of the nuclear potential by valence p, d and f electrons causes a contraction of the inner s-orbitals therefore indirectly modifying the isomer shift. By measuring a number of Fe compounds trends in isomer shift can be correlated to the chemical properties, this is shown in Figure 2.6.

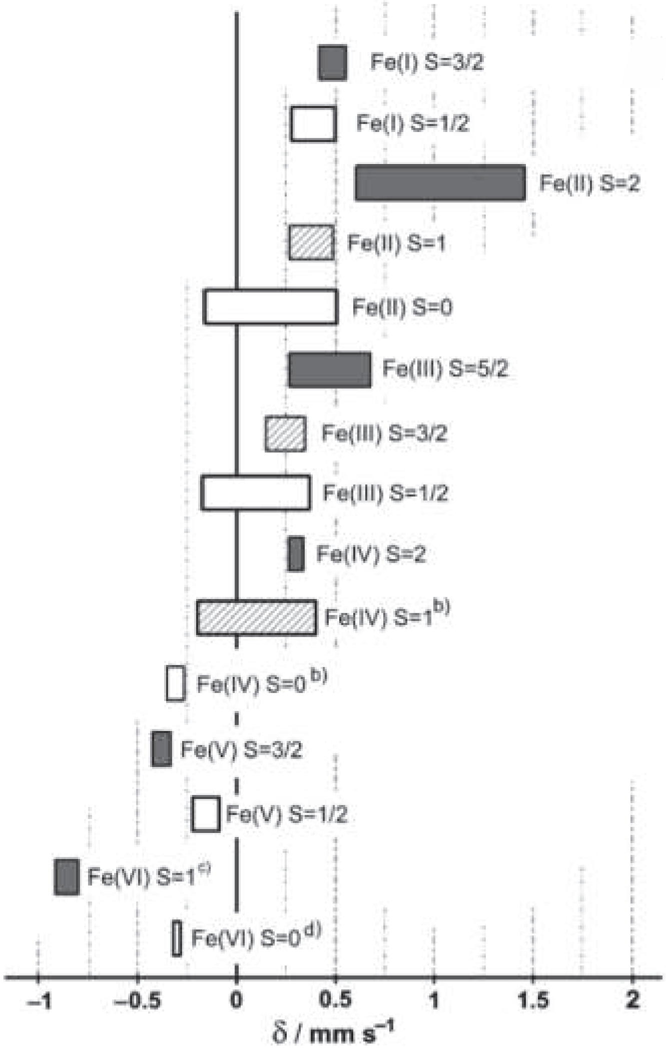

Figure 2.6 Typical isomer shift values for Fe nuclei given their oxidation state and spin state where grey, hatched, and white rectangles represent high spin, intermediate spin and low spin Fe compounds respectively. Reprinted by permission from Springer: Reference 85. Copyright 2011.

Given a high spin Fe compound, the lower the oxidation state the higher the isomer shift, this trend is represented by the dark grey rectangles. Given a low spin Fe compound, there is very little variation in isomer shift with oxidation number, and oxidation states are often indistinguishable as indicated by the white rectangles. Additionally, low spin Fe compounds typically exhibit lower isomer shift values than high spin compounds, and intermediate spin compounds often resemble their low spin counterparts (represented by the hatched rectangles).

2.3.1.2 Electric Quadrupole Interaction

The electric quadrupole interaction arises from the interaction of a non-homogeneous electronic distribution about the nucleus (the electric field gradient (EFG)) with the quadrupole moment of that nucleus. Any nucleus with a spin quantum number $I > 1/2$ (as in the first excited state of ^{57}Fe) is non-spherical and will therefore have a non-zero quadrupole moment. The energy of the electric quadrupole interaction E_Q can be calculated according to Equation 2.10 where e is the electron charge, Q is the quadrupole moment, V_{zz} is the z-component of the EFG, m_I is the magnetic quantum number where $m_I = I, I\text{-}1, \ldots -I$, and η is a parameter defining the asymmetry of the EFG about the nucleus where $0 \leq \eta \leq 1$ and 0 defines cubic symmetry.

$$E_Q = \frac{eQV_{zz}}{4I(2I-I)}\left[3m_I^2 - I(I+1)\right]\sqrt{1+\frac{\eta^2}{3}} \tag{2.10}$$

Therefore, given that m_I is squared in, the electric quadrupole interaction will split the degeneracy of the $I = 3/2$ excited state into two non-degenerate excited states where the $m_I = \pm 3/2$ are increased in energy by E_Q and the $m_I = \pm 1/2$ are decreased in energy by E_Q. This gives rise to a Mössbauer spectrum with two peaks, referred to as a quadrupole split doublet. The quadrupole splitting, Δ, is defined as the distance between the two peaks (typically in mm/s), and it can therefore be shown that $\Delta = 2E_Q$.

2.3.1.3 Magnetic Dipole Interaction

Given a nucleus with a spin quantum number $I > 0$, that nucleus will interact with any magnetic field by its magnetic dipole moment; also known as the Nuclear Zeeman effect. The magnetic dipole interaction can result from either an internal magnetic field (as in the case of metallic ^{57}Fe) and/or, an applied magnetic field. This interaction splits the degeneracy of the nuclear state into $2I + 1$ states with energy separation, E_m, dependant upon the magnetic quantum number m_I. This is shown in Equation 2.11 where μ is the magnetic dipole moment, B is the magnetic induction, and g_N is the nuclear Landé factor, and and μ_N is the nuclear magneton.

$$E_m = \frac{-\mu B m_I}{I} = -g_N \mu_N B m_I \tag{2.11}$$

The magnetic dipole moment, μ, can be related to the nuclear magneton, μN, by the nuclear Landé factor gN according to the relationship $\mu = gN\, \mu N\, I$.

In the case of ^{57}Fe the ground state spin quantum number is $I = 1/2$, this state is then split into two non-degenerate states given $m_I = \pm 1/2$. The excited state with a spin quantum number of $I = 3/2$ is then split into four non-degenerate states given $m_I = \pm 3/2, \pm 1/2$. Selection rules for nuclear transitions dictate that an allowed transition is given by $\Delta I = 1$, and $\Delta m_I = 0, \pm 1/2$, therefore leading to six allowed transitions and a six-line spectrum. The transition probabilities will vary depending on the spin and parity of the ground and excited states as well as the geometric configuration of the magnetic field with respect to the direction of observation which can be defined by the square of the appropriate Clebsch-Gordan coefficients.[85] For example, given a homogeneous magnetic field relative to the direction of observation, the ratio of transition probabilities will be, from lowest to highest energy transition, 3:2:1:1:2:3. However, when the magnetic field is perpendicular to the direction of observation the ratio of transition probabilities will be, from lowest to highest energy, 3:4:1:1:4:3.

2.3.2 Mössbauer Spectroscopy Experimental Apparatus

The Mössbauer drive unit consists of a radioactive source mounted on a rod suspended by disc springs allowing motion in one-dimension toward and away from the sample and detector. Within the rod are two magnets surrounded by two external coils, a drive coil and a pickup coil. As current flows through the drive coil a magnetic force is generated causing motion of the rod, and therefore the source. Using a digital function generator, current is increased and decreased linearly in a triangle wave fashion from some maximum value, $+I_o$, to some minimum value $-I_o$; therefore, resulting in an identical response in velocity, from $+v_o$ to $-v_o$ shown in Figure 2.6. As the drive unite moves a current is generated in the pickup coil via induction and the true motion of the drive unit is measured as a function of current. If the measured current deviates from the reference current, the difference results in a correction signal, pushing the drive in the opposite direction ensuring that the true drive motion matches that of the digital function generator.

γ-rays modulated by the drive unit pass through the sample and toward the detector. If the energy of the γ-ray matches that of the nuclear transition of the 57Fe nuclei present in the sample, γ-rays are scattered in all directions and a decrease in intensity is observed by the detector. Detectors are typically gas-filled proportional counter detectors. An inert counting gas (krypton) as well as a quenching gas (methane) is contained within a cylinder with a beryllium window to allow the transmission of γ-rays. A wire runs through the center of the cylinder and potential difference of 1.5-2.0 kV is established between the wire and the walls of the cylinder. The energy of the incident γ-ray is great enough to ionize counting gas molecules, the electron produced from gas molecule ionization is directed to the central wire and the positively charged gas molecules to the wall of the detector. As the electron travels to the wire it is accelerated by the potential difference and, in a cascade reaction, continues to ionize additional gas molecules. As electrons strike the wire a current is generated therefore enabling the detection of γ-rays.

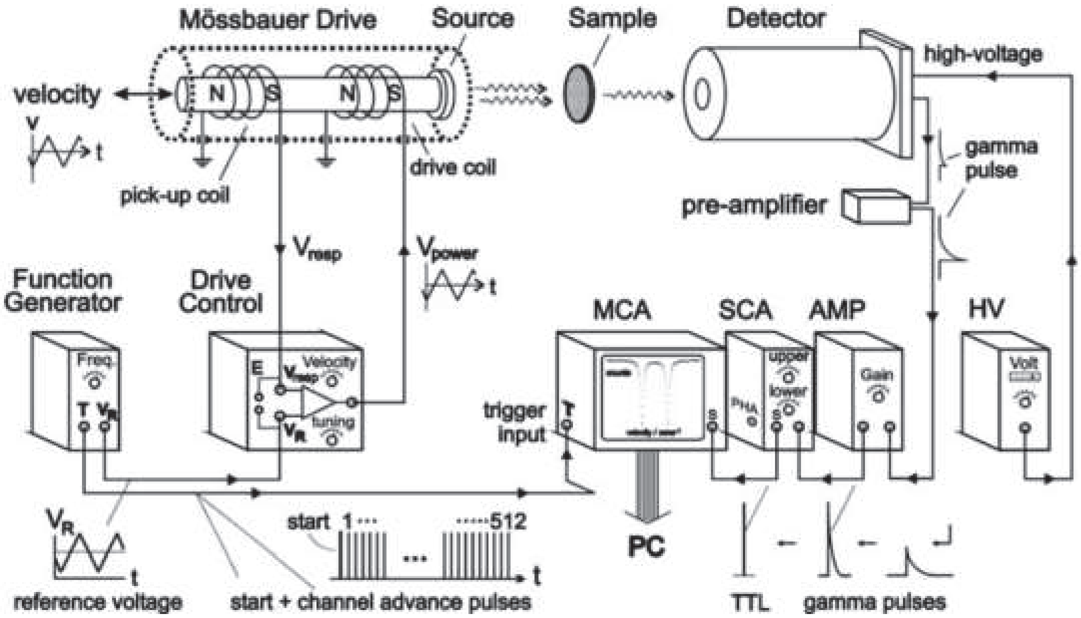

Figure 2.7 Experimental apparatus for a typical Mössbauer spectrometer in transmission geometry. Reprinted by permission from Springer: Reference 85. Copyright 2011.

The multi-channel analyser (MCA) allows each detection event to be recorded synchronously with velocity. When the source velocity is equal to the minimum velocity, $-v_o$, data collection is initialized and the first channel in the MCA is opened. The velocity range is divided into 1028 increments, or, channels. When velocity exceeds the velocity range for a given channel, that channel is closed, and the following channel is opened. This continues until the source velocity reaches the maximum value, $+v_o$, then swept back to the minimum value in a triangle wave fashion, while data is continuously collected. When a channel is open, counts from the detector are recorded, and over the course of thousands to millions of velocity sweeps, enough counts have accumulated in each channel to form a suitable Mössbauer spectrum. The triangle wave variation of velocity results in two symmetric Mössbauer spectra which must be folded in order to form a single spectrum. The folding point is the channel at which $+v_o$ is recorded and is typically located at the center of the spectrum (channel 512). Folding is a pairwise average of the data about the folding point and increases signal to noise ratio by a factor of $\sqrt{2}$. Channel number is then correlated to velocity by the spectrum of a known reference material (typically α-Fe foil).

The emission spectrum of the ^{57}Co source is rather complex. ^{57}Co decays to the 136 keV excited state of ^{57}Fe. The 136 keV state of ^{57}Fe decays to the ground state in one of two ways, by emission of a 136 keV γ-photon (15%), or by the two-step emission of a 122 keV γ-photon, followed by the emission of a 14.4 keV γ-photon (85%). The 14.4 keV γ-photon is the desired Mössbauer radiation used to induce nuclear transitions in sample nuclei. The 14.4 keV excited state, however, has a high probability of decaying by internal conversion (~0.9). Internal conversion is the process by which X-rays are generated where an electron from the 2p orbital transitions to the 1s orbital to fill the hole following electron capture; therefore, generating an Fe Kα X-ray. This necessitates the discrimination of incoming radiation at the detector to reduce the counts attributed to undesired photons from the decay scheme of ^{57}Co. This is handled by pulse-height analysis (PHA) and a single-channel analyser (SCA). Electric output pulses in the γ-detector are amplified and shaped such that the pulse height is proportional to energy and the emission spectrum of ^{57}Co can be measured as a function of voltage. The SCA then imposes a voltage barrier such that only pulses at the voltage which the 14.4 keV transition is detected are counted by the

MCA. Without PHA and a SCA the noise generated by the non-resonant background radiation prevents the detection of nuclear γ-resonance.

2.4 Electrochemical Characterization

Electrochemical characterization of new materials is typically carried out in half cells. Half cells are easy to make and evaluate especially on a small scale. Because there is a large excess of Li-ions and electrolyte, the observed electrochemical performance is directly related to the performance of electrode material being tested. As shown in Figure 2.8, half cells consist of an electrode and a Li-metal counter electrode separated by a polymer separator; allowing the transfer of Li-ions from positive to negative electrode, while simultaneously preventing an internal short. Spacers ensure an appropriate stack pressure is maintained, such that all components of the cell can remain in electrical contact, while the gasket prevents leaks and contact of the external cell housing, preventing an external short.

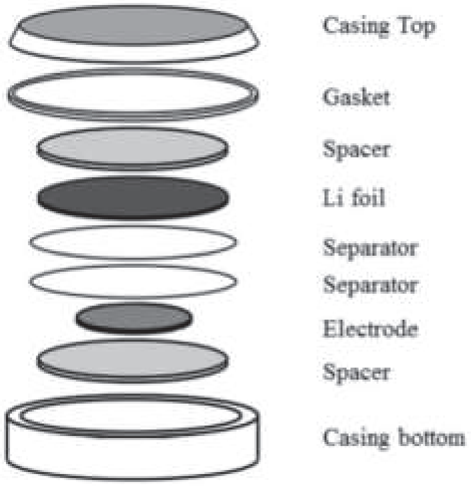

Figure 2.8 schematic diagram of a deconstructed view of a typical 2325 type coin cell.

2.4.1 Cell Construction

Electrode slurries were prepared in distilled water at a volume ratio of 70/25/5 Fe-Si alloy/LiPAA (neutralized polyacrylic acid solution (Sigma-Aldrich, average molecular weight 250000 g/mole, 10 wt% in H_2O) with $LiOH·H_2O$ (Sigma-Aldrich, 98%) in distilled water)/Carbon black (Imerys Graphite and Carbon, Super C65). The slurry was mixed for one hour on a Retsch PM200 planetary mill at 100 rpm with 2 13mm WC balls and spread using a stainless-steel coating bar with a gap of 10.2 μm onto electrolytic copper foil (Furakawa Electric, Japan). Prior to cell assembly the electrodes were heated under vacuum for >1 hour at 120 ºC.

Electrodes were assembled in 2325-type coin cells with a lithium metal counter/reference electrode separated by two layers of Celgard 2300. Electrolyte salt consisted of 1 M LiPF6 (BASF) in a solution of EC/DEC/FEC (BASF) at a volume ratio of 3/6/1 and the cell was constructed under an inert argon atmosphere. Two coin cells were constructed for each sample, and cycled galvanostatically at 30.0 ± 0.1 ºC from 900 mV to 5 mV on a Maccor series 4000 Automated Test System at a rate of C/10 for the first cycle and C/5 for the following cycles. C-rate is the magnitude of the current, expressed with respect to time desired for a charge or discharge half-cycle. By dividing the theoretical capacity of the cell by the desired charge/discharge time, the cycling current is calculated. Therefore, a C/10 rate implies that it will require 10 hours for a single charge or discharge half cycle, and the cycling current will be 1/10 the theoretical capacity of the cell.

2.5 Gas Pycnometry

Gas pycnometry is a technique used to determine the true density of, often powdered, samples. By using an inert gas, the total volume of a powdered sample can be determined therefore, this and an accurate measurement of the sample mass allows the calculation of sample density.

Gas pycnometry is typically performed with helium or argon gas, where an inert gas of small particle size is paramount, such that any pores, cracks, or internal voids can be filled, and true volume can be determined. The powdered sample is placed inside a chamber of known volume, V_c. An inert gas is added until a pre-defined pressure, P_1, is measured by a pressure transducer. A valve is opened connecting the sample chamber to a reference chamber of known volume, V_r. Following the expansion of the gas a second pressure, P_2, is measured. This allows the determination of the sample volume, V_s, by Equation 2.12. A schematic diagram of a gas displacement pycnometer is additionally shown in Figure 2.9.

$$V_s = V_c + \frac{V_r}{1-\frac{P_1}{P_2}} \tag{2.12}$$

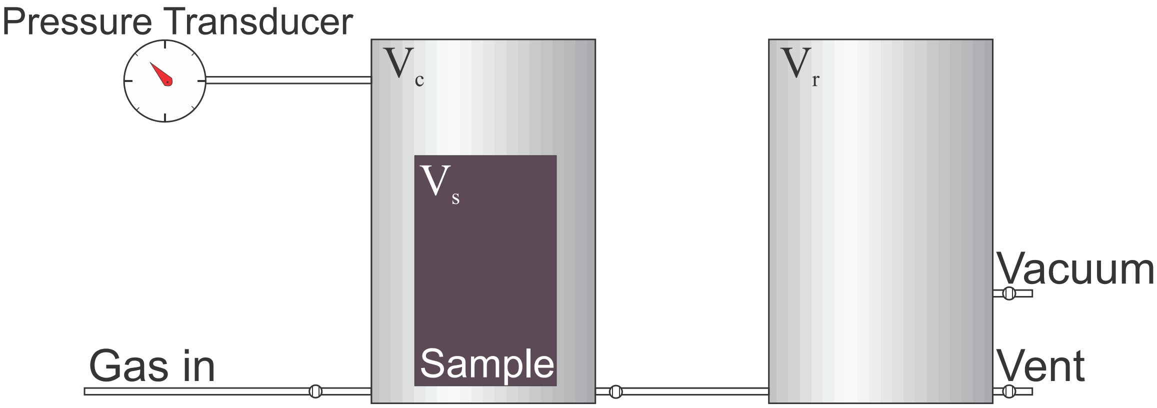

Figure 2.9 Schematic diagram of a gas displacement pycnometer.

In this research a Micromeretics AccuPyc II 1340 gas displacement pycnometer was used. The inert gas of choice was helium. Volume was determined over 5 cycles, following 10 purging cycles.

2.6 Inductively Coupled Plasma – Optical Emission Spectroscopy

Inductively Coupled Plasma – Optical Emission Spectroscopy (ICP-OES) is a technique used to quantify atomic composition of aqueous samples. When an atom is ionized, a valence electron is removed therefore emitting a photon proportional to the energy transition of that electron. Elements can not only be characterized by this ionization energy; but, can be additionally quantified according to the intensity of detected photons. An ICP torch can reach temperatures required to provide sufficient energy to ionize most elements, therefore enabling OES.[86]

In this work, ICP-OES analysis was performed in 2% nitric acid. Depending on sample solubility, samples were either directly dissolved in 2% nitric acid, or if solubility was low in 2% nitric acid, samples were dissolved in 70% nitric acid and diluted in distilled water by a factor of 35. Elemental composition was determined by generating a calibration curve of known concentrations of the elements of interest. In this case the only element of interest was Fe. A stock solution of 1000 mg/mL was diluted such that three calibration standards at a concentration of 0.2 mg/mL, 2 mg/mL, and 20 mg/mL. Samples with an unknown Fe content were prepared such that Fe content was roughly 10 mg/mL. ICP-OES analysis was performed using a PerkinElmer Optima 8000 ICP optical emission spectrophotometer.

2.7 Scanning Electron Microscopy – Energy Dispersive Spectroscopy

The introduction of the light microscope in the 1600's allowed the magnification of biological material using light and glass lenses. Early light microscopes were limited in resolution by the ability of the lens maker to fabricate smooth and perfect lenses. Resolution is, however, inherently limited by the wavelength of light such that nothing smaller than the wavelength of light can be resolved. By using high energy electrons (>1000 keV) the wavelength (<1.2 nm) is considerably less than that of visible light, and therefore resolution is no longer limited by the wavelength of light, and depending on the SEM, features on the nm scale can be resolved.

Electrons are generated by passing a current through a tungsten filament. Electrons are then accelerated through a potential difference >1000 keV. The electron beam is rastered across the sample and an electron image is generated in one of two ways, by the detection of secondary electrons (SE) or the detection of backscattered electrons (BSE). When electrons of sample atoms interact with the electron beam low-energy secondary electrons are emitted from the valence or conduction bands. Secondary electrons are directed towards a detector by a potential bias generating a SE image of the topography of the sample. A BSE image, however, is generated as high energy electrons of the electron beam strike the sample, penetrating to a depth of ~1 μm, and are scattered. Scattered electrons are detected by a detector above the sample generating a BSE image. Additionally, information on composition can be acquired by the intensity of BSE. Since incident electrons are scattered by electrons of the atoms in the sample, an atom with more electrons will scatter more electrons in the direction of the detector and appear brighter in the image. An atom in the sample with fewer electrons will appear darker, as fewer electrons are scattered in the direction of the detector.

Energy-dispersive X-ray spectroscopy (EDS) is often applied in SEM in order to quantify sample composition by X-rays emitted. When a high energy electron strikes an atom with sufficient energy a core electron is removed. A higher energy electron will occupy the hole left by the removed electron, thereby emitting an X-ray of energy proportional to that transition. There are multiple allowed transitions leading to the generation of characteristic X-rays, depending on the atomic composition of the sample. EDS can then be used to generate a composition analysis map of the image generated by the SEM. The ability of EDS to quantify composition is inherently limited by electron beam spot size as well as the nature of the sample. The composition analysis is performed as the electron beam is rastered across the sample; therefore, as spot size increases resolution will decrease, and as spot size decreases resolution will increase. Additionally, an ideal sample is smooth, flat, and must remain perpendicular to the electron beam.

In this work SEM images were collected using a TESCAN MIRA 3 field-emission scanning electron microscope. Samples were adhered to a conductive carbon tape and images were collected at an accelerating potential of 15 kV.

Chapter 3 **Si-TM Alloys**

3.1 Fe

Iron, because of its abundance in the earth's crust and relative low cost, is an ideal candidate inactive component for Si alloys employed in LIBs. The Fe-Si system has been evaluated previously in sputtered thin films;[87–89] however, at this time, sputtering is too expensive to be performed on a commercially relevant scale. The Si-Fe system has also been evaluated by ball milling,[46,90,91] the work done by Lee et. al fabricated electrodes using PVDF as a binder and showed poor capacity retention,[90] the work done by Dong et. al used $BaSi_2$ as a component in the inactive matrix to increase ductility, and fabricated electrodes using PTFE as a binder, and similarly showed poor capacity retention.[91] The work done by Li et. al used a commercial $FeSi_2$ precursor with excess silicon using mechanical milling only to mix graphite and reduce grain size, fabricated electrodes using a PTFE binder, and again showed poor capacity retention.[46] Advances in binder chemistry have resulted in significant improvement in capacity retention of alloying negative electrodes by focusing on water based poly-carboxylic acid binders, including carboxymethyl cellulose (CMC)[43–49] and poly acrylic acid (PAA).[36,40–42] Therefore, it is important to revisit the Fe-Si system employing ball milling as a commercially relevant synthetic technique and evaluating the electrochemical performance using a modern high performance binder, such as PAA.

In this study, ^{57}Fe Mössbauer spectroscopy and XRD was used to quantify mechanochemical reactions. Mössbauer spectroscopy is a spectroscopic technique based on the recoil-free absorption and emission of γ-rays by a nucleus probing the local electronic and magnetic environment. As opposed to XRD, Mössbauer spectroscopy is able to detect nano-crystalline phases with short-range order that are formed when powders are mechanically alloyed.[92]

3.1.1 Experimental

$Si_{100-x}Fe_x$ alloys were prepared by loading 0.5 mL (calculated from bulk densities) of stoichiometric amounts of Si and Fe powder, required masses shown in Table 3.1, into a 65 mL hardened steel milling vial (SPEX SamplePrep, NJ) with 180g of 1.6 mm stainless steel milling balls, sealed under an argon atmosphere and milled with a high energy ball mill (8000D Mixer/Mill, SPEX SamplePrep, NJ) under conditions optimized to form amorphous alloys, as described in a previous study.[81] Precursor powders were Si (-325 mesh Sigma-Aldrich, 99.9%) and Fe (<10 µm Alfa-Aesar, 99.9%). Two series of alloys were prepared, first with varying composition (x=10, 15, 20, 25, 30) a fixed 8 hour milling time; and, secondly, at a fixed $Si_{85}Fe_{15}$ composition with different milling times: 6, 12, 18, 24, 30, 36, 42, 48, 54 minutes, and 2, 4, 8, and 16 hours.

Table 3.1 Mass of Si and Fe precursor required for a total volume of 0.5 mL.

Composition	Si (g)	Fe (g)
$Si_{90}Fe_{10}$	1.093	0.241
$Si_{85}Fe_{15}$	1.055	0.370
$Si_{80}Fe_{20}$	1.015	0.505
$Si_{75}Fe_{25}$	0.974	0.645
$Si_{70}Fe_{30}$	0.930	0.793

XRD patterns were collected using a Rigaku Ultima IV diffractometer with a Cu kα X-ray source operating at 45 kV and 40 mA and a diffracted beam monochromater. Patterns were collected from diffraction angle of 20° to 60° at 0.05° increments 8 seconds per increment. ^{57}Fe Mössbauer spectroscopy was performed using a spectrometer (SEE Co., Minneapolis, MN) operating in a constant acceleration mode with a Rh ^{57}Co source.

Velocity scale was calibrated according to the α-Fe spectrum. SEM images were collected using a field-emission scanning electron microscope (MIRA 3, TESCAN, Kohoutovice, Czech Republic).

Electrode slurries were prepared in distilled water at a volume ratio of 70/25/5 Fe-Si alloy/LiPAA (neutralized polyacrylic acid solution (average molecular weight 250000 g/mole, 35 wt% in H_2O, Sigma-Aldrich) with $LiOH \cdot H_2O$ (Sigma-Aldrich, 98%) in distilled water)/carbon black (Super C65, Imerys Graphite and Carbon). The slurry was mixed for one hour with a planetary mill (PM200, Retsch) at 100 rpm with two 13 mm WC balls and spread to a thickness of 10.2 μm using a stainless-steel coating bar onto electrolytic copper foil (Furakawa Electric, Japan). Prior to cell assembly the electrodes were heated under vacuum for >1 hour at 120 ºC.

Electrodes were assembled in 2325-type (23 mm in diameter and 2.5 mm in height) coin cells with a lithium metal counter/reference electrode separated by two layers of separator (Celgard 2300). Cells were constructed in an Ar-filled glove box. Electrolyte salt consisted of 1 M $LiPF_6$ in a solution of EC/DEC/FEC (battery grade, all from BASF) in a volume ration of 3/6/1. Two coin cells were constructed for each sample, and cycled galvanostatically at 30.0 ± 0.1 ºC from 900 mV to 5 mV with a battery charger (Series 4000 Automated Test System, Maccor, Tulsa, OK) I at a rate of C/10 for the first cycle and C/5 for the following cycles. Here C-rate is calculated based on all the iron in the alloys reacting to form inactive $FeSi_2$ and the excess Si having a theoretical capacity of 3578 mAh/g, according to $Li_{15}Si_4$ being the fully lithiated state of Si.

3.1.2 Results and Discussion

3.1.2.1 Structural Characterization

There are two thermodynamically stable polymorphs of $FeSi_2$: α-$FeSi_2$, stable above 915 °C; and β-$FeSi_2$, stable below 915 °C. These phases are shown in the Si-Fe binary phase diagram in **Error! Reference source not found.**. Diffraction patterns of mechanically alloyed Si-Fe alloys are often more complex than the equilibrium phases predicted from the binary phase diagram. The utility of mechanical alloying is to form nano-meter sized grains as good electrochemical performance can be directly linked to an amorphous microstructure in order to suppress the formation of $Li_{15}Si_4$ and prevent the pulverization of alloy particles upon electrochemical lithiation. Mechanical alloying, however, is not an equilibrium process, as a result of the large impact energy, and the formation of metastable phases not observed in the binary phase diagram as well as the formation of phases in violation of the Gibb's phase rule are often observed. significantly.

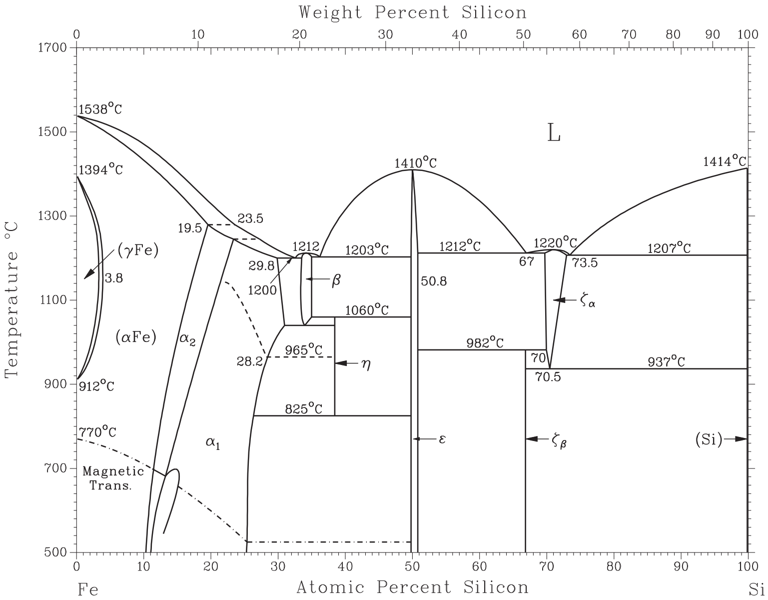

Figure 3.1 Binary phase diagram Fe and Si.

Additionally, high energy impact can introduce disorder, defects, and strain in the crystal structure all of which will cause the observed diffraction pattern to differ from the expected diffraction pattern containing the equilibrium phases. An SEM images of $Si_{85}Fe_{15}$ alloys are shown in Figure 3.2 to show the change in particle morphology following ball milling. In Figure 3.2 a) shows the un-milled Si and Fe precursors powder morphology and b) shows the Si and Fe alloy powder morphology following 8 hours of milling where particle size is reduced.

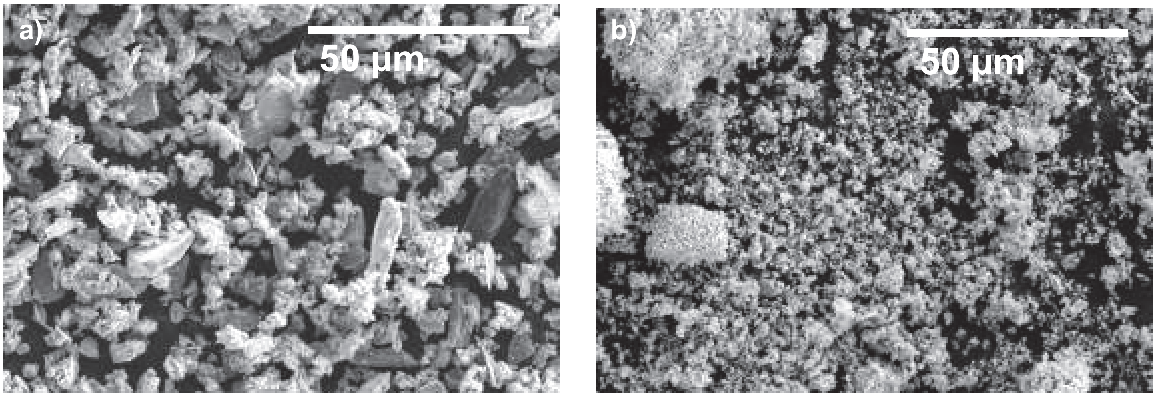

Figure 3.2 SEM images of $Si_{85}Fe_{15}$ alloy a) un-milled precursor powders and b) following 8 hours of milling

In the case of β-$FeSi_2$, a deviation from the expected diffraction pattern is observed when mechanically alloyed. Yamane et al. showed that when β-$FeSi_2$ was generated by a low temperature (600 ºC), and high temperature (900 ºC) reaction of Si and Fe precursors differing XRD patterns were observed. When generated at a low temperature, the 221, 312, and 421 reflections in β-$FeSi_2$ XRD patterns were less intense and more broad than expected from theory. The diffraction pattern of low temperature β-$FeSi_2$ closely resembles that of mechanically alloyed β-$FeSi_2$ with a systematic decrease in peak intensity of the $k + l \neq 2n$ reflections. The experimental diffraction pattern of high temperature β-$FeSi_2$, however, can be fitted by calculating the diffraction pattern using the known crystal structure.[93] It was then shown that the systematic decrease in the $k + l \neq 2n$ reflections in low temperature and mechanically alloyed β-$FeSi_2$ was the result of planar stacking faults.[93]

In addition to stacking faults, when grain sizes are reduced to nano-meter scales often there is not enough long-range order present to generate a distinct XRD pattern. X-ray scattering from a set of nuclei can be calculated according to the Debye scattering formalism shown in Equation 3.1, where I is scattered intensity, f is the atomic scattering factor, k is $4\pi\sin(\theta)/\lambda$, m and n are the indices representing two atoms, and r_{mn} is the distance between atoms m and n.[94–96]

$$I = \sum_m \sum_n f_m f_n \frac{\sin(k*r_{mn})}{k*r_{mn}} \tag{3.1}$$

Scattered intensity according to the Debye scattering formalism is then related only to the distance from each atom to every other atom in the system. Scattered intensity will begin to resemble the crystalline diffraction pattern as the number of atoms in the model is increased; however, when grain size is small, and the calculation is performed with a small number of atoms scattered intensity will differ from the crystalline diffraction pattern. This is especially true for ball milled Si shown in Figure 3.3.

Shown in the top panel of Figure 3.3 a) when the scattering calculation is performed for a set of atoms forming a single unit cell two peaks, rather than three, are observed as the 220 and 311 peaks merge forming a single peak. However, when the calculation is performed extending the number of atoms to a 2 × 2 × 2 set of unit cells, the 220 and 311 peaks split into two clearly distinguishable peaks. Figure 3.3 shows the results when b) the experimental XRD pattern is fit with three broad pseudo-Voigt curves corresponding to the reference pattern, and c) when two curves corresponding to the Debye scattering model are used. Additionally, three pseudo-Voigt curves corresponding to the crystalline reference pattern are used in both cases to fit c-Si (as some c-Si remains post milling). By using the Debye scattering model, the fit is improved considerably.

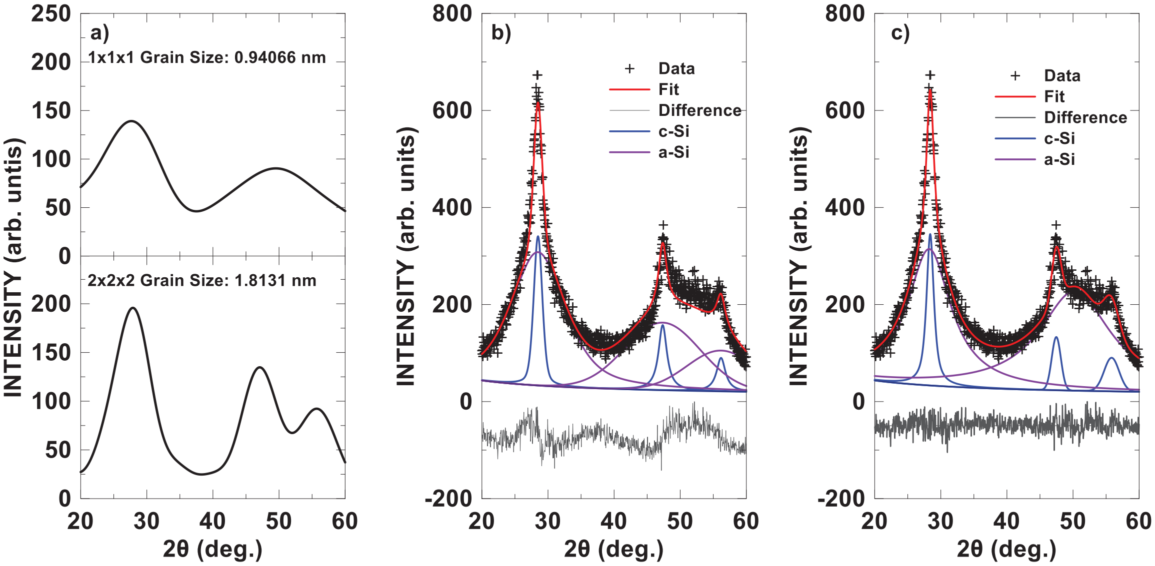

Figure 3.3 a) Debye scattering calculation for a set of Si atoms, b) fit of XRD pattern of ball milled Si using crystalline diffraction for a-Si and c-Si, and c) fit of XRD pattern of ball milled Si using the Debye scattering model a-Si and crystalline diffraction pattern for c-Si.

Two conclusions can be drawn from this exercise. The first is that the grain size of a-Si is considerably smaller than that predicted by the Scherrer equation. According to the Debye scattering model grain size must be <1 nm in order for the 220 and 311 peaks to merge. When the grain size is calculated strictly by peak width using the Scherrer equation a value of ~2 nm is found. This highlights the inability of the Scherrer equation to accurately predict grain sizes for such broad peaks. Grain size values calculated by the Scherrer equation are, therefore, not absolute and only serve as a qualitative correlation of peak width to grain sizes. The second is that a-Si should be fitted with a set of two peaks rather than the three suggested by the crystalline Si XRD pattern. Therefore, in the analysis of the following experimental diffraction patterns a-Si will be fitted with a set of two peaks rather than three. The Debye scattering model will be later used to consider the phases formed Si-Fe alloys, as the small grain sizes formed often cause the observed diffraction pattern to vary from the theoretical diffraction pattern.

A series of $Si_{100-x}Fe_x$ ($10 \leq x \leq 30$) alloys were produced where milling time was constant at 8 hours and Fe content was varied in order to determine the effect of Fe content on phase formation. Figure 3.4 a) shows all diffraction patterns collected as a function of Fe content. All alloys in this series form an amorphous Si phase, a β-$FeSi_2$ phase, and the high temperature metastable α-$FeSi_2$ phase. This represents a non-equilibrium condition that is not predicted by the Fe-Si phase diagram and is also a situation which violates the Gibbs' Phase Rule. A qualitative analysis of phase formation as a function of Fe content was performed by fitting the diffraction pattern shown in Figure 3.4 b) with pseudo-Voigt peak functions representative of the expected XRD peaks of each phase.

In Figure 3.4 c) the relative quantity of each phase is plotted as a function of Fe content. Mechanically alloyed $Si_{90}Fe_{10}$ results in the nearly exclusive formation of α-$FeSi_2$ with a small quantity of β-$FeSi_2$. β-$FeSi_2$ in this case, however, does not match the known reference pattern. By fitting the $Si_{90}Fe_{10}$ XRD pattern using only a-Si and α-$FeSi_2$ the error vector representing the difference between the data and the fit can be attributed to β-$FeSi_2$, shown in Figure 3.5 a). By using the Debye scattering formalism, the scattering profile of β-$FeSi_2$ was calculated considering the atoms which form a single 1 × 1 × 1 unit cell. This scattering profile was then compared to the error vector shown in Figure 3.5 b). There is a positive correlation between the calculated scattering profile of β-$FeSi_2$ and the error vector. Peaks that are present in locations not predicted by the reference XRD pattern can be explained by the Debye scattering calculation, and additionally the lack of intensity at positions where the reference diffraction pattern would predict peaks can also be explained. This therefore implies that at low Fe contents the formation of small grain sized β-$FeSi_2$ is preferred.

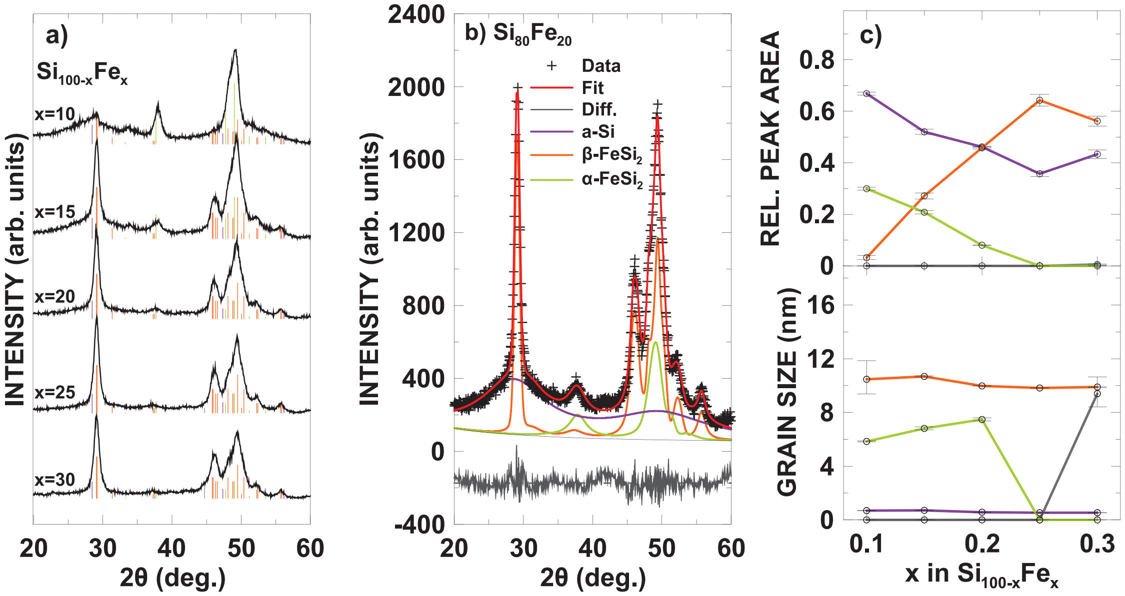

Figure 3.4 a) XRD patterns of all of the alloys formed in the $Si_{100-x}Fe_x$ series, b) an example fit of the $Si_{90}Fe_{10}$ alloy, and c) the fitting results showing relative phase intensity and approximate grain size.

There is a roughly linear dependence on the formation of the α and β-$FeSi_2$ as Fe content is varied. β-$FeSi_2$ increases with increasing Fe content, and α-$FeSi_2$ decreases with increasing Fe content. At a composition of $Si_{75}Fe_{25}$ and higher Fe contents β-$FeSi_2$ is observed exclusively. It should be noted, however, that in this case it is not small grain size β-$FeSi_2$ and the observed diffraction pattern matches the diffraction pattern observed by Yamane et al. with a systematic absence of $k + l \neq 2n$ reflections.[93] No c-Si peaks are observed in any of the diffraction patterns. All c-Si is converted to a-Si and only broad peaks are observed. Grain size was also calculated according to the Scherrer equation, as seen in the bottom panel of Figure 3.4 c), grain size as calculated by the Scherrer equation does not vary considerably as a function of Fe content. However, when considering β-$FeSi_2$ in $Si_{90}Fe_{10}$ grain size must be < 1.5 nm in order for the calculated scattering profile to match the observed diffraction pattern. This is considerably smaller than ~10 nm as determined by the Scherrer equation. In all other compositions the diffraction pattern of β-$FeSi_2$ matches the theoretical diffraction with the presence of a planar stacking fault.

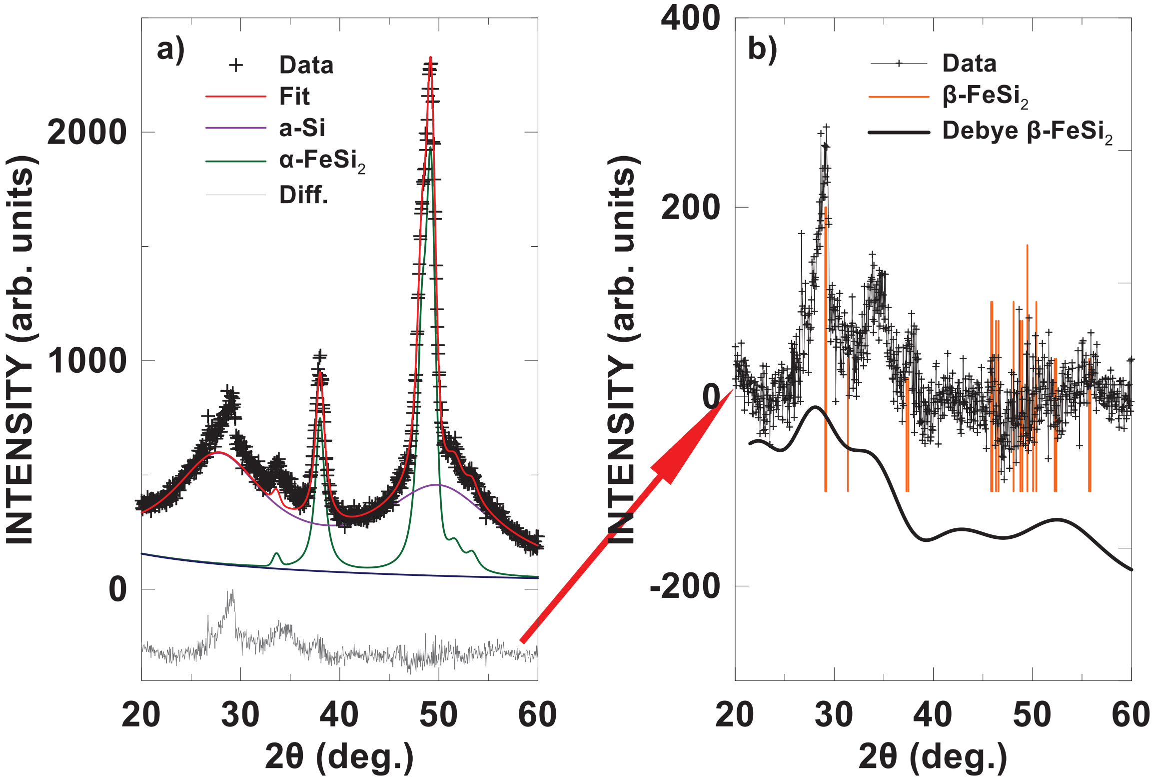

Figure 3.5 a) Fit of XRD pattern $Si_{90}Fe_{10}$ using only a-Si and α-$FeSi_2$ and b) comparison of difference from a) and Debye model calculation for β-$FeSi_2$.

In order to evaluate the Si-Fe mechanochemical reaction kinetics, a single composition of $Si_{85}Fe_{15}$ was selected and a series of alloys were produced where milling time was varied from 0.1 to 0.2, 0.3, 0.4, 0.5, 0.6, 0.7, 0.8, 0.9, 1, 2, 4, 8, and 16 hours. Diffraction patterns were fitted using pseudo-Voigt functions in order to determine the relative integrated intensity of each phase. In Figure 3.6 a detailed fit is shown for the alloys produced when milling time was 0.1-4 hours, in Figure 3.9 a summary relative integrated intensity of all phases is shown. In the initial stages of milling after 0.1 and 0.2 hours no mechanochemical reaction has occurred and the experimental diffraction pattern can be fitted well with only peaks corresponding to a-Si, c-Si and Fe.

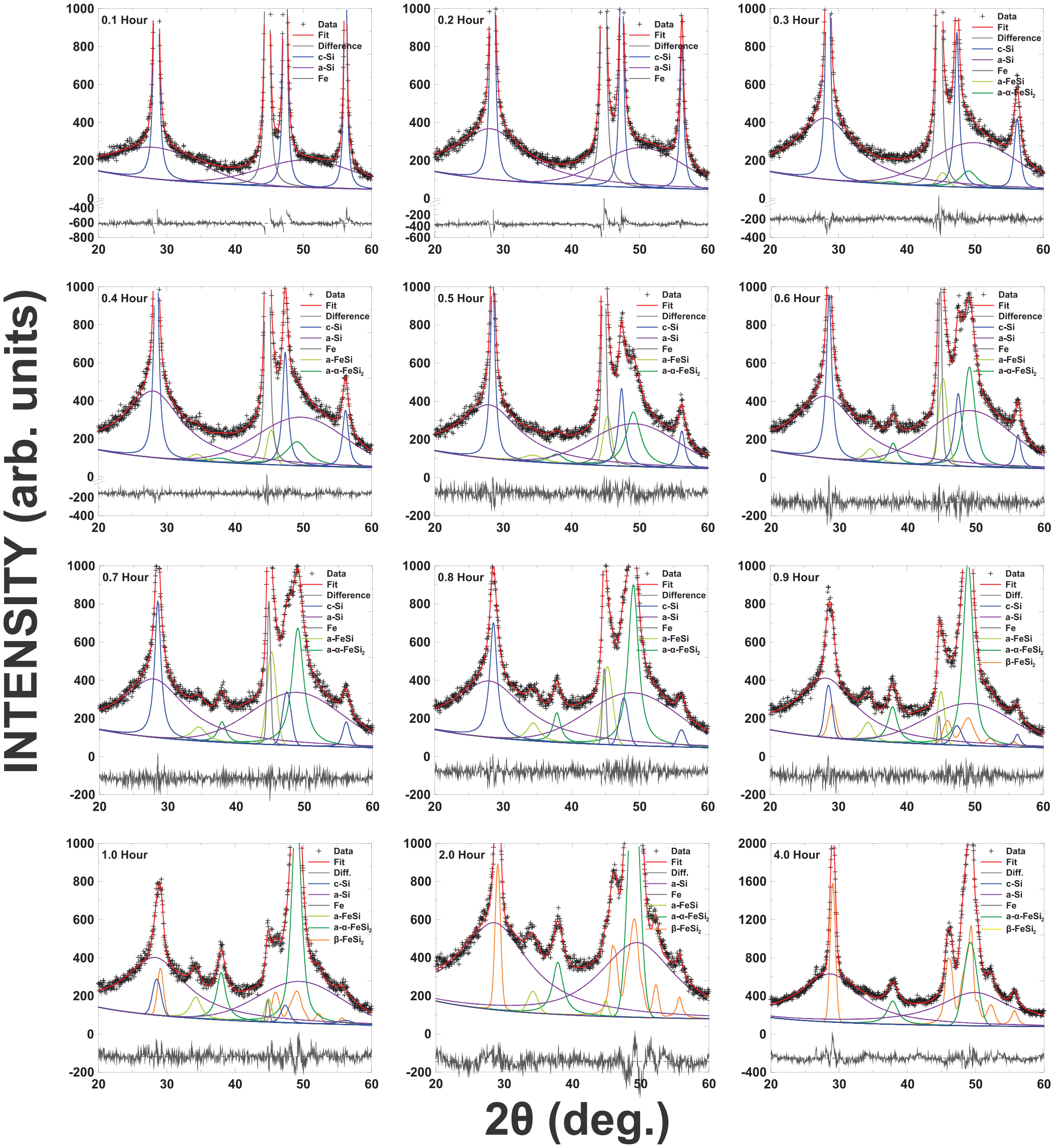

Figure 3.6 Detailed fit of XRD patterns from $Si_{85}Fe_{15}$ series where milling time was varied from 0.1-4 hours.

Following 0.3 hours of milling, two sets of two peaks are observed corresponding to two phases which will be designated, a-α-$FeSi_2$ (peak locations 49.3º and 37.8º) and a-

FeSi (peak locations 45.4º and 34.4º). These peaks increase in intensity as milling time is increased until 0.8 hours when they are most intense. Figure 3.7 shows the peaks that were used to fit the a-α-$FeSi_2$ and a-FeSi phases. Vertical lines have been added representing the reference patterns of each phase's crystalline counterpart. There is a partial match of the fitted peaks to the reference patterns, though several peaks are not observed in the experimental diffraction pattern. In order to further understand the phases formed in the initial stages of the mechanochemical reaction, a Debye scattering calculation was performed using the set of atoms forming the α-$FeSi_2$ and FeSi unit cells. The calculated scattering profiles are shown in Figure 3.8.

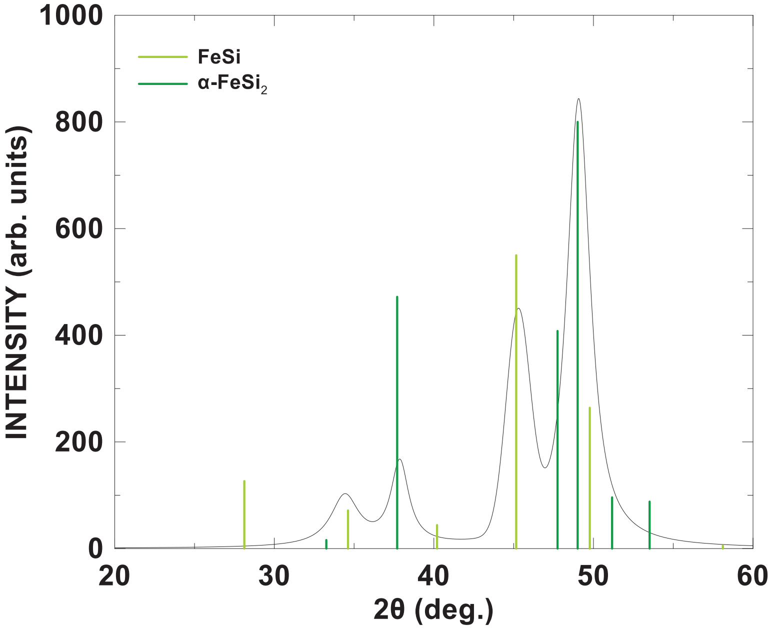

Figure 3.7 Curves used to fit the unknown phases denoted a-α-$FeSi_2$ and a-FeSi for the $Si_{85}Fe_{15}$ alloy milled for 0.8 hours with vertical lines indicating the reference patterns.

The scattering profile calculated for a-α-$FeSi_2$ shows two peaks, one at 48.6° and the other at 37.0°. These peaks resemble the two peaks attributed to the a-α-$FeSi_2$ in the fit; however, the experimentally observed peaks are considerably sharper than those calculated by the Debye scattering formalism. Additionally, the scattering profile calculated for a-

FeSi does not resemble the set of peaks that were observed experimentally. The Debye scattering model fails to explain the experimentally observed diffraction patterns in the initial stages of mechanochemical reaction. The most likely explanation for the origin of the unknown phases in Figure 3.7 is that these phases formed may have a similar crystal structure to α-$FeSi_2$ and FeSi resulting in a similar diffraction pattern; however, substantial disorder, defects, stacking faults, and/or strain have caused the experimentally observed diffraction pattern to differ significantly from the reference diffraction pattern. Additionally, it is also possible that crystal structures formed when only a small number of atoms are present may vary from the expected crystal structure.

Following 0.9 hours of milling β-$FeSi_2$ is first observed and increases in intensity as milling time is further increased, while the a-α-$FeSi_2$ and a-FeSi phases decrease in intensity. The a-FeSi phase disappears entirely following 4 hours of milling, and the only remaining phases are a-Si, a-α-$FeSi_2$, and β-$FeSi_2$. This is in partial agreement with the mechanism that has been previously proposed for the mechanochemical reaction of high Fe content Si-Fe alloys.[97]

It was reported Yelsukov and Dorofeev that in the initial stages of milling the mechanochemical reaction occurs at disordered grain boundaries, relying on a decrease in Fe grain size, allowing the solid-state diffusion of Si into Fe, to form an amorphous Si-Fe alloy. As grain size is reduced, disordered grain boundaries increase, accounting for ~15% of the molar volume when grain size is < 10 nm where amorphous Si-Fe alloys are formed.[97–99] The work done by Yelsukov and Dorofeev explored two Fe-rich compositions $Si_{25}Fe_{75}$ and $Si_{32}Fe_{68}$, where the only phase detected following the mechanochemical reaction is FeSi. As a result of a more Si rich starting composition ($Si_{85}Fe_{15}$) in this work, a-FeSi as well as a-α-$FeSi_2$ are initially observed.

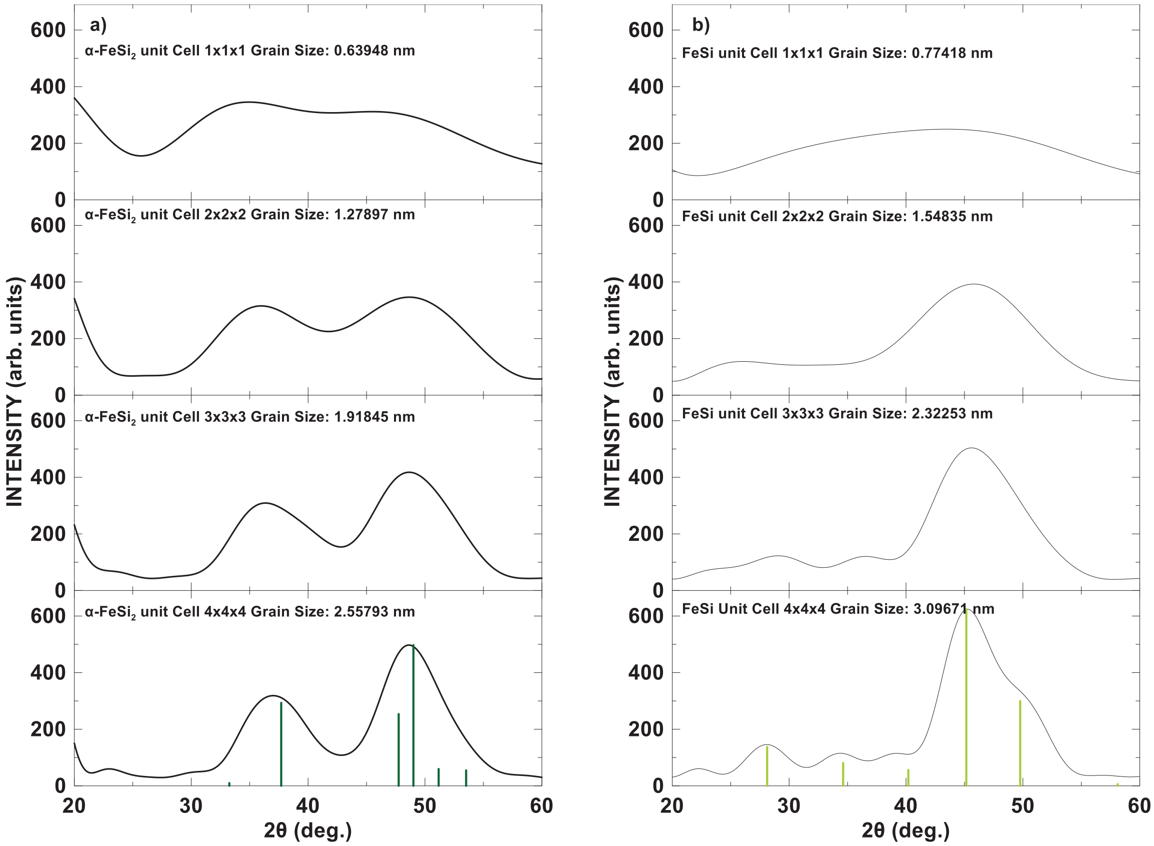

Figure 3.8 Debye scattering calculation for a) α-$FeSi_2$ and b) FeSi with vertical lines representing the reference diffraction pattern for the crystalline species.

Phase formation in the initial stages of the mechanochemical reaction prefers the formation of a-α-$FeSi_2$ and a-FeSi though they are not the thermodynamically preferred phases. With such a large crystal structure, the formation of β-$FeSi_2$ requires the rearrangement of atoms and must be limited by a kinetic barrier. β-$FeSi_2$ is therefore only observed at milling times > 0.8 hours. After 4 hours, when a steady state is reached, β-$FeSi_2$ is the dominant phase. A summary of the relative integrated intensities of all fitted phases is shown in Figure 3.9 as a function of milling time. Following 4 hours there remains a-Si, β-$FeSi_2$ and α-$FeSi_2$, and no FeSi nor c-Si peaks are detected.

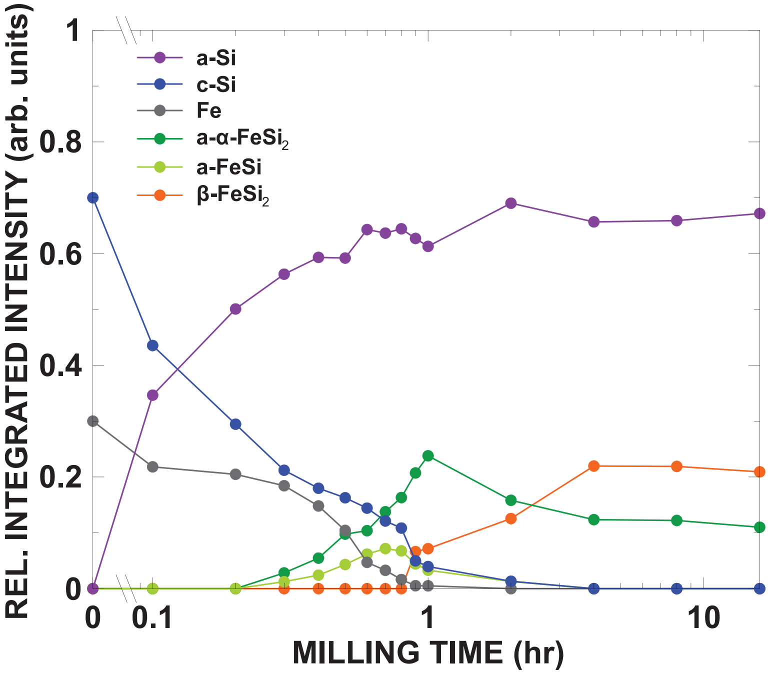

Figure 3.9 Relative integrated intensity of phases determined by fitting XRD patterns for $Si_{85}Fe_{15}$ alloys generated as a function of milling time.

In order to further characterize the microstructure of the $Si_{85}Fe_{15}$ alloy series ^{57}Fe Mössbauer spectroscopy was conducted. Figure 3.10 a) shows Mössbauer spectra collected at a velocity range from -2 to +2 mm/s and their associated fits. A velocity range of -2 to +2 mm/s was selected in order to focus on the FeSi and $FeSi_2$ phases which should appear as quadrupole split doublets clearly visible within this range near 0 mm/s.[88,100–102] By focusing on this region, the intent is to gain insight on phase formation during the initial stages of the mechanochemical reaction.

Initially both α-Fe and Si-Fe phases are detected following 0.1 hours of milling. The central two peaks of the α-Fe sextet are detected at ±0.8 mm/s and, as milling time is increased, decrease in intensity. The Si-Fe phase is detected as a quadrupole split doublet with peaks at -0.1 mm/s and 0.5 mm/s, though the exact positions vary as a function of milling time. As milling time is increased the Si-Fe phases increase in intensity and the center shift decreases, as shown in Figure 3.10 b). In contrast to the XRD analysis, Si-Fe phases are detected by Mössbauer spectroscopy immediately after 0.1 hours of milling, whereas Si-Fe phases were detected only after 0.3 hours by XRD. This reflects the dependence of XRD detection limits on grain size, whereas Mössbauer detection limits are insensitive to grain size.

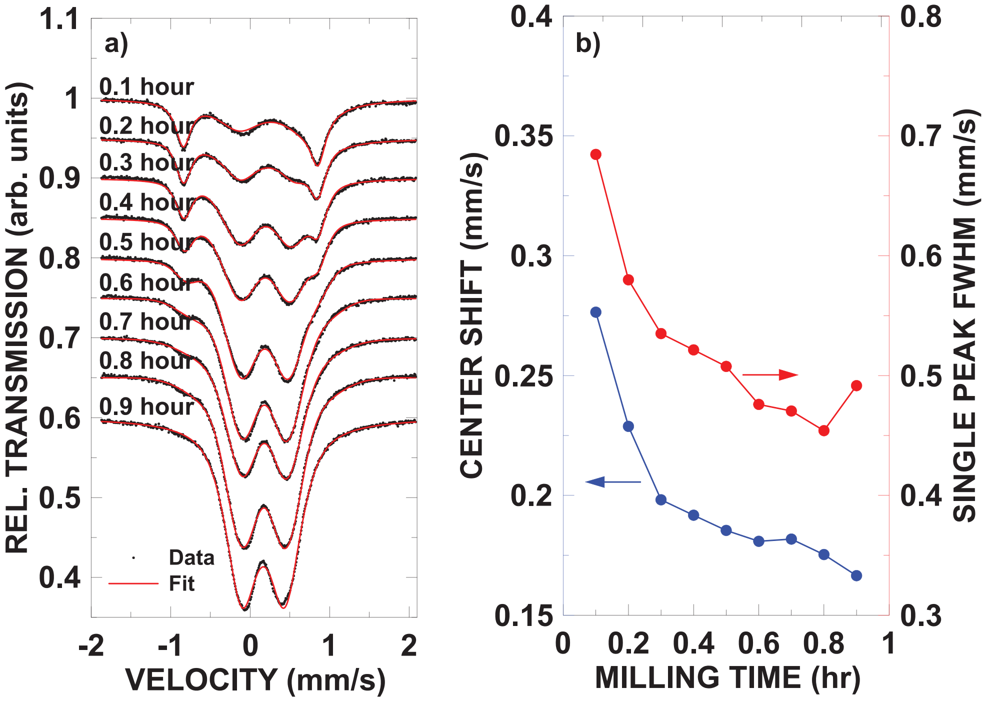

Figure 3.10 a) Mössbauer spectra and fit of $Si_{85}Fe_{15}$ from 0.1-0.9 hours of milling and b) the fitted centre shift and quadrupole splitting.

Since multiple Si-Fe phases are present in all samples, it is necessary to determine the hyperfine parameters of individual Si-Fe phases in order to interpret the Mössbauer spectra. α and β-$FeSi_2$ were synthesized by ball milling and arc-melting and the XRD patterns of the resulting phases are shown in Figure 3.11. Following the trend shown in Figure 3.4 c), when Si and Fe powders are ball milled at a stoichiometric ratio such that the final alloy composition is $FeSi_2$, β-$FeSi_2$ is the only phase formed. This is confirmed by the diffraction pattern shown in Figure 3.11 a). However, when Si and Fe are arc melted at a stoichiometric ratio such that the final composition of the alloy is $FeSi_2$, α-$FeSi_2$ is formed with an FeSi impurity. α-$FeSi_2$ is the metastable polymorph of $FeSi_2$ stable above 915 ºC. Since the arc-melted alloy is rapidly quenched, only α-$FeSi_2$ is able to form with the addition of an FeSi impurity. This impurity exists as $FeSi_2$ is not congruently melting. The arc melted alloy was then ball milled for 4 hours in order to observe the effects of ball milling on the hyperfine parameters of α-$FeSi_2$ observed by Mössbauer spectroscopy.

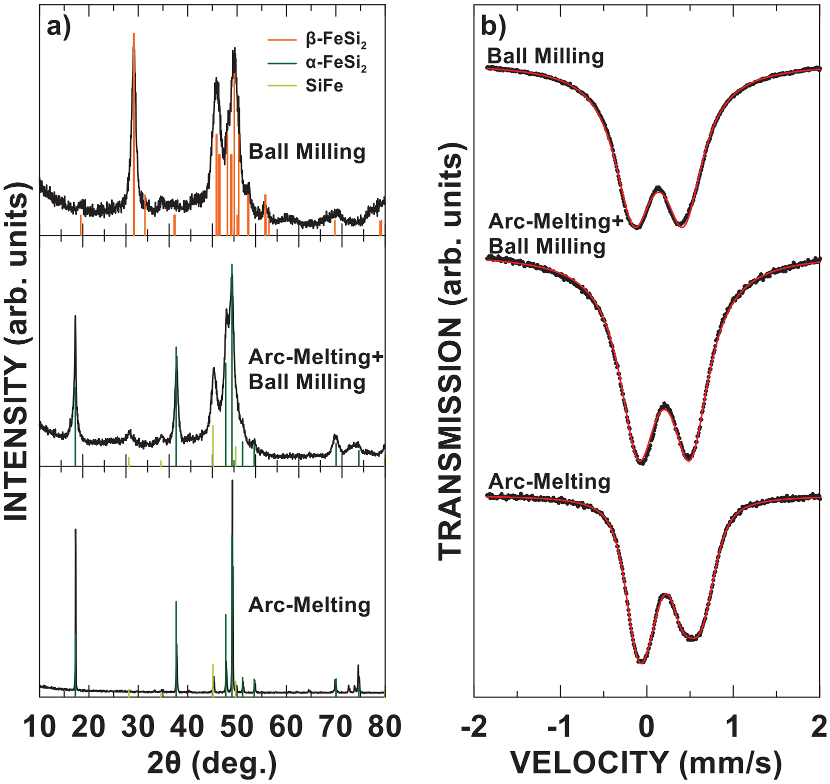

Figure 3.11 a) XRD and b) Mössbauer spectroscopy analysis of $FeSi_2$ alloys made by ball milling, arc-melting, and ball milled following an arc-melt.

By fitting the Mössbauer spectra shown in Figure 3.11 b), the centre shift of arc melted α-$FeSi_2$ was found to be 0.239 mm/s. When the same alloy was ball milled the centre shift was found to decrease to 0.201 mm/s. The center shift of ball milled β-$FeSi_2$ was found to be 0.139 mm/s. It should also be noted, that given the presence of FeSi in the arc melted α-$FeSi_2$ alloy, there should be an increase in center shift.[88] Comparing the results observed here to previous reports of hyperfine parameters for Si-Fe phases, the effect of ball milling appears to increase the center shift of β-$FeSi_2$ and decrease the center shift of α-$FeSi_2$. The center shift of β-$FeSi_2$ was reported to be less than 0.100 mm/s.[100,101] Center shift values of α-$FeSi_2$ were reported to be 0.260 mm/s when evaluating crystalline α-$FeSi_2$ or thin films.[101,102] Center shift values for FeSi were found to be 0.280 mm/s.[101] As the center shift values of both α and β-$FeSi_2$ become increasingly similar following ball milling, Mössbauer spectroscopy is unable to resolve two doublets with a difference in center shift of > 0.1 mm/s and a single peak FWHM of 0.5 mm/s. However, the trends in center shift can be correlated to average composition as a function of milling time.

The initially detected Si-Fe phase has a center shift of 0.276 mm/s and a single peak FWHM of 0.685 mm/s. As milling time is increased there is a substantial decrease in center shift to 0.228 mm/s and 0.198 mm/s as well as single peak FWHM to 0.580 mm/s and 0.535 mm/s for 0.2 and 0.3 hours of milling time respectively. The comparatively high center shift and single peak FWHM values observed in the first 0.1 hours of milling can be explained by the previously reported reaction mechanism for Fe rich Si-Fe alloys reported by Yelsokov and Dorofeev. As grains are reduced alloying is initially observed in highly disordered grain boundaries relying on the solid-state diffusion of Si into Fe; therefore resulting in an Fe rich Si-Fe alloy.[97] As Fe content is increased in Si-Fe alloys, an increase in center shift should be observed.[88] Additionally, the ~20% increase in single peak FWHM can be explained by disorder. In a Mössbauer spectrum FWHM is related to the mean lifetime of the nuclear excited where an increase in the mean lifetime of the nuclear excited state decreases FWHM and a decrease in the mean lifetime of the nuclear excited state increases FWHM.[85] In a highly disordered alloy, however, there is a larger variation in observed center shift therefore resulting in an increase in the observed FWHM,[97] since mean lifetime of the nuclear excited state is an intrinsic property of the nucleus and should not vary considerably. These results, therefore, confirm the presence of a highly disordered, Fe rich, Si-Fe alloy forming at small grain boundaries, such that it cannot be detected by XRD. A continual decrease in center shift and FWHM can be explained by an increase in Si content of the Si-Fe alloy, and an increase in order of the Si-Fe alloy respectively, decreases in both parameters are observed until 0.9 hours of milling when the β-$FeSi_2$ phase is first observed by XRD. The presence of β-$FeSi_2$ should have two effects, a decrease in center shift and an increase in FWHM as observed in Figure 3.10 b). Because β-$FeSi_2$ has a lower center shift than α-$FeSi_2$ and FeSi the appearance of β-$FeSi_2$ will decrease the observed center shift, however, given all phases are present, the superimposing spectra cause an increase in the observed FWHM.

Mössbauer spectra were additionally collected from a velocity range of -12 to +12 mm/s such that the full spectrum of α-Fe is observed, as shown in Figure 3.12 a). Using the method for quantitative composition determination by Mössbauer spectroscopy which is the topic of, and will be heavily discussed in, Chapter 4, the recoil free fraction of each species (Fe and $FeSi_2$) was determined. This allows the calibration of integrated intensity to atomic fraction from one species to another as a function of milling time.

Figure 3.12 b) shows the quantitative composition determination by Mössbauer spectroscopy for all $Si_{85}Fe_{15}$ alloys. After 0.1 hours of milling the mechanochemical reaction proceeds and Si-Fe phases are detected. Because this phase is not immediately detected by XRD, this implies that $FeSi_2$ has formed with no long-range order. After 0.3 hours of milling, Si-Fe phases have accumulated enough long-range order to be detected by XRD, and both XRD and Mössbauer spectroscopy are in agreement. XRD and

Mössbauer spectroscopy both show that all Fe eventually reacts with Si to form Si-Fe phases, however, XRD is able to show that changes in α and β $FeSi_2$ continue to occur following 2 hours of milling while Mössbauer spectroscopy only shows a steady state following 2 hours where Fe is no longer detected.

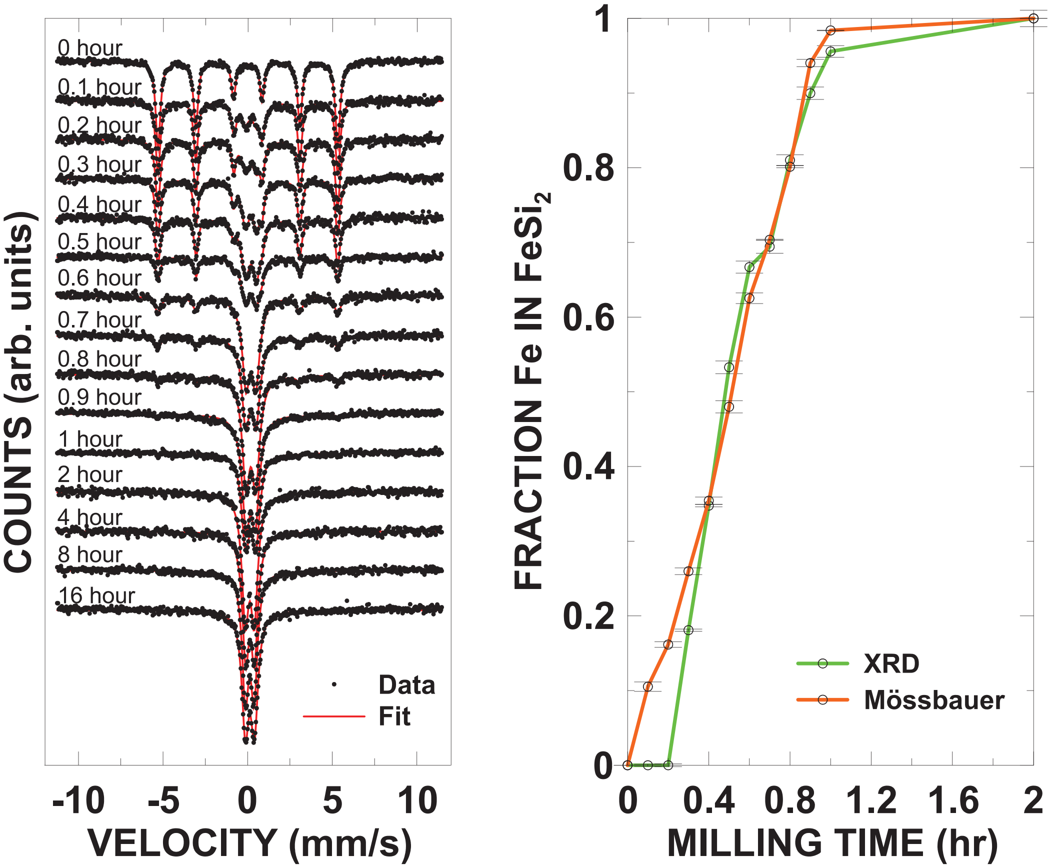

Figure 3.12 a) Mössbauer spectra collected for $Si_{85}Fe_{15}$ alloys, and b) fraction of total Fe content incorporated in Si-Fe including data from XRD as a function of milling time.

To summarize the XRD and Mössbauer results, when Fe and Si are ball milled in a 15:85 mole ratio they immediately react to form a disordered Fe rich Si-Fe alloy as grain boundaries are reduced and Si and Fe contact is increased allowing solid state diffusion. This alloy is immediately observed by Mössbauer spectroscopy with a center shift of 0.276 mm/s, indicating an Fe rich phase. Following 0.3 hours of milling this phase is observed by XRD, though the peaks representing these phases do not match the reference diffraction pattern of known Si-Fe phases, and instead only partially match that of FeSi and α-$FeSi_2$, additionally indicating a disordered Si-Fe phase. As milling time is further increased center shifts decrease indicating the formation of β-$FeSi_2$ rather than α-$FeSi_2$ or FeSi. This is additionally confirmed by XRD as β-$FeSi_2$ appears following 0.8 hours of milling. Following the completion of the mechanochemical reaction β-$FeSi_2$ is the predominant phase as observed by XRD, with α-$FeSi_2$ at roughly half the intensity of β-$FeSi_2$. The reaction proceeds via a zeroth order reaction mechanism as the concentration of detected Si-Fe phases varies linearly as a function of milling time shown both by XRD and quantitative composition determination by Mössbauer spectroscopy.

3.1.2.2 Electrochemical Characterization

Electrodes were prepared for each sample and electrochemical performance was evaluated in coin cells. Results are shown in Figure 3.13. The potential profiles in the top row of panels show the characteristic sloping profile of Si. In the case of $Si_{90}Fe_{10}$, there is a plateau at 450 mV, corresponding to the de-lithiation of $Li_{15}Si_4$. This means that $Li_{15}Si_4$ crystallizes when $Si_{90}Fe_{10}$ is fully lithiated. This is immediately apparent in the differential capacity curve in the middle row panels of Figure 3.12, where a large peak is formed in the initial cycles, and increases in intensity with cycle number. Little to no $Li_{15}Si_4$ formation is observed for $Si_{85}Fe_{15}$, nor any compositions with decreasing Fe content. The bottom panel of Figure 3.12 shows the cycling performance of this series of alloys. As Fe content is increased, capacity decreases and cycling performance improves. $Si_{85}Fe_{15}$ cycled at a reversible capacity of 1742 Ah/L with an initial coulombic efficiency of 80.7% and an average coulombic efficiency for the following cycles of 99.43% ± 0.06%. Because

$Si_{85}Fe_{15}$ was the highest Si composition that did not form $Li_{15}Si_4$ during cycling, this composition was selected for a kinetic study of the mechanochemical alloying process.

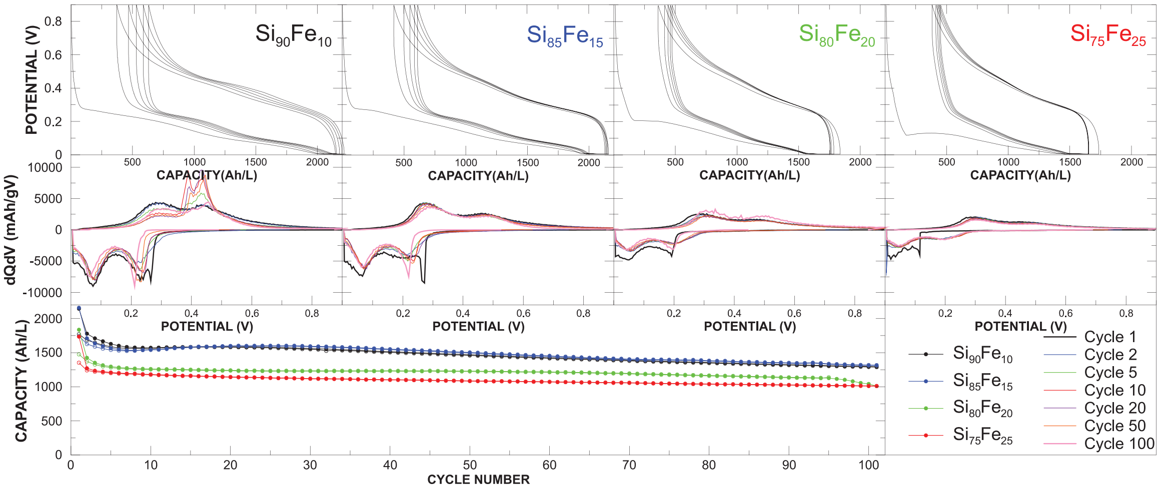

Figure 3.13 Electrochemical performance data for $Si_{100-x}Fe_x$ (x=10, 15, 20, 25). Top panel: voltage curve (first 5 cycles). Middle panel: differential capacity. Bottom panel: capacity versus cycle number.

Figure 3.14 shows the electrochemical performance of electrodes prepared from $Si_{85}Fe_{15}$ alloys having been milled for 2,4, 8, and 16 hours. After 2 hours of milling c-Si was no longer detected in the diffraction pattern, the diffraction pattern and Mössbauer spectrum indicated all Fe had reacted to form $FeSi_2$. However, the differential capacity profile of the 2-hour sample shows that as cycle number increases $Li_{15}Si_4$ phase is detected. Additionally, following 4 hours of milling, $Li_{15}Si_4$ is detected, though not in the initial cycles. $Li_{15}Si_4$ content increases as a function of cycle number. However, after 8 and 16 hours, no $Li_{15}Si_4$ is detected at any cycle number. In order to prevent the formation of $Li_{15}Si_4$ during electrochemical cycling further milling is required, even after the mechanochemical reaction has completed, likely in order to reduce the size of active Si domains.

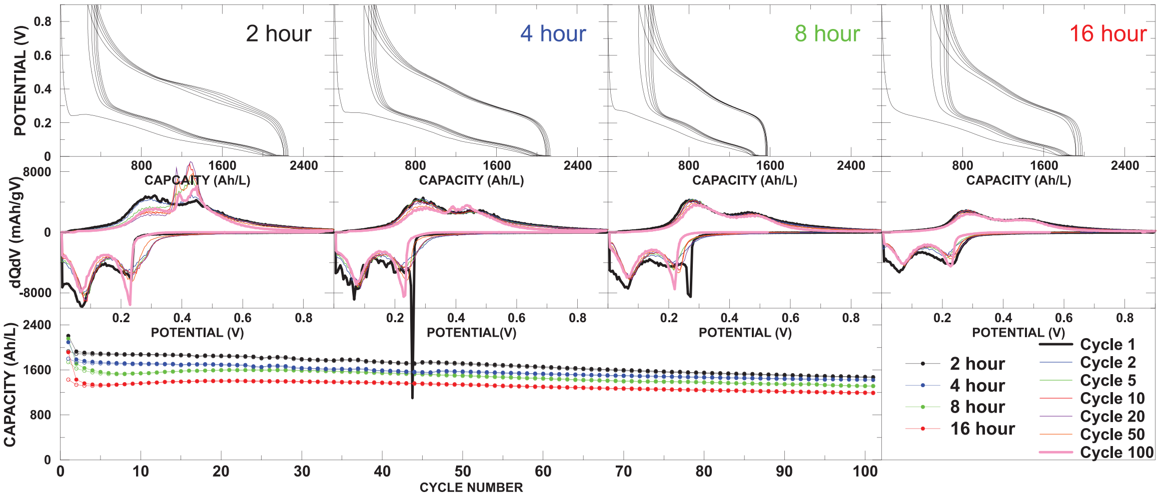

Figure 3.14 Electrochemical performance data for $Si_{85}Fe_{15}$ where milling time=2, 4, 8, 16 hours. Top row panels: voltage curve (first 5 cycles). Middle row panels: differential capacity. Bottom panel: capacity versus cycle number.

The percent of the active Si present that forms $Li_{15}Si_4$ at full lithiation can be quantified from the fraction of the $Li_{15}Si_4$ de-lithiation peak compared to the total de-lithiation capacity. The de-lithiation of $Li_{15}Si_4$ occurs at a potential between 360 to 480 mV, while the de-lithiation of pure a-Li_xSi occurs in a solid solution region and results in a sloping potential profile. with capacity observed in the entire 5 mV - 900 mV potential range. About 20 % of the de-lithiation capacity of a-Li_xSi occurs in the 360 to 480 mV range that $Li_{15}Si_4$ de-lithiation occurs. From these properties, the content of active Si that forms $Li_{15}Si_4$ during lithiation can then be approximated according to Equation 3.2.[75]

$$\%Li_{15}Si_4 = \frac{\left[\frac{Q_{0.36\,V-0.48\,V}}{Q_{tot}}-0.2\right]}{0.8} * 100\% \tag{3.2}$$

Where $\%Li_{15}Si_4$ is the percent active Si in the alloy that forms $Li_{15}Si_4$, $Q_{0.36\,V-0.48\,V}$ is the de-lithiation capacity observed within the potential range of 360 mV to 480 mV, and Q_{tot} is the de-lithiation capacity observed over the entire potential range from 5 mV to 900 mV

Though the peaks in the differential capacity profile of the 2-hour and especially the 4-hour milled alloys appear small, as shown in Figure 3.15, by using equation 3.2 the quantity of active Si present that forms $Li_{15}Si_4$ is significant. When milled for 2 hours the quantity of active Si present that forms $Li_{15}Si_4$ content is in excess of 20%, though in the initial cycle there was little to no $Li_{15}Si_4$ detected. Similarly, for the 4-hour milled alloy, no $Li_{15}Si_4$ is observed in the initial cycle, though as cycle number increases the quantity of active Si present that forms $Li_{15}Si_4$ content increases reaching nearly 10% following 10 cycles. When milling time is in excess of 8 hours, the quantity of active Si present that forms $Li_{15}Si_4$ content is ~0% at any cycle number. Such alloys are expected to have the most stable cycling.

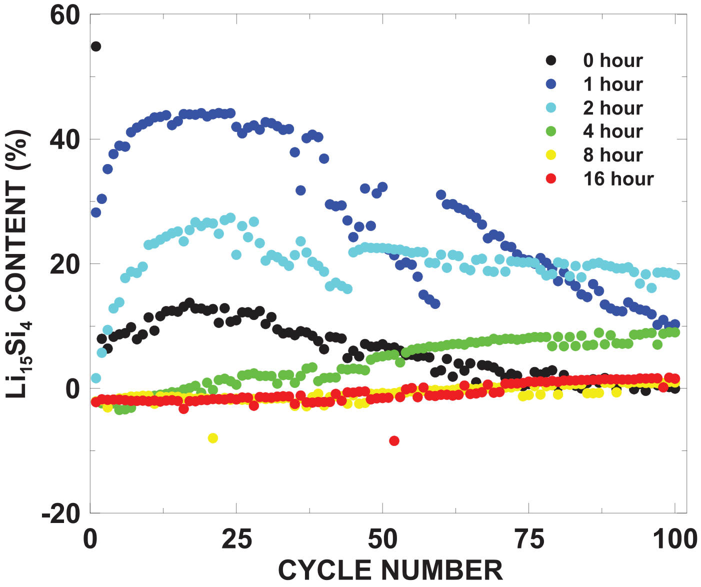

Figure 3.15 $Li_{15}Si_4$ content for all $Si_{85}Fe_{15}$ alloys.

The CEs of $Si_{85}Fe_{15}$ alloys prepared with different milling times are shown in Figure 3.16 a) as a function of cycle number. Average CE's improve with milling time; though, initial CE decreases as a function of milling time. The lowest initial CE is observed for the 0 hours milling sample; this is the result of mechanical disconnection of particles. Lithium-ions are irreversibly trapped in particles that are disconnected, resulting in a very low initial CE. At milling times of 1, 2 and 4 hours, initial CE improves as Si reacts with

Fe and grain sizes are reduced, decreasing the number of mechanically disconnected particles upon electrochemical lithiation. Following 8 and 16 hours of milling, initial CE decreases drastically. Further processing following the completion of the mechanochemical reaction results in the refinement of particles potentially increasing surface area therefore decreasing initial CE as more electrolyte decomposition is required to form a passivation layer over the surface of the particles. The initial CE following 16 hours of milling was 74.6%. When comparing average CE, alloys milled for 4, 8 and 16 hours appear to have the highest average CE that is, in the case of the 16 hour alloy, 99.40% ± 0.07%, with 1 and 2 hours of milling having slightly lower average CE's.

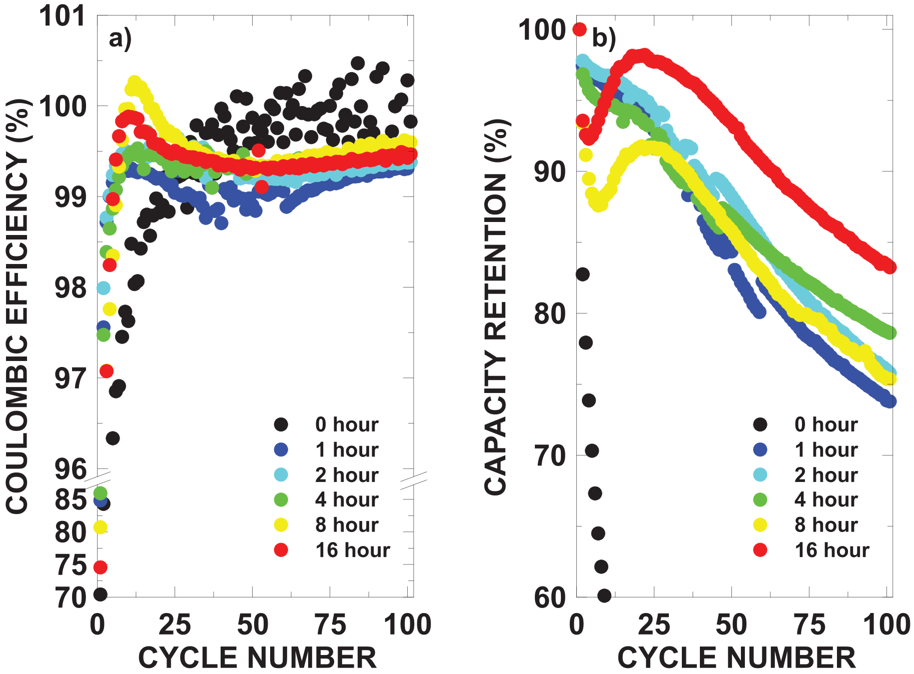

Figure 3.16 CE and normalized capacity as a function of cycle number for $Si_{85}Fe_{15}$ alloys.

Figure 3.16 b) shows normalized capacity as a function of cycle number. Capacity is normalized relative to the initial charging capacity. Capacity retention improves as milling time increases with a slight discrepancy comparing 4 and 8 hours; though following 16 hours of milling capacity retention is the highest with >80% retained capacity following

100 charge discharge cycles. This is a considerable improvement in capacity retention when compared to other Si-Fe alloys reported. Li et. al showed that an Si-Fe alloy of the same composition ($Si_{85}Fe_{15}$) when blended with graphite at a weight ratio of 60:40 $Si_{85}Fe_{15}$:graphite had a capacity retention of 76% following 50 cycles.[46] Lee et. al showed that an $Si_{80}Fe_{20}$ alloy had a capacity retention of 22% following 50 cycles, and 59% following 50 cycles when blended with graphite at a weight ratio of 50:50 $Si_{80}Fe_{20}$:graphite.[90] Additionally, Dong et. al showed that a ball milled $Si_{50.1}Fe_{28.4}Ba_{20.5}$ alloy had a capacity retention of 38% following 15 cycles, and 85% capacity retention following 15 cycles when blended with graphite at a weight ratio of 50:50 $Si_{50.1}Fe_{28.4}Ba_{20.5}$:graphite.[91] In all of these publications fluoropolymer binders were used resulting in poor capacity retention. Fluoropolymer binders do not fully coat the surface of electrode particles, do not chemically bond to the surface of electrode particles, and swell when exposed to electrolyte compromising the mechanical integrity of the binder.[36,39,40] In this work, Li-PAA was used as a binder. Water based poly-carboxylic acid binders offer dramatic improvements in alloying negative electrode cycling by totally covering the surface of the particles, chemically bonding with the surface of the particle, and maintaining mechanical integrity when exposed to electrolyte.[36,40–42] By using Li-PAA as a binder a capacity retention of 83.2% was observed following 100 cycles for a $Si_{85}Fe_{15}$ alloy milled for 16 hours without the use of graphite. This result highlights the importance of water-based poly-carboxylic acid binders. Drastic improvements in capacity retention are observed when appropriate binders are used.

As a direct comparison of structural characterization and electrochemical analysis, a model of active Si content can be used to calculate theoretical capacity and then compared to observed capacity. This is shown in Figure 3.17. There is a large difference in observed first lithiation and de-lithiation capacity, as the first lithiation capacity includes SEI formation and is then larger than the theoretical value. During de-lithiation, mechanical disconnection of active materials tends to lower the capacity less than the theoretical value. As a result, it is expected that the theoretical capacity as predicted by structural characterization should reside between the observed first lithiation and de-lithiation capacities. In order to calculate a theoretical capacity using XRD, the relative quantity of the Si phase was used, where a decrease in relative Si content can be directly related to the formation of Si-Fe phases and a therefore a proportional decrease in capacity. In order to calculate theoretical capacity from the Mössbauer spectroscopy, the change in relative peak areas from Fe to $FeSi_2$ was considered. As Fe reacts with active Si to form $FeSi_2$, capacity should decrease accordingly. Both of these models have clear limitations that will be discussed below.

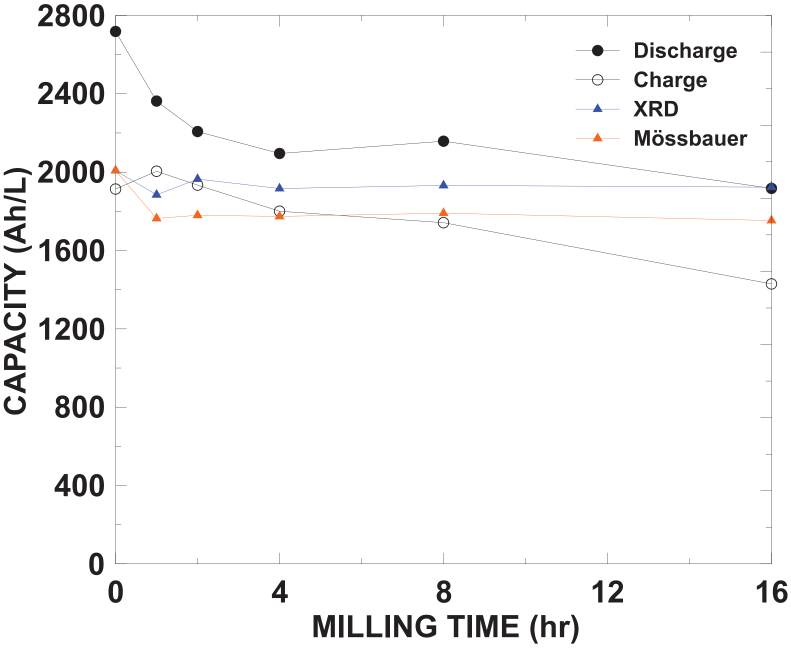

Figure 3.17 Experimental and theoretical specific capacity for $Si_{85}Fe_{15}$ electrodes as a function of milling time.

In both the case of XRD and Mössbauer spectroscopy, the un-milled 85Si + 15Fe powder mixture serves as a verification of capacity prediction. Since no mechanochemical reaction has occurred and the amount of active Si is known exactly, the theoretical capacity should then match the observed capacity. As expected, the capacity of this sample resides between the experimentally observed lithiation and de-lithiation capacities. When considering theoretical capacity as calculated by XRD, there is an underestimation of capacity of the sample milled for 1 hour. This indicates that the relative quantity of Si in the diffraction pattern was underestimated by the fitting routine. At this milling time there remains a large relative quantity of the unidentified a-FeSi and a-α-$FeSi_2$ phases included in the fit. This may indicate that the amount of Si in these phases may be less than the assumed stoichiometry. Another possibility is that these unknown phases may have some electrochemical activity and are contributing to capacity. As milling time is increased, and the intensity of these phases is decreased the capacity predicted by the model falls within the lithiation and de-lithiation capacities.

However, the theoretical capacity as predicted by Mössbauer spectroscopy is lower than the XRD predicted capacity for all the samples, excepting the un-milled powder. This results in a larger discrepancy between the observed and predicted capacities. The reason for the lower predicted values is because Mössbauer spectroscopy cannot differentiate between FeSi and $FeSi_2$ phases and only the formation of $FeSi_2$ was assumed when predicting theoretical capacity. As a consequence, the theoretical capacity is underestimated when FeSi is present, at all milling times < 2 hours. This model is most accurate when no FeSi is present following 4 hours of milling and the theoretical capacity is within error of the observed capacity. However, even when no FeSi is present, values predicted by Mössbauer spectroscopy are lower than those predicted by XRD. This is likely the result of a systematic error when considering a-Si in the XRD pattern. Such broad peaks make the disambiguation of a-Si and background intensity difficult. If more background intensity is considered as a-Si, the model will then predict more capacity. As a result, the capacity predicted by XRD is systematically larger than that predicted by Mössbauer spectroscopy. It is then expected that when FeSi is present, XRD is able to more accurately predict capacity as the systematic error is self correcting; however, when no FeSi is present Mössbauer spectroscopy is able to more accurately predict capacity.

3.2 Cr

Cr is an interesting choice as an inactive transition metal in Si/inactive alloys because of its differing mechanical properties to Fe, especially when mechanochemical synthesis is the method by which the Si/inactive alloys are formed. Cr is a brittle metal,[103] and therefore the kinetics of the mechanochemical alloying of Si with Cr should differ when compared to a more ductile Fe transition metal.

Cr has been previously explored as a component in Si alloys.[104,105] Weydanz et al. found that when $CrSi_2$ was reacted with Li at 360 ºC for 15 hours under argon and galvanostatically de-lithiated, there was an observed de-lithiation capacity of 500-800 mAh/g for varying $CrSi_2$:Li ratios.[104] However, Fleischauer et al. showed, by combinatorial sputtering, that Si-M (M = Cr + Ni, Fe, Mn) exhibit capacities directly related to the active Si content and that the SiM and SiM_2 phases are inactive.

The goal of this work is to synthesize Si-Cr alloys by mechanochemical synthesis while quantifying the mechanochemical reaction in order to compare the observed kinetics to those of mechanochemically synthesised Si-Fe alloys. The Si-Cr alloys will additionally be evaluated as negative electrode materials in a Li metal counter electrode half cell.

3.2.1 Experimental

Experimental techniques in this section largely mirror those in section 3.1.1, though rather than an Fe precursor, Cr precursor (-325 Alfa Aesar, 99.5%) was used to form Si-Cr alloys. The mass required for 0.5 mL of Si_8Cr_{15} alloy was 1.053 g Si and 0.344 g Cr. For additional experimental details, the reader is directed to section 3.1.1.

3.2.2 Results and Discussion

From the binary phase diagram of Cr and Si shown in Figure 3.18, at a composition of $Si_{85}Cr_{15}$, the expected equilibrium phases are Si and $CrSi_2$. It is important to note that, in contrast to the Fe-Si system, there is only a single $CrSi_2$ phase. XRD patterns were used to quantify the phases present by fitting pseudo-Voigt functions corresponding to the crystalline reference patterns of $CrSi_2$ Cr, and c-Si. The a-Si phase, however, was fitted using two pseudo-Voigt functions according to a Debye scattering calculation, as discussed above. The appropriateness of this fit indicates that the Si grain size must be <1 nm and intensity is best represented by a Debye scattering model.

Figure 3.19 a) shows the XRD patterns of all $Si_{85}Cr_{15}$ alloys as a function of milling time. Vertical lines represent the location and intensity of the reflections expected from the crystalline reference patterns of Si, $CrSi_2$ and Cr. Figure 3.19 b) shows an example fit of $Si_{85}Cr_{15}$ having been milled for 2 hours with pseudo-Voigt functions corresponding to the peaks of a-Si, c-Si, $CrSi_2$, and Cr. By modeling the diffraction pattern using these phases a simulated diffraction pattern can be generated that closely matches the experimental diffraction pattern. By doing this a qualitative understanding of phase evolution as a function of milling time can be established. The relative integrated intensity was then used to compare the relative quantity of each phase as a function of milling time shown in Figure 3.19 c) along with an approximation of grain size according to the Scherrer equation.

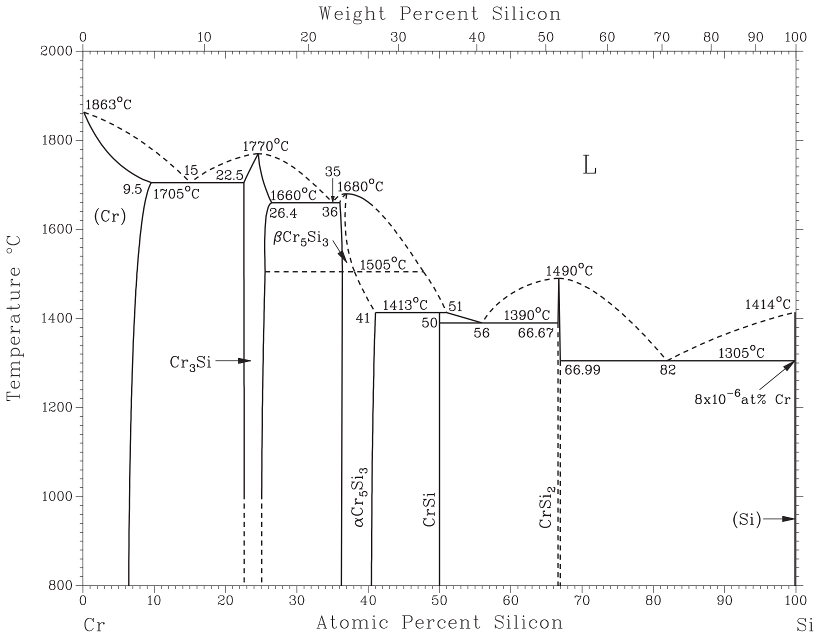

Figure 3.18 Binary phase diagram Cr and Si.

The phase analysis of the $Si_{85}Cr_{15}$ alloy series shows that even after 16 hours of milling the mechanochemical reaction has not completed and some metallic Cr remains unreacted. Additionally, the grain size of metallic Cr does not vary considerably as a function of milling time. During mechanochemical reaction, grain size is reduced by repeated collisions that work harden particles, leading to embrittlement and eventually to fracture. Cr is, however, brittle and the use of Cr may not be appropriate under a milling regime where frequency of impacts is optimized. Though this milling method was optimized for Si,[81] which is also brittle, Young’s modulus of both Si and Cr differ significantly. Young’s modulus of Cr is 279 GPA, while that of Si is ~20% that of Cr at 49 GPA. As a result, significantly more stress is required to strain Cr as compared to Si. In this work milling parameters for the rapid synthesis of amorphous alloys were utilized, whereby impact frequency was optimized rather than impact energy.[81] Given that Cr is brittle low energy high frequency impacts may not exceed the yield strength of Cr, thereby decreasing the rate of the mechanochemical reaction and inhibiting its completion. By increasing impact energy it is possible that a $Si_{85}Cr_{15}$ alloy could be generated with no metallic Cr impurity, however, in this work milling parameters remained constant in order to reasonably compare the mechanochemical reactions of Si with Fe or Cr, and a milling regime optimizing impact energy was not explored.

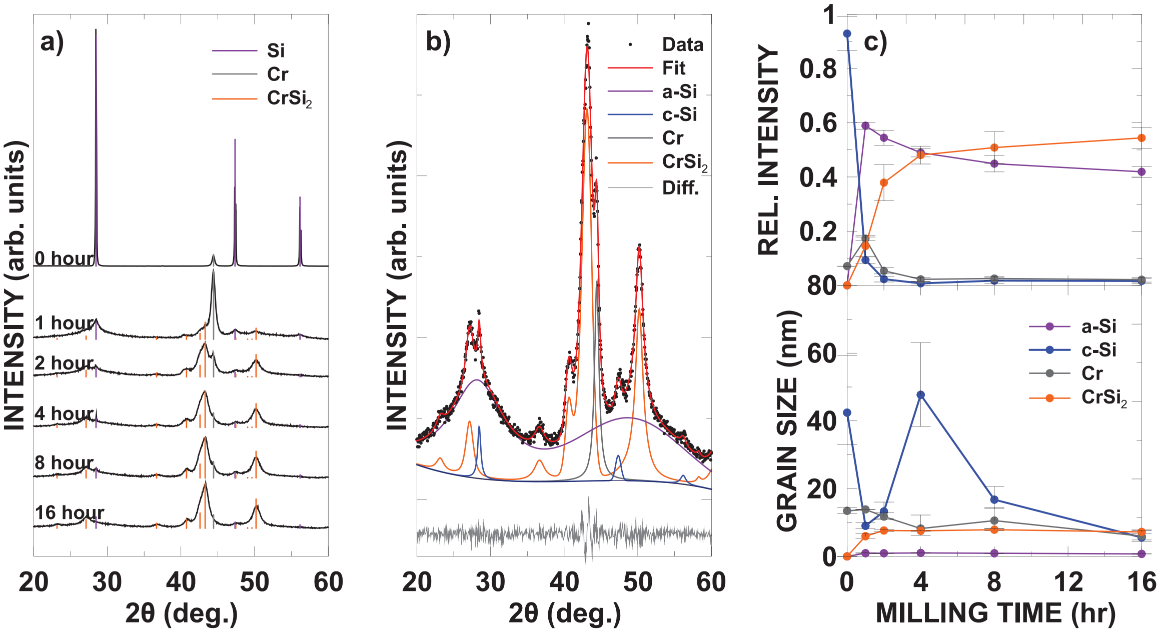

Figure 3.19 a) all XRD patterns of $Si_{85}Cr_{15}$ varying milling time, b) a fit of $Si_{85}Cr_{15}$ milled for 2 hours, and c) a summary of the fitting results for all XRD patterns.

The electrochemical performance of the $Si_{85}Cr_{15}$ alloy series was evaluated in Li-metal half cells, shown in Figure 3.20. The sloping potential profile with two pseudo-plateaus characteristic of a-Si can be observed in the top row of panels in Figure 3.20. The second row of panels shows the differential capacity profile of each milling time from 2 to 16 hours. In all differential capacity plots an increase in potential polarization as a function of cycle number is observed. This can be seen by a uniform shift to the right in the top half of the differential capacity profile, and a shift to the left in the bottom half of the differential capacity profile; indicating that the potential at which Si is lithiated has decreased and the potential at which Si is de-lithiated has increased.

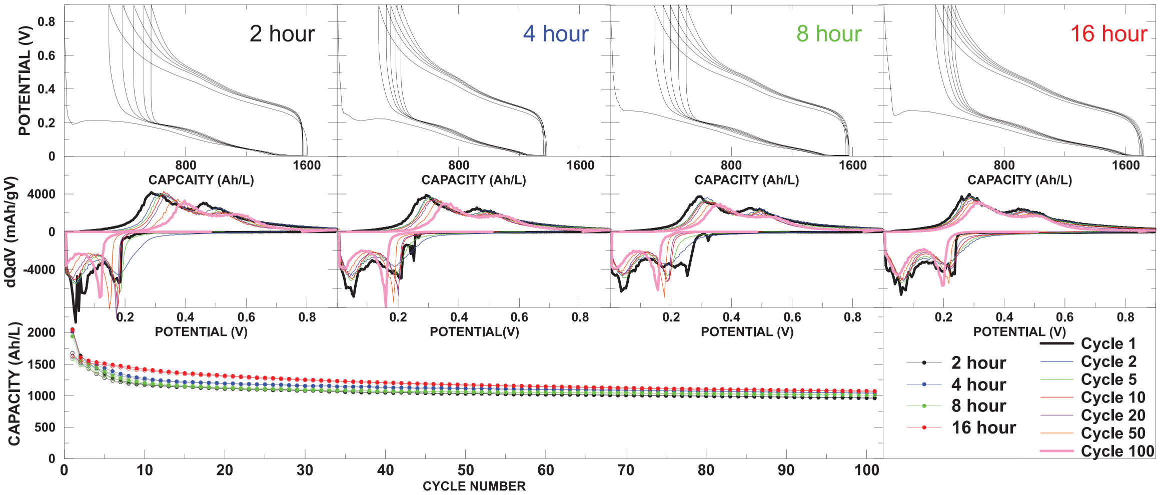

Figure 3.20 Half cell cycling results as a function of cycle number for $Si_{85}Cr_{15}$ as a function of milling time, a) volumetric capacity, b) gravimetric capacity, c) coulombic efficiency.

The average lithiation and de-lithiation potentials were then calculated as a function of cycle number and their difference, representing the potential polarization, was plotted as a function of cycle number, shown in Figure 3.21 a). Potential polarization observed for $Si_{85}Fe_{15}$ alloys as a function of milling times is also shown in Figure 3.21 b) for direct comparison. An increase in polarization as a function of cycle number could be caused by several factors including internal fracture of alloy particles, which can restrict Li ion diffusion paths; the mechanical disconnection of alloy particles, resulting in poor ohmic contacts or the reduction of electrolyte on the surface of the electrode, forming a thicker SEI that is more difficult for ions to penetrate. Increases in potential polarization as a function of milling time are observed for all $Si_{85}Cr_{15}$ alloys, though only observed for un-milled $Si_{85}Fe_{15}$. This implies that either Si-Cr alloys have inferior mechanical properties resulting in the pulverization of alloy particles during lithiation and de-lithiation or metallic Cr or $CrSi_2$ catalyzes the reduction of electrolyte at the electrode surface thereby increasing potential polarization and impedance. In order to support this conclusion a direct-current measurement of area specific impedance (ASI) was additionally performed.

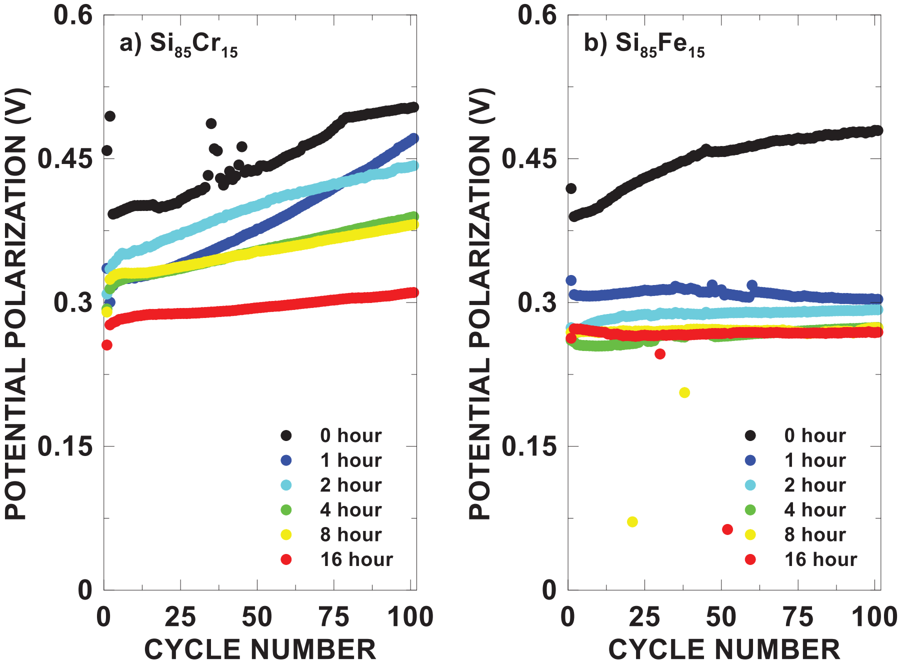

Figure 3.21 Potential polarization as a function of cycle number for $Si_{85}Fe_{15}$ and $Si_{85}Cr_{15}$ alloys evaluated Li-metal half cells.

A 15-minute rest period where the open circuit potential of the cell was allowed to relax was implemented following every charge/discharge cycle. The rest potential change can be correlated to impedance using Ohm's law. Since impedance is proportional to potential over current, the change in impedance divided by the average current of the previous cycle can be used to calculate impedance as a function of cycle number[66] shown in Figure 3.22 a) for $Si_{85}Cr_{15}$ and b) for $Si_{85}Fe_{15}$. Though absolute values of ASI cannot be meaningfully compared, as areal capacity varied from cell to cell; trends in ASI as a function of cycle number can be.

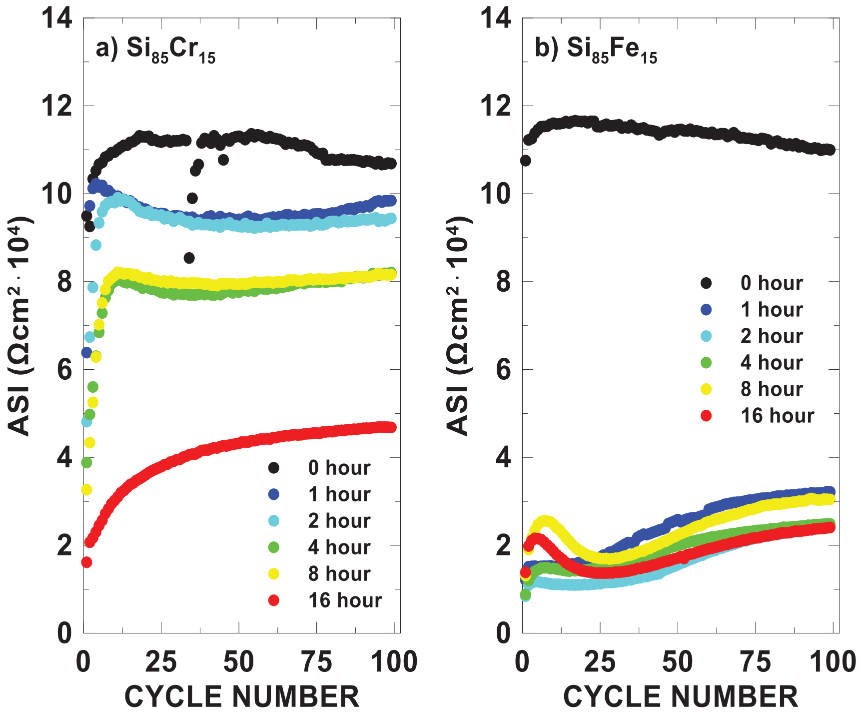

Figure 3.22 Area specific impedance as a function of cycle number for $Si_{85}Cr_{15}$ and $Si_{85}Fe_{15}$ alloys as evaluated in Li-metal half cells.

Drastic increases in impedance as a function of cycle number are observed for all $Si_{85}Cr_{15}$ alloys. Increases in impedance as a function of cycle number are the least extreme following 16 hours of milling. This is the milling time at which the smallest amount of metallic Cr is present according to XRD analysis. However, in the case of $Si_{85}Fe_{15}$ increases in impedance as a function of cycle number are smaller by roughly a factor of two. Additionally, increases in impedance as a function of cycle number do not vary as drastically as a function of milling time for $Si_{85}Fe_{15}$ alloys as they do for $Si_{85}Cr_{15}$ alloys. This behaviour has been previously reported by Yan and Obrovac, who showed that inactive components like Ni and Cu may facilitate parasitic electrolyte reactions, especially at low potentials.[106] Though Cr was not explored in their study, it was found that when Cu or Ni were used the rate of parasitic electrolyte reactions increased by a factor of 2-3.5, additionally showing high concurrent impedance growth. This supports the conclusion that the presence of metallic Cr may be catalyzing the reduction of electrolyte.

CE and normalized capacity are shown in Figure 3.23 a) and b) respectively. Initial irreversible capacities are on average higher than those observed for $Si_{85}Fe_{15}$ alloys having been milled for the same amount of time. This is especially true for $Si_{85}Cr_{15}$ milled for 16 hours where initial CE was 79.7%, as compared to 74.6% for $Si_{85}Fe_{15}$ milled for the same amount of time. This may be, in part, related to the inability of the Cr grain size to be reduced, thereby maintaining lower surface areas and therefore increased initial CE. Average CE, however, was lower for $Si_{85}Cr_{15}$ alloys. When milled for 16 hours the average CE of $Si_{85}Cr_{15}$ was 99.28% ± 0.06%, as compared to 99.40% ± 0.07% observed for $Si_{85}Fe_{15}$ milled for the same amount of time. The most drastic difference in electrochemical performance of $Si_{85}Fe_{15}$ and $Si_{85}Cr_{15}$ can be observed in Figure 3.23 b). Capacity retention as a function of cycle number is considerably worse for all $Si_{85}Cr_{15}$ alloys as compared to $Si_{85}Fe_{15}$ alloys. Following 16 hours of milling the capacity retention of the $Si_{85}Cr_{15}$ alloy was found to be 65.7% after 100 charge discharge cycles, as compared to a capacity retention of 83.2% for a $Si_{85}Fe_{15}$ alloy milled for the same amount of time.

This can be related to the inefficiency of the mechanochemical reaction of Si and Cr. A reversible capacity of 1628 Ah/L was observed for a $Si_{85}Cr_{15}$ alloy milled for 16 hours. This is 200 Ah/L (12%) higher than was observed for $Si_{85}Fe_{15}$ milled for the same amount of time. The mechanochemical reaction of Si with Fe was able to reach completion and observed capacity was therefore lower and capacity retention was improved. Unreacted Si and Cr in the $Si_{85}Cr_{15}$ alloys causes an increase in volume expansion and therefore a decrease in cycling performance. Alloy volume expansion was calculated according to

Equation 3.3 where ξ is volume expansion, k is the molar volume of lithium per host atom, ρ_{alloy} is the density of the alloy, c_{alloy} is the alloy specific capacity, and F is Faraday's constant.[1]

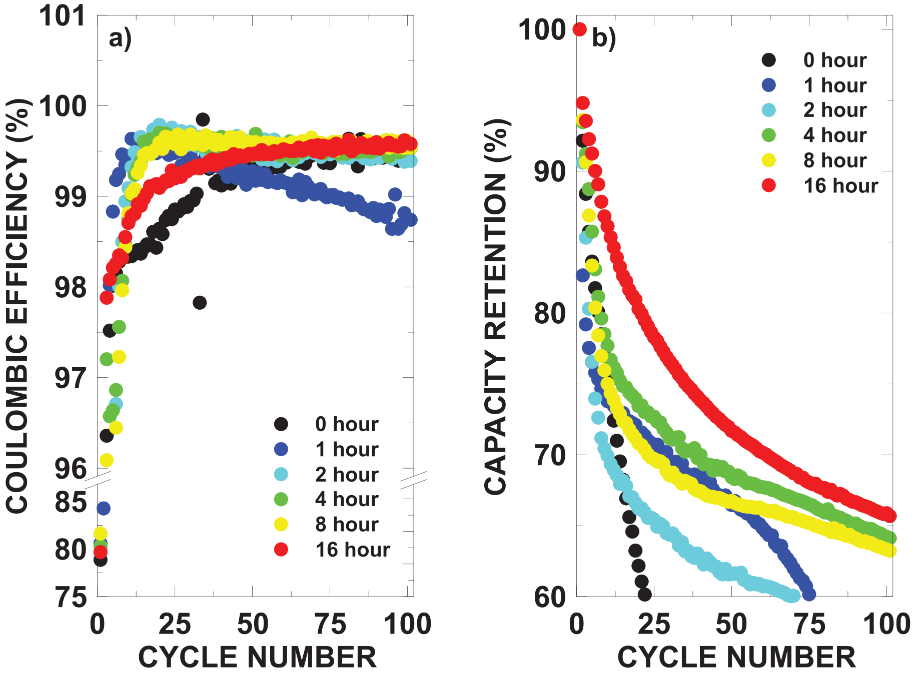

Figure 3.23 a) coulombic efficiency and b) capacity retention as a function of cycle number for $Si_{85}Cr_{15}$ alloy series.

$$\xi = \frac{k\rho_{alloy}c_{alloy}}{F} * 100\% \tag{3.3}$$

Volume expansion for $Si_{85}Cr_{15}$ alloy milled for 16 hours upon electrochemical lithiation was calculated to be 120.7%, as compared to 92.3% for a $Si_{85}Fe_{15}$ alloy milled for the same amount of time; ultimately leading to poor capacity retention of $Si_{85}Cr_{15}$ alloys.

In order to compare structural characterization and electrochemical analysis, XRD can be used to predict lithiation capacities in the same way as was shown for $Si_{85}Fe_{15}$ alloys in Figure 3.17. By using relative peak area as determined by XRD analysis, active Si can be determined and capacity can be calculated as a function of milling time, as shown in Figure 3.24.

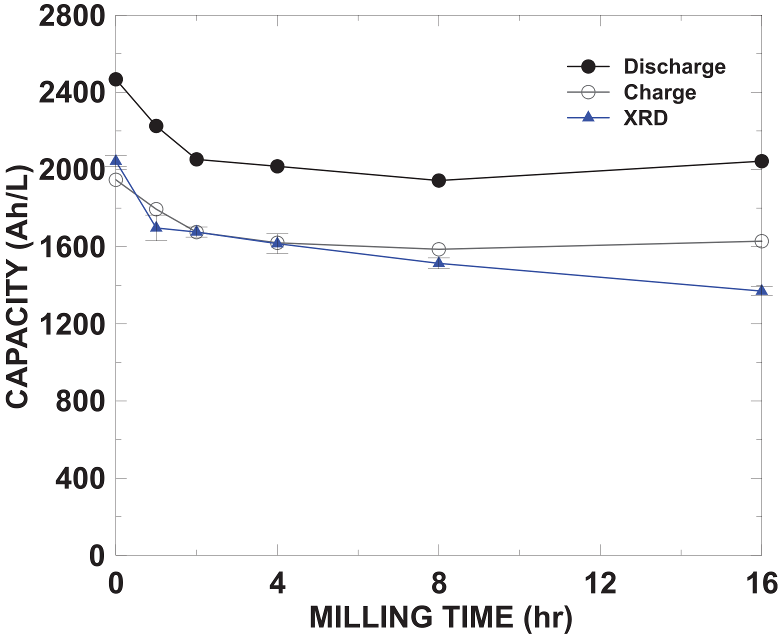

Figure 3.24 Measured charge and discharge capacity of $Si_{85}Cr_{15}$ alloy series with capacity predicted by XRD.

The un-milled 85Si + 15Cr falls within the lithiation and de-lithiation capacities as the amount of active Si is known exactly and no mechanochemical reaction has occurred; though, the model does not consistently predict a value within the lithiation and de-lithiation capacities as a milling time is increased. At milling times of 2 and 4 hours the predicted de-lithiation capacities are within error of the experimentally observed capacities, at all other milling times there is an underestimation of capacity by this model. When milling time is 8 and 16 hours, there is a significant underestimation of capacity. Underestimation of capacity can be attributed to the systematic error associated with the disambiguation of the background and a-Si. If more intensity is attributed to the background rather than a-Si, capacity will then be underestimated by XRD. As the mechanochemical reaction proceeds and a-Si increases in intensity this error becomes more pronounced.

In this case, it may be more appropriate to use the electrochemical analysis to inform the quantification of phases. This is relatively straightforward for Si-Cr alloys, since only $CrSi_2$ is formed as a result of the mechanochemical reaction of Cr and Si. Observed capacity can then be directly related to a single composition and single value of x in $Si_{(85-2x)}Cr_{(15-x)}(CrSi_2)_x$, this is shown in Figure 3.25, where theoretical capacity is plotted for this series as a function of x. Therefore, in theory, a measurement of the theoretical capacity is all that is required to precisely identify the phases present in this series. Fe contamination was additionally considered, as will be discussed in section 4.3.2, which will further decrease capacity by forming $FeSi_2$. The result of this analysis is shown in Figure 3.26, where the first cycle de-lithiation capacity was used to predict the phases present.

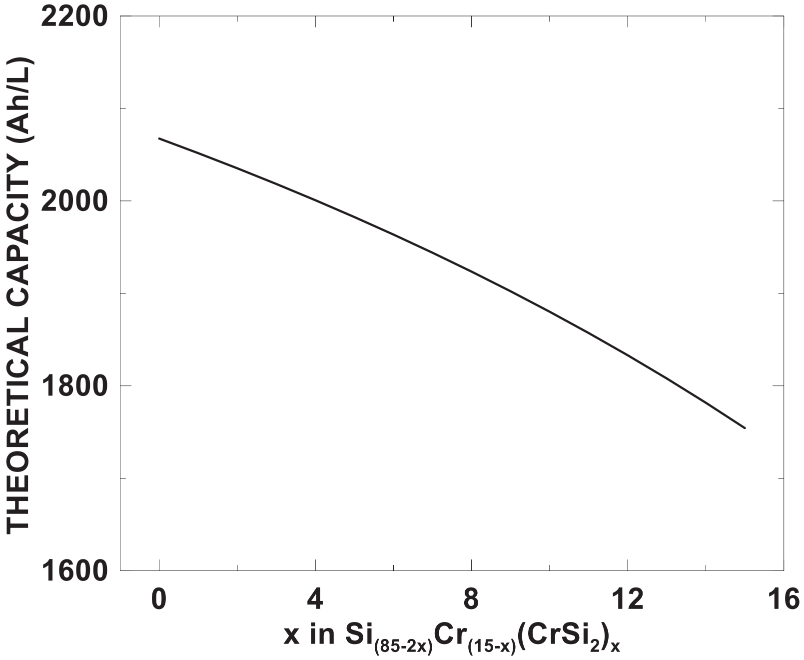

Figure 3.25 Theoretical capacity calculated as a function of the mechanochemical reaction of Si and Cr at a molar ratio of 85Si + 15Cr forming $CrSi_2$.

Using first cycle de-lithiation capacities to predict phase formation does, however, have separate limitations. The observed first de-lithiation capacity can be reduced by irreversibly trapped Li-ions in mechanically disconnected particles. This would tend to cause $CrSi_2$ formation to be overestimated. This effect would be greatest for alloys with large volume expansion, which would tend to cause the greatest amount of irreversible mechanical particle disconnection. In the case of the 16 hour milled alloy, volume expansion upon lithiation was calculated to be 120.7%, given such a large volume expansion it is likely that some Li-ions are irreversibly trapped as particles are mechanically disconnected. This is clear in Figure 3.26 where even in the un-milled alloy some $CrSi_2$ must be present to account for an observed capacity lower than the expected theoretical value of capacity. Additionally, at 4 and 8 hours of milling, there must be more $CrSi_2$ present than could possibly be formed according to the initial quantity of Cr.

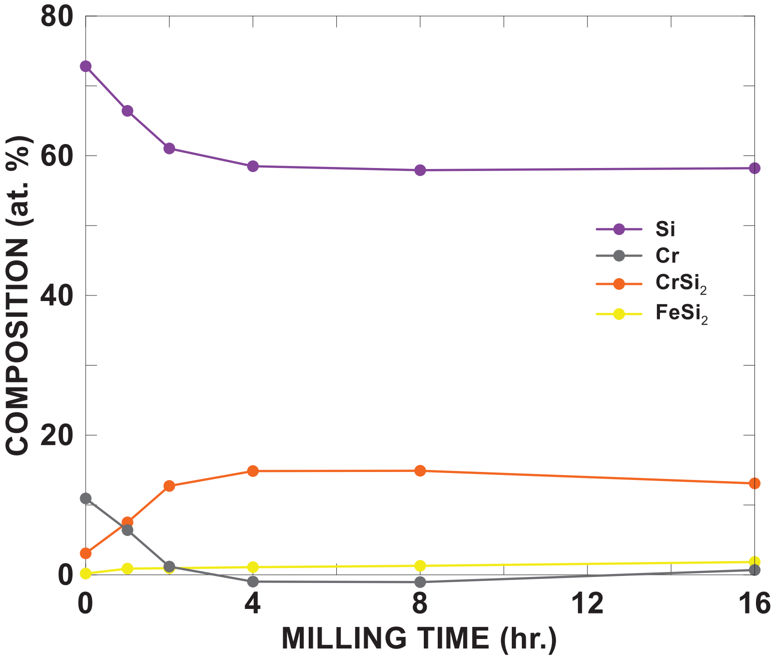

Figure 3.26 Phase analysis of $Si_{85}Cr_{15}$ alloys as a function of milling time using observed lithiation capacity to predict phase formation.

Both using the structural characterization to predict de-lithiation capacities and using de-lithiation capacities to predict phase formation have clear limitations. Using either method should be approached with caution as the error involved is likely large.

3.3 Discussion

In sections 3.1, and 3.2, the active material (with respect to lithiation) does not change, and assuming that the mechanochemical reaction is complete the final product should be relatively similar for both transition metals, where the products post milling are Si and $TMSi_2$. This, however, is not what is observed. Differences in processability of each transition metal ultimately leads to differences in the final microstructure and therefore differences in the electrochemical performance.

Varying processability of each transition metal can be directly related to its mechanical properties. Considering the mechanism by which a mechanochemical reaction occurs, the mechanical properties that govern a transition metals processability should be Young's modulus and yield strength. As described in section 2.1, Young's modulus is stress required to strain a material given that the yield strength is not exceeded. Therefore, as Young's modulus is increased, it is proportionately more difficult to strain a material, and, as Young's modulus is decreased, it becomes proportionately easier to strain a material. Given that a mechanochemical reaction requires a material to be strained beyond the elastic limit, materials with a lower Young's modulus should react more quickly as they are deformed more easily. Yield strength is the energy required to exceed the elastic limit and begin plastic deformation. Because the mechanochemical reaction requires repeated plastic deformation leading to a ductile to brittle transition, a material with a lower yield strength should react more quickly.

Young's modulus is a material property derived from the elastic region of the stress strain curve and therefore can be used to meaningfully compare one transition metal to another. This is because Young's modulus can be modeled by the interatomic potential in a two-atom system shown in Equation 3.4, where E is Young's modulus, r is the interatomic distance, r_o is the equilibrium interatomic distance, V is the potential energy.

$$E = \frac{1}{r_o}\left(\frac{\partial^2 V}{\partial r^2}\right) \tag{3.4}$$

Yield strength, however, is a material property derived from the plastic region of the stress strain curve and is therefore not strictly dependant on the elements involved. Materials properties beyond the elastic limit of the stress strain curve cannot be modeled by the interatomic potential of a two-atom system because behaviour relies on the progressive destruction of the crystal structure which is highly variable for even materials composed of the same element. For example, in the case of wrought iron (low carbon iron), ultimate tensile strength (the maximum value of a stress strain curve) when hardened and tempered can be 620 MPa with 2% elongation exceeding the elastic limit; though, as rolled (no tempering, no hardening) ultimate tensile strength can be 330 MPa with 25% elongation exceeding the elastic limit.[107] Materials properties beyond the elastic limit can be highly variable which makes it especially difficult to develop a model to predict and/or explain the mechanochemistry of a given system.

When Fe was the inactive transition metal, according to the XRD analysis the mechanochemical reaction was complete following 4 hours of milling, where the transition metal was no longer present and very little change was observed in the XRD pattern, a summary of these results is shown in Figure 3.27. This was additionally confirmed by Mössbauer spectroscopy which showed that no Fe was detected following 2 hours of milling. Fe can be described as ductile metal, which can then accumulate dislocations and become embrittled with repeated cold working. This is necessary in order for the mechanochemical reaction to occur and to reach completion in a relatively short amount of time. Though XRD showed the mechanochemical reaction to be complete, electrochemical performance in a Li-metal half cell is often more sensitive to the microstructure of the electrode as electrochemical performance continued to improve following 16 hours of milling. A summary of the electrochemical performance is shown in Figure 3.28.

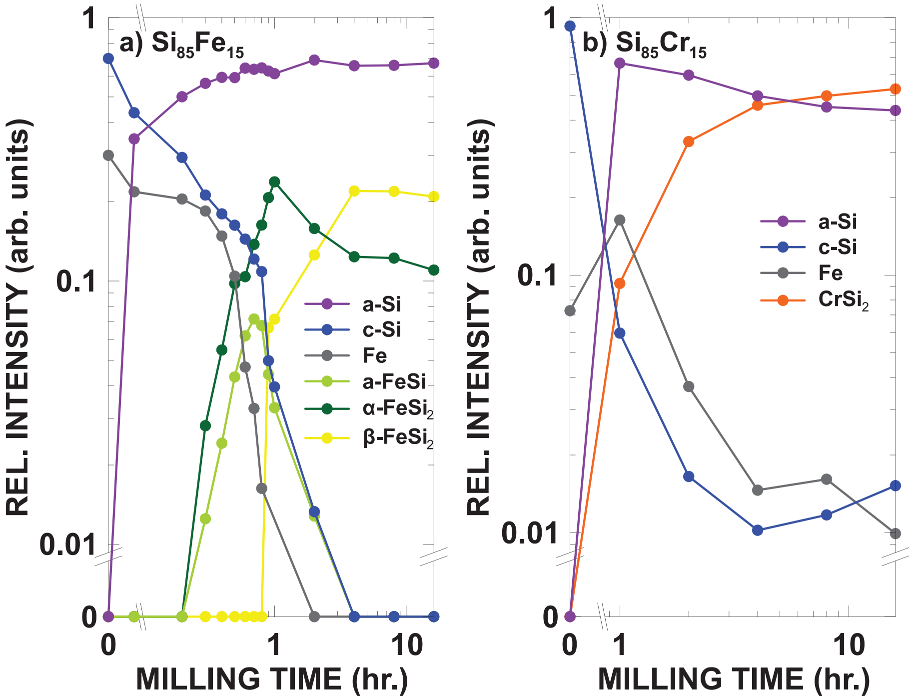

Figure 3.27 Summary of the qualitative phase analysis for the $Si_{85}TM_{15}$ (TM = Fe, Cr) as a function of milling time.

However, when Cr was the inactive transition metal XRD analysis showed that the mechanochemical reaction did not complete even after 16 hours, where some quantity of metallic Cr remained. Cr can be described as a brittle material[103] which is therefore not as suitable for mechanochemical reactions, especially with Si which is also brittle. The inability to accumulate dislocation energy prevents Cr from becoming progressively embrittled and Cr may therefore not be a suitable transition metal for the mechanochemical alloying of Si with a TM. Additionally, electrochemical results shown in Figure 3.28 show that Cr may be unsuitable as increasing potential polarization and impedance with cycle number are observed, which may indicate that Cr is catalysing the reduction of electrolyte worsening electrochemical performance as a function of cycle number.

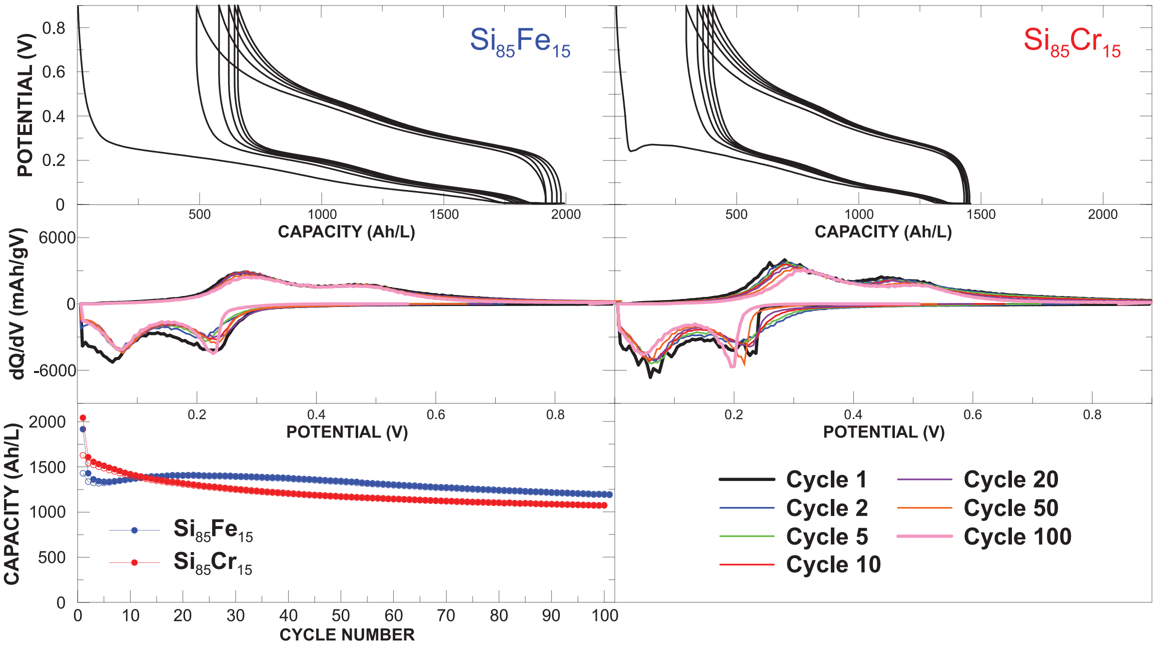

Figure 3.28 Summary of electrochemical performance $Si_{85}TM_{15}$ (TM = Fe, Cr) for a milling time of 16 hours.

The implications of the catalytic reduction of electrolyte are not as obvious in a Li-metal half cell, as there is a large excess of electrolyte and Li and therefore a substantial decrease in capacity as a function of cycle number is not observed. In a full cell format, however, there is a limited quantity of electrolyte, and Li, as Li is supplied only by the cathode material. Therefore, the continual reduction of electrolyte irreversibly consuming Li would result in a drastic decrease in capacity as a function of cycle number. Cr is therefore, not an ideal candidate for Si-TM alloy electrodes for Li-ion batteries.

3.4 Conclusions

Si as a negative electrode material in Li-on batteries has garnered considerable research interest because of its volumetric capacity, thermal stability, and relative low cost.[1] However, because Si does not store Li via an intercalation mechanism, rather by an alloying mechanism; Li storage in Si results in a volume expansion of up to 280%.[2] Such large volume expansions are detrimental to cell cycling[3,4] and therefore must be limited to some tolerable amount.

One method of limiting volume expansion is by alloying Si with a TM forming an inert TM silicide, effectively reducing the amount of active Si; therefore, reducing the total volume expansion.[1] Fe, because of its abundance in the earth's crust and relative low cost, is an ideal candidate. Cr was additionally explored as the mechanical properties of Cr are different than those of Fe. SiTM alloys were generated by a commercially relevant mechanochemical synthesis and evaluated in Li metal half cells.

It was found that in the case of Fe, the mechanochemical reaction was complete after 4 hours when evaluated by XRD and Mössbauer spectroscopy. However, it was found that further milling was required to achieve improved cycling performance when evaluated in Li-metal half cells. Following 16 hours of milling a $Si_{85}Fe_{15}$ alloy was found to cycle at a reversible capacity of 1428 Ah/L, with an irreversible capacity of 488 Ah/L (25.4%) and a capacity retention of 83.7% after 100 charge discharge cycles. In the case of Cr it was found that the mechanochemical reaction did not reach completion even after 16 hours of milling and some metallic Cr remained. Cycling performance of Si-Cr alloys was poor as compared to Fe with a reversible capacity of 1628 Ah/L for a $Si_{85}Cr_{15}$ alloy milled for 16 hours, with an irreversible capacity of 415 Ah/L, and a capacity retention following 100 charge discharge cycles of 65.7%. There was additionally evidence that Cr may be catalytically reducing electrolyte as increases in polarization and impedance as a function of cycle number were observed. As a result, Cr may not be appropriate choice as an inactive component for Si-TM negative electrode materials.

Chapter 4 **Quantitative Composition Determination by Mössbauer Spectroscopy**

4.1 Introduction

Mössbauer spectroscopy is a spectroscopic technique based on the recoilless absorption and emission of γ-rays by a nucleus and has been employed extensively in the characterization of Fe containing materials. Mössbauer spectroscopy is particularly useful because of its ability to probe the local magnetic and electronic environment of nuclei present in amorphous or nano-crystalline phases that would otherwise be undetectable by XRD .[88] Quantitative phase determination by Mössbauer spectroscopy is, however, tedious because spectral area is not directly dependent on the number of ^{57}Fe nuclei but also depends on the RFF.

When a γ-ray is absorbed or emitted by a nucleus, nuclear recoil energy is transferred to a phonon, thereby preventing the observation of nuclear γ-resonance fluorescence. The RFF represents a finite probability of a zero-phonon process, therefore allowing nuclear resonance fluorescence to occur.[85] Specifically, the RFF, $f=\exp(-\boldsymbol{k}^2\langle x^2\rangle)$, is the mean square vibrational amplitude of the resonating nucleus in the direction of observation for gamma rays of a wave vector $\boldsymbol{k}$. The RFF is commonly determined in one of three ways: the change in integrated intensity of the resonant absorption as a function of temperature, $A(T)$;[108–111] the change in isomer shift with temperature, $\delta(T)$;[112–115] or the two lattice method, where the integrated intensity of two or more known compounds is measured simultaneously.[116–119] These three approaches are discussed briefly below.

The first method for the determination of the RFF is by the change in integrated spectral intensity with temperature. The Debye model of solids considers atoms to vibrate about their mean crystallographic sites with a distribution of frequencies, dependent upon a characteristic Debye temperature, θ_D. θ_D can therefore be considered as a measure of the interatomic forces in a crystal structure; such that a large θ_D implies less motionabout the mean position and a small θ_D implies more motion about the mean position. It can then be shown that the RFF is dependent upon θ_D of a material; according to Equation 4.1: where *f(T)* is the RFF, *T* is temperature, E_R is the recoil energy of the Fe atom (1.952×10^{-3} eV) , k_B is Boltzman's constant (8.617×10^{-5} eV/K), and θ_D is a fitted parameter.

$$f(T) = \exp\left[-\frac{6E_R}{k_B\theta_D}\left(\frac{1}{4} + \left(\frac{T}{\theta_D}\right)^2 \int_0^{\frac{\theta_D}{T}} \frac{x}{e^x-1}\,dx\right)\right] \tag{4.1}$$

Change in integrated intensity, *A(T)*, with temperature can then be used to approximate θ_D, and calculate the RFF for a given material at a given temperature.

The second method for the determination of the recoil free fraction is the change in isomer shift with temperature. The measured center shift, $\delta(T)$, is the sum of the isomer shift, δ_o, and the second order doppler-shift (SOD), $\delta_{SOD}(T)$, and can be written as $\delta(T) = \delta_o + \delta_{SOD}(T)$. The SOD is the result of the thermal motion of the absorbing or emitting nuclei about their mean lattice position and is dependent upon the mean square velocity. According to the Debye model of solids, $\delta_{SOD}(T)$ can be calculated by Equation 4.2; where *T* is temperature, k_B is Boltzman's constant, M_{Fe} is the mass of an Fe atom (or effective mass), *c* is the speed of light, and θ_D is a fitted parameter.

$$\delta_{SOD}(T) = -\frac{9k_BT}{2M_{Fe}c}\left(\frac{T}{\theta_D}\right)^3 \int_0^{\frac{\theta_D}{T}} \frac{x^3}{e^x-1}\,dx \tag{4.2}$$

$\delta_{SOD}(T)$ can then be used to approximate θ_D, and the RFF can be calculated as above. These methods, where the RFF is determined by θ_D, require spectra recorded at multiple temperatures where there is only a small variation in integrated intensity, as well as SOD with temperature. The approximation of θ_d, therefore, relies on the complex analysis of experimental data and the error associated with this procedure has been determined to be significant.[111] This is shown in Figure 4.1 where the change in RFF and SOD are plotted as a function of temperature, over a 500 K temperature change there is very little variation in RFF or SOD.

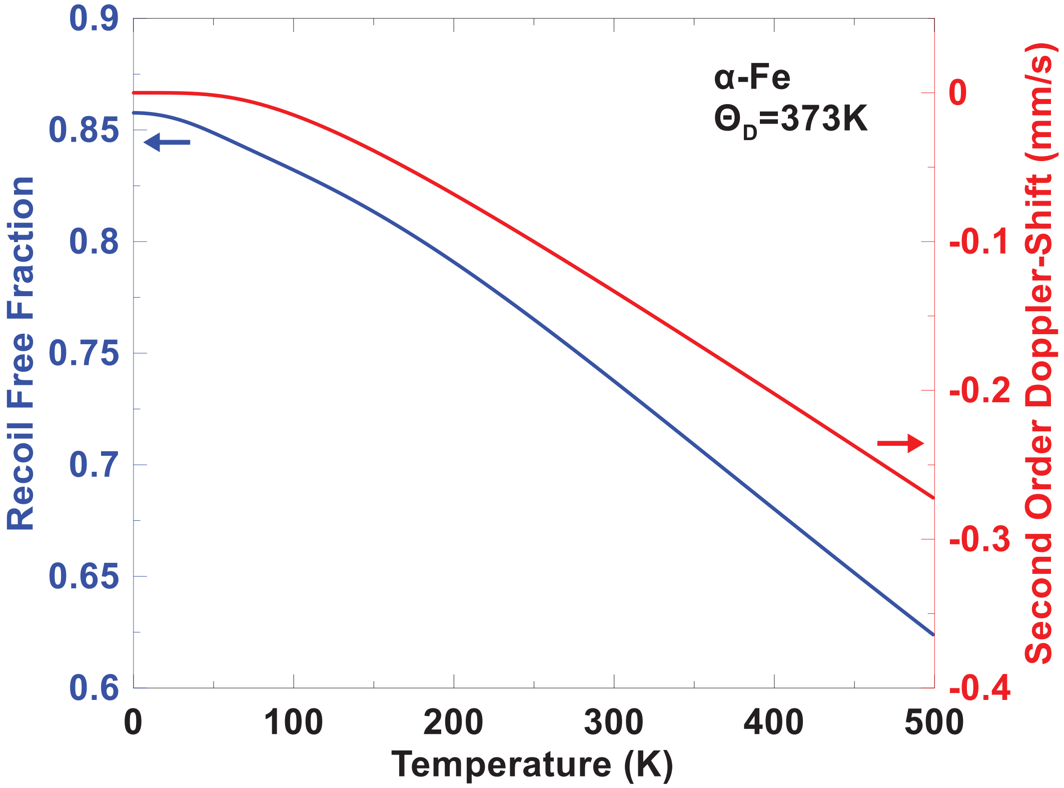

Figure 4.1 Change in recoil free fraction (left axis) and second order doppler-shift (right axis) with temperature calculated for α-Fe with θ_D of 373K.

The third method for the determination of the RFF is the two-lattice method, using the relative integrated intensity of two compounds measured simultaneously. This method, developed by Sorescu, allows for the determination of the RFF using a single room temperature measurement of a two-foil absorber.[116] It can be shown, because the integrated intensity, A, is dependent on the number of ^{57}Fe nuclei, $N(^{57}Fe)$, that if the two phases are present in known quantities, then the RFF of the two phases are related by the expression.

$$f_j = \frac{N(^{57}Fe)_i * f_i}{N(^{57}Fe)_j} * \frac{A_j}{A_i} \tag{4.3}$$

where the i and j are the indices represent the two different phases.[116]

Using the two-lattice method, the determination of the RFF is facile, although there remain some inherent accuracy limitations. Most importantly, this equation is exact only within the limit of the thin absorber approximation. When absorbers approach an appreciable thickness, there is no longer a linear response in integrated intensity.[111] Though, assuming a thin absorber, the RFF must also consider the presence of impurities as well as the occupancy of Fe in the crystal structure. Additionally, grain size has a significant effect on the RFF. For instance, it has been shown that the RFF of mechanochemically synthesized xSc_2O_3-$(1-x)$ α-Fe_2O_3, where $x = 0.1$, 0.3, and 0.5, decreases steadily with processing time as the grain size is decreased.[120] The determination of the RFF is, therefore, sensitive to a host of parameters that are often unknown or vary considerably from case to case. Because of this literature, RFF values cannot be used blindly in quantitative phase analysis for mixtures of Fe-containing species. Instead, RFF values should be determined independently for each species, if quantitative phase analysis is the goal. Since the goal of this study is strictly quantitative phase analysis, a response factor, F, is used to correlate the integrated intensity from one Fe-containing species to another, shown in Equation 4.4, where F encompasses all of the effects that impact quantitation, including the RFF. Quantitative phase analysis is then enabled by the addition of an internal standard (IS) for which the response factor is known. Thus, the amount of Fe in a species with an unknown (unk) concentration may be expressed in terms of the amount of Fe in the IS by the relation:

$$N(^{57}Fe)_{unk} = \frac{N(^{57}Fe)_{IS} * F_{IS}}{F_{unk}} * \frac{A_{unk}}{A_{IS}} \tag{4.4}$$

A similar method was used by Arredondos et. al in a previous study to identify and quantify Fe phases in medicines.[121] The novelty of the approach developed here is the use of a Bellcore plastic film. The unknown and IS are mixed homogeneously in slurry containing a plasticizer that when solidified forms a plastic film. Using a plastic film not only ensures that a homogenous mixture is maintained but also allows careful control of the Fe loading in the film ensuring that the thin absorber approximation is never exceeded, and quantitative results are always achieved.

The intention of the present work is to develop a general method for quantitative Mössbauer spectroscopy that can be extended to any powder system and most importantly, to systems where alternative methods of characterization are difficult or impractical. This is especially true for mechanochemically synthesized Si alloys.

Mechanochemical synthesis is a powder processing technique widely used in the fields of powder metallurgy, magnetic materials and hydrogen storage. Powder particles trapped between colliding milling media are stressed beyond their elastic limit and plastically deformed. Repeated plastic deformation leads to a ductile to brittle transition and eventually fracture. Upon fracture, fresh reactive surfaces are generated, and alloys can be formed at room temperature. An inherent drawback of mechanochemical synthesis is contamination from milling media, vessel, and atmosphere. Atmospheric contamination is easily preventable; however, contamination from milling tools is unavoidable.[122,123]

Therefore, in any mechanochemically synthesized powder there will always be some quantity of Fe contamination when milling tools are composed of Fe.

Traditionally, inductively coupled plasma atomic emission spectroscopy (ICP-AES) or ICP mass spectrometry (ICP-MS) are used to quantify the atomic composition of powdered samples. This is difficult in the case of Si because in the conventional approach, acid digestion by hydrofluoric acid (HF) is time consuming, requires constant attention and is prone to partial loss of analyte by evaporation of volatile fluorides.[124] Microwave assisted sample preparation techniques have been adapted such that atomic composition can be determined by ICP without the use of HF. US EPA Method 3051 is one such method, however, when using only HNO_3, complete sample dissolution is not always achieved, and analyte may remain bound in silicate structures. Variations on US EPA Method 3051 have been developed to optimize total sample dissolution and total element recovery,[125,126] however, when Fe is the only element of interest (as in the case of Fe contamination by mechanochemical synthesis), quantitative Mössbauer spectroscopy offers a very distinct advantage. ICP analysis is strictly limited to quantitative Fe determination independent of Fe containing phases, however, Mössbauer spectroscopy is able to identify the phases present while additionally offering quantitative Fe phase analysis. Using the method for quantitative Mössbauer spectroscopy developed in the present work, it is possible to quantify Fe contamination of mechanochemically synthesized Si alloys.

4.2 Experimental

Samples comprising known mixtures of iron (III) citrate (IC, $FeC_6H_5O_7$, 99% Sigma Aldrich) and calcium acetate (CA, $Ca(C_2H_3O_2)_2$, 99%, Alfa Aesar) were used for proof of concept. IC and CA powder mixtures were combined by mortar and pestle in known quantities such that the total Fe content was 0.5, 1, 2, 5, or 10 wt.%.

Ball milled Si was prepared from Si (99%, -325 mesh, Sigma-Aldrich) precursor powder. A total of 0.5 mL of precursor powder was loaded into a 65 mL hardened steel milling vial (SPEX model 8000-D, Spex CertiPrep, Metuchen, NJ) with 180g of 1.6 mm stainless steel balls. Loaded vials were sealed under an argon atmosphere.

Ball milled Si-TM alloys were prepared from precursor powders: Si (99%, -325, Sigma-Aldrich), V (99.5%, -325 mesh, Alfa Aesar), Cr (99%, -325, Alfa Aesar), Ti (99%, -325, Alfa Aesar), Ni (99.8%, -325, Alfa Aesar). A total of 0.5 mL of powder was loaded into a 65 mL hardened steel milling vial (SPEX model 8000-D, Spex CertiPrep Metuchen, NJ) with 180 g of 1.6 mm stainless steel milling balls. Loaded vials were then sealed under an argon atmosphere.[81]

X-ray diffraction patterns were collected using a Rigaku Ultima IV diffractometer with a Cu K_α X-ray source operating at 40 kV and 45 mA and a diffracted beam monochromator. Room temperature ^{57}Fe Mössbauer spectroscopy was conducted using a SEE Co. spectrometer operating in the constant acceleration mode with a ^{57}Co(Rh) source. The velocity scale was calibrated according to room temperature α-Fe foil. Mössbauer analysis of powdered samples prior to the addition of the IS were performed in a 4 cm^2 PET sample holder, at a mass loading of 15 mg Fe/cm^2.

Free-standing Bellcore plastic films[127,128] comprising powder samples and the IS (Fe_2O_3 powder, 99%, Sigma-Aldrich) were used for quantitative Fe content determination by Mössbauer analysis. These films were made by first preparing slurries according to the formulation: powder sample/poly(vinylidene fluoride-co-hexafluoropropylene) (PVDF-HFP, Kynar Flex 2801, Arkema)/dibutyl phthalate (99% Sigma-Aldrich)/Acetone (Fisher Scientific, Certified ACS), in a mass ratio of 0.12/0.06/0.10/0.72. Slurries were mixed homogeneously using a Mazerustar planetary mixer (Kurabo Electronics, JP) and mixed three times for 100 seconds at a rotational frequency about the primary axis of 1140 rpm and at a rotational frequency about the secondary axis of 680 rpm. The slurry was then spread onto a glass substrate using a PTFE coating bar with a 0.2 mm gap. Free-standing films were peeled off the glass substrate after air drying.

The composition of powders in the Bellcore films are listed in Table 4.1. The quantity of Fe_2O_3 IS was varied systematically throughout this work such that the amount of Fe nuclei in the Fe_2O_3 IS approximately matched the amount of Fe in the sample. For samples containing an unknown amount of Fe, a trial Bellcore film was made with an estimated amount of IS added, the Fe content of the sample was measured by Mössbauer spectroscopy, and then a new Bellcore film was made with the quantity of IS adjusted to more closely match the sample powder Fe content.

Table 4.1 Mass of sample and Fe_2O_3 IS powders in all Bellcore plastic films used for quantitative Fe content determination

			Fe-content (μmoles)	
	Sample (g)	Fe_2O_3 (g)	Sample	Fe_2O_3
IC 0.5% Fe	0.29743	0.00215	27.0	26.9
IC 1.0% Fe	0.29602	0.00478	52.8	59.8
IC 2.0% Fe	0.29333	0.00682	99.2	85.4
IC 5.0% Fe	0.29632	0.01984	266	248
IC 10% Fe	0.28483	0.02808	504	351
Si 0 hr	0.60493	0.02326	43.0	291
Si 1 hr	0.59966	0.02521	141	316
Si 2 hr	0.60136	0.02350	168	294
Si 4 hr	0.59724	0.02352	211	294

Si 8 hr	0.59362	0.02646	230	331
Si 16 hr	0.60101	0.02354	234	295

Scanning electron microscope (SEM) images were collected using a TESCAN MIRA 3 field-emission scanning electron microscope. Independent Fe content determination by ICP-OES was performed using a PerkinElmer Optima 8000 ICP optical emission spectrophotometer.

4.3 Results and Discussion

4.3.1 Proof of Concept

In order to quantify the iron content of samples using Equation 4.4, powder samples must be blended with a known quantity of IS. In this study Fe_2O_3 powder was used as the IS. To ensure homogeneity, powder samples and the Fe_2O_3 IS were combined in free standing Bellcore plastic films.[127] Such films were originally designed for use in Li-ion polymer batteries,[127,128] where good coating homogeneity is also required for even current distribution. Figure 4.2 a) shows a resulting Bellcore plastic film with composition 10% IC as shown in Table 4.1. The film is about 50 ± 10 μm thick and contains a homogeneous mixture of known amounts of the sample and IS, as shown in Figure 4.2 b) and d). The films were cut into 4 equal sections, which were then folded to create a sample for Mössbauer measurement, shown in Figure 4.2 e). Mössbauer spectra and Fe content were measured for each section individually. Error bars were then calculated according to the standard error across the measurement of each of the four sections.

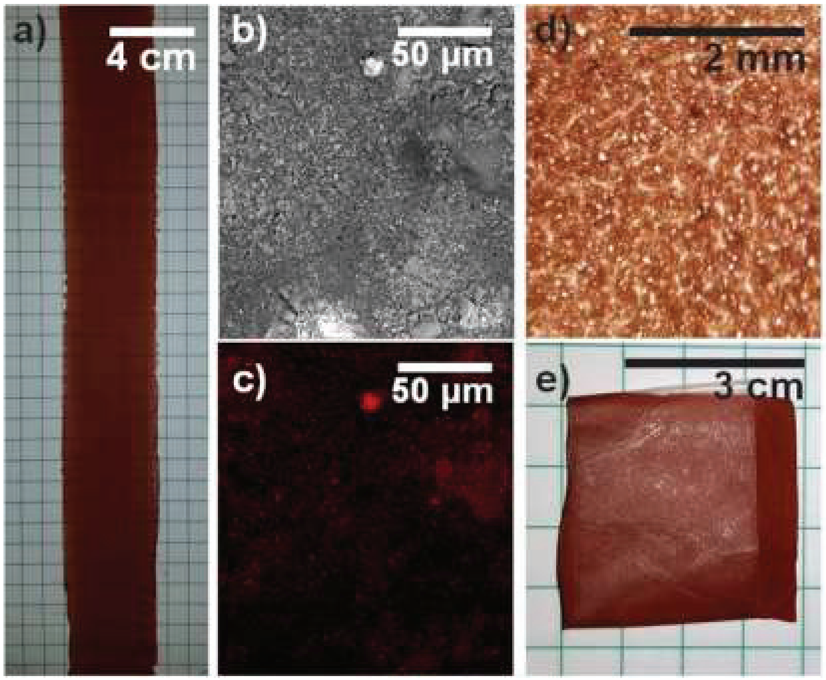

Figure 4.2 a) Optical image of a Bellcore plastic film with a 10% Fe IC/CA mixture with Fe_2O_3 IS, b) SEM image, c) EDS map of Fe in red, d) optical microscope image of the Bellcore plastic film, and e) the same Bellcore plastic film folded for Mössbauer analysis.

In order to verify the merit of this method for quantitative Mössbauer spectroscopy, a series of powdered samples were generated with known Fe content using mixtures of iron (III) citrate (IC) and calcium acetate (CA). IC and CA were selected because they are not excessively hygroscopic, can be ground to fine particles, dispersed uniformly in a Bellcore plastic film, and are both soluble in mineral acid and therefore suitable for independent Fe-content confirmation by ICP-OES analysis. Since the hydration number of IC may vary from 9-11 H_2O per formula unit, its true Fe content was first determined by ICP-OES and was found to be 18.2 ± 0.1 wt.% Fe. In this way the Fe content in different IC/CA mixtures was known, allowing the determination of the response factor from their Mössbauer spectra in Bellcore films with known quantities of Fe_2O_3 IS. Figure 4.3 a) shows a Mössbauer spectrum of pure IC powder. This spectrum was fit with a single doublet, with fitting parameters listed in Table 4.2. From this spectrum, the fitting parameters (center shift (CS), quadrupole splitting (QS), and line width (FWHM)) for IC were obtained. Figure 4.3 a) also shows the Mössbauer spectrum of pure Fe_2O_3 powder, which was fit with a single sextet with fitting parameters listed in Table 4.2. From the IC and Fe_2O_3 spectra, it can be seen that the Fe_2O_3 spectrum can be easily discerned from the IC spectrum and furthermore that no Fe_2O_3 is present in the IC. This makes Fe_2O_3 an ideal IS for Fe content determination for these IC/CA samples.

Table 4.2 Mössbauer fitting parameters for the pure phases of the Fe containing species evaluated in this work, where H is the hyperfine magnetic field in Tesla units.

	IC	Fe_2O_3	$FeSi_2$
CS (mm/s)	0.4241	0.3857	0.1443
QS (mm/s)	0.6112	-0.1064	0.5587
HWHM (mm/s)	0.4754	0.3195	0.4823
H (T)		51.52	

Figure 4.3 b) shows the Mössbauer spectrum of a 10 wt.% Fe IC/CA Bellcore film containing Fe_2O_3 IS. The spectrum was fitted according to a sextet corresponding to the Fe_2O_3 IS, and a doublet corresponding to IC. From their relative integrated areas, the IC/IS response factor was determined to be 0.55 ± 0.02. After having determined the response factor, Mössbauer spectra were recorded for Bellcore films containing the IS and IC/CA mixtures with different Fe contents, by varying the IC/CA ratio. These spectra were fitted, and the total integrated intensity of each species was used to quantify Fe content, using the response factor found for the 10 wt.% IC/CA Bellcore film. Fe contents were also measured by ICP-OES for comparison.

Figure 4.3 c) shows the results of this quantitative Fe determination, where Mössbauer results are plotted on the y-axis, ICP-OES results are plotted on the x-axis, and the dashed line represents the target Fe content. The Mössbauer analysis was found to be within the error of the ICP-OES results for Fe content in all cases. The ICP-OES error was found to be smaller than the data symbol size shown in Figure 4.3 c) for all Fe contents, though this accounts only for instrumental error.

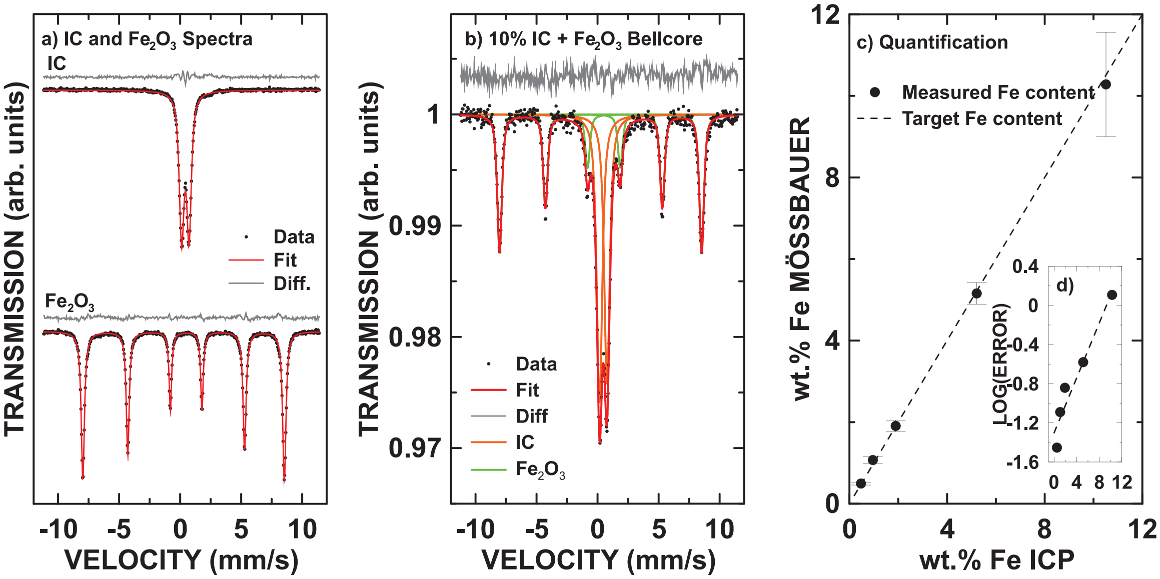

Figure 4.3 a) Mössbauer spectra of pure IC and Fe_2O_3, b) Mössbauer spectrum of a 10% Fe IC/CA mixture with Fe_2O_3 IS, c) quantitative Fe analysis using Mössbauer spectroscopy and ICP-OES, and d) log(error) as a function of Fe content.

The observed error in the Mössbauer measurement, however, increases with the Fe content. Figure 4.3 d) shows a plot of log(error) as a function of Fe content for the Mössbauer results. The linear relationship implies an exponential increase in error with Fe content. This error may be caused by adsorption effects. Because error is calculated according to spectra recorded along four different sections of the same free-standing film, another source of error could be the result of non-homogeneity in the film. At higher Fe contents, a large disparity in the density of the IC, CA and Fe_2O_3 powders could result in their separation as the film is being cast. This was confirmed as Fe contents in the leading side of the films as coated were systematically higher than those in the tailing side of the film. To remedy this effect, more advanced coatings could be used, that include thickeners to prevent particle settling. In this study, these effects were kept to a minimum by using a minimal amount of acetone to increase slurry viscosity. In order to avoid absorption effects, mass loadings were kept under 15 mg Fe/cm^2. Quantifying Fe Contamination Ball Milled Si

Si alloys have garnered considerable research interest as potential anode materials in lithium-ion batteries offering a ~22% increase in energy density compared to a graphite anode.[23] Such alloys need to have small grain size to have good charge/discharge cycle lifetimes. Transition metal or carbon can also be added to reduce volume expansion during cycling, also extending lifetime. Such alloys are often made by mechanochemical synthesis using steel vials and milling media to reduce cost.[129] However, Fe contamination from ball milling results in the formation of $FeSi_2$, which is inactive towards lithium.[23] Not only does this reduce cell capacity, but an unknown amount of Fe contamination consequently makes the lithiation capacity of the material also unknown. This is not acceptable in the production of Li-ion batteries where the cathode and anode capacities must be precisely balanced. It is, therefore, important to understand the relationship between processing time and Fe contamination. However, as mentioned in the introduction, this is difficult to achieve by conventional methods. For instance previous measurements for Fe in ball milled Si by energy dispersive X-ray analysis could not detect any Fe contamination,[129] while previous measurements by ICP-OES suggested ball milled Si contains 0.7 - 1 at.% Fe.[81] Although many publications about ball milled Si, Si-C and Si-metal alloys have been published, to our knowledge, no detailed analysis has been carried out on the amount of Fe contamination introduced.

Figure 4.4 a) shows XRD patterns of the un-milled Si precursor and Si that was ball milled for 16 hours. A significant reduction in grain size and amorphization is observed in the milled sample by the broadening of the Si peaks; however, neither Fe nor $FeSi_2$ were detected by XRD. Figure 4.4 b) shows the Mössbauer spectra for the same samples, where a symmetric doublet consistent with $FeSi_2$[100–102] is observed, even in the un-milled precursor powder. Details of the fitting are listed in Table 4.2. This demonstrates the sensitivity of the Mössbauer method, since the supplier's certificate of analysis (COA) of the precursor Si powder indicates the presence of only 0.2 at.% Fe. This small amount of Fe contamination is undetectable by XRD, but easily detected by Mössbauer spectroscopy. The quantification of the iron contamination is discussed below.

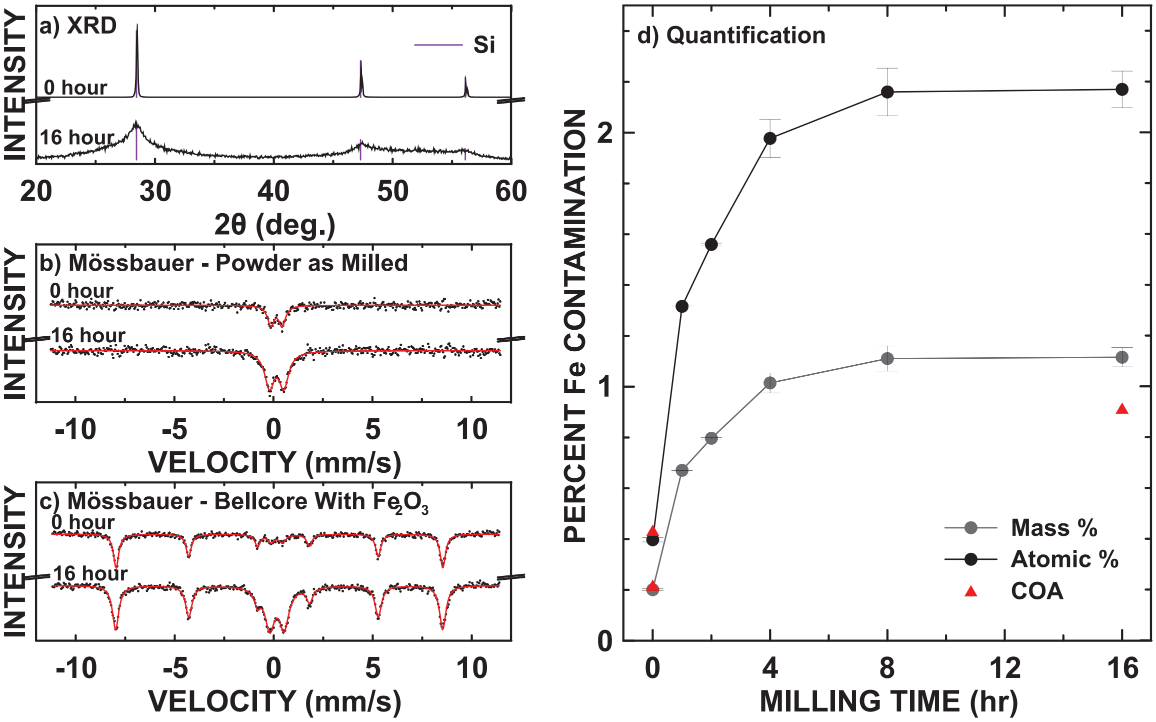

Figure 4.4 a) XRD of un-milled Si and Si milled for 16 hours, b) Mössbauer spectra of un-milled Si and Si milled for 16 hours, c) Mössbauer spectra of un-milled Si and Si milled for 16 hours after being cast in a Bellcore plastic film with Fe_2O_3, and d) quantitative Mössbauer spectroscopy results.

Milled Si powders and the Si precursor powder were cast into Bellcore plastic films with the addition of a known quantity of Fe_2O_3, as listed in Table 4.1. Figure 4.4 c) shows the Mössbauer spectra recorded for Bellcore plastic films made with the un-milled Si precursor and the Si sample that was milled for 16 hours. The integrated intensity of each phase was used to quantify Fe contamination. Figure 4.4 d) shows the results of the quantification of Fe contamination as a function of milling time. To our knowledge this is the first reported measurement of Fe contamination in ball milled Si as a function of milling time. Error bars represent the standard error across four measurements conducted for different sections of each film. Fe contamination increases rapidly during the first 4 hours of milling reaching a plateau where increasing milling time does not increase Fe content substantially. This trend is coincident with trends in grain size reduction, which, under the same milling conditions used here, also decreases substantially during the first 4 hours of milling and then reaches a steady state after 8 hours.[81] Large Si grains are likely more abrasive than smaller grains, resulting in a lower increase in Fe contamination as grain size is reduced. The red triangles represent Fe contamination in the Si precursor powder, as indicated by the supplier's COA. There is excellent agreement between the method developed in this work and the COA. After 16 hours of milling the Fe contamination was determined to be 1.12 ± 0.07 at.%. Therefore, 0.201 ± 0.004 at.% Fe was present in the Si precursor and 0.92 ± 0.07 at.% Fe was introduced as contamination from ball milling. This is consistent with earlier estimates of Fe contamination by ICP-OES.[81]

4.3.2 Quantifying Fe Contamination in Ball Milles Si-TM Alloys

When there is a large difference in hardness of the powder and the milling media, substantial contamination is introduced as the result of metal-metal abrasion. For example, in the case of WC milled using stainless-steel media, Fe contamination was found to be as high as 33 atomic percent.[130] Si alloys for lithium-ion batteries often contain an inactive phase thereby forming an inactive silicide, buffering the volume expansion of Si upon lithiation and improving charge/discharge cycle lifetime. Introducing an inactive phase can then inadvertently increase Fe contamination. It is especially important to understand the relationship between the inactive phase and Fe contamination introduced during ball milling such that Fe contamination can be minimized.

A series of V-Si alloys were produced at a composition $V_{15}Si_{85}$ where milling time was varied from 0 to 1, 2, 4, 8, and 16 hours, and Fe content was quantified. Though Fe is an ideal transition metal candidate for commercial Si-TM alloys for Li-ion batteries, V was selected in this work as an inactive alloying element, as opposed to Fe, because it is difficult to distinguish Fe as a precursor from Fe introduced as contamination. Figure 4.5 a) shows the XRD patterns of the $V_{15}Si_{85}$ series. By fitting the XRD patterns using pseudo-Voigt functions corresponding to the known crystalline phases, the relative intensity of each phase can be quantified additionally grain size can be approximated by peak width using the Scherrer equation. An example fit of the $V_{15}Si_{85}$ alloy milled for 4 hours is shown in Figure 4.5 b), and the qualitative phase analysis is shown in Figure 4.5 c). XRD is unable to detect Fe contamination as no reflections from metallic Fe nor $FeSi_2$ are observed. The Mössbauer spectra of the $V_{15}Si_{85}$ alloys, shown in Figure 4.6 a); however, shows that Fe is easily detected by Mössbauer spectroscopy. The Mössbauer spectra show that after milling at least two Fe containing phases are detected: a symmetric doublet consistent with Fe in $FeSi_2$, as well as a singlet corresponding to amorphous Fe in Si. As indicated by Norem et al., the isomer shift of amorphous Fe in Si is 0.505 mm/s.[131] This is in agreement with the isomer shift of the singlet that is observed for all alloys formed in this series which was found to be on average 0.510±0.05 mm/s.

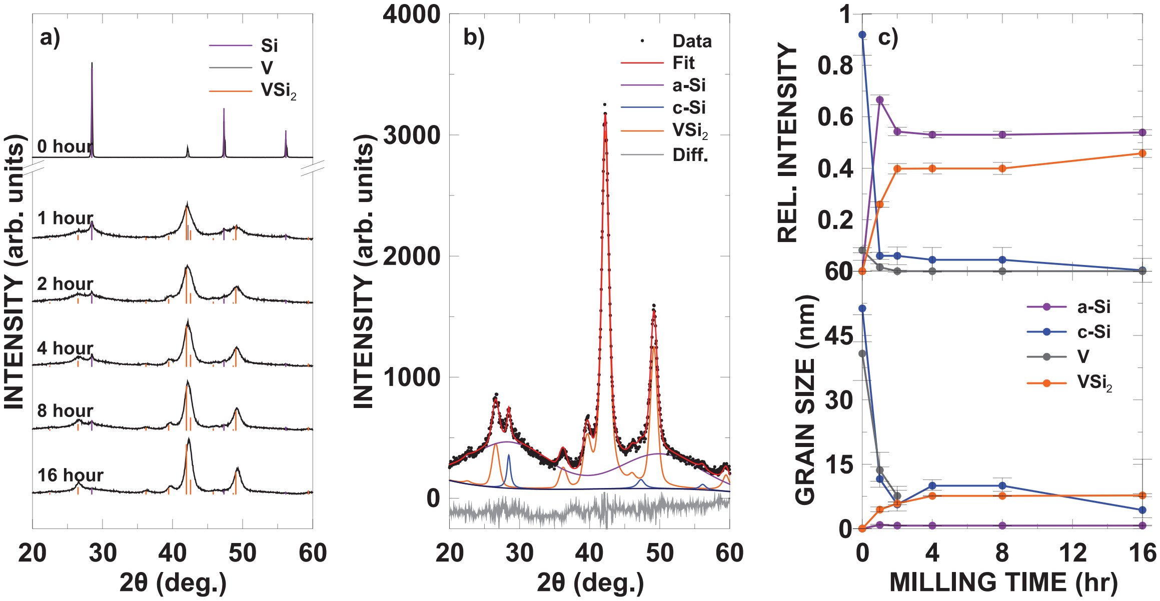

Figure 4.5 Mössbauer spectra of $V_{15}Si_{85}$ series for a) powdered sample as milled, b) Bellcore films with added IS, and c) Fe quantified Fe contamination.

All $V_{15}Si_{85}$ alloys were then combined with a known quantity of Fe_2O_3 and cast into a Bellcore plastic film. The composition of all films is shown in Table 4.3. Each film was cut into four equal sections, and a Mössbauer spectrum was recorded for each section. Figure 4.6 b) shows the a Mössbauer spectra recorded for a single section of Bellcore plastic coating for the $V_{15}Si_{85}$ series. Using the integrated intensity of each phase, as well as the pre-determined response factor, the Fe content was quantified as a function of milling time shown in Figure 4.6 c). When V is introduced, Fe content is roughly double that of milled Si precursor alone. Additionally, when V is introduced, the Fe content does not reach a steady state and instead a continual increase in Fe content with milling time is observed. It therefore becomes increasingly important to evaluate electrochemical performance as milling time is increased when there is a transition metal present so that the minimum required milling time can be determined where acceptable electrochemical performance is observed, therefore minimizing Fe contamination. Fe content of the $V_{15}Si_{85}$ alloy milled for 16 hours was determined to be 3.7 ± 0.1 wt. %; that is, 0.27 ± 0.01 wt. % Fe present in the $V_{15}Si_{85}$ precursor and 3.4 ± 0.1 wt. % Fe introduced as contamination from the milling tools.

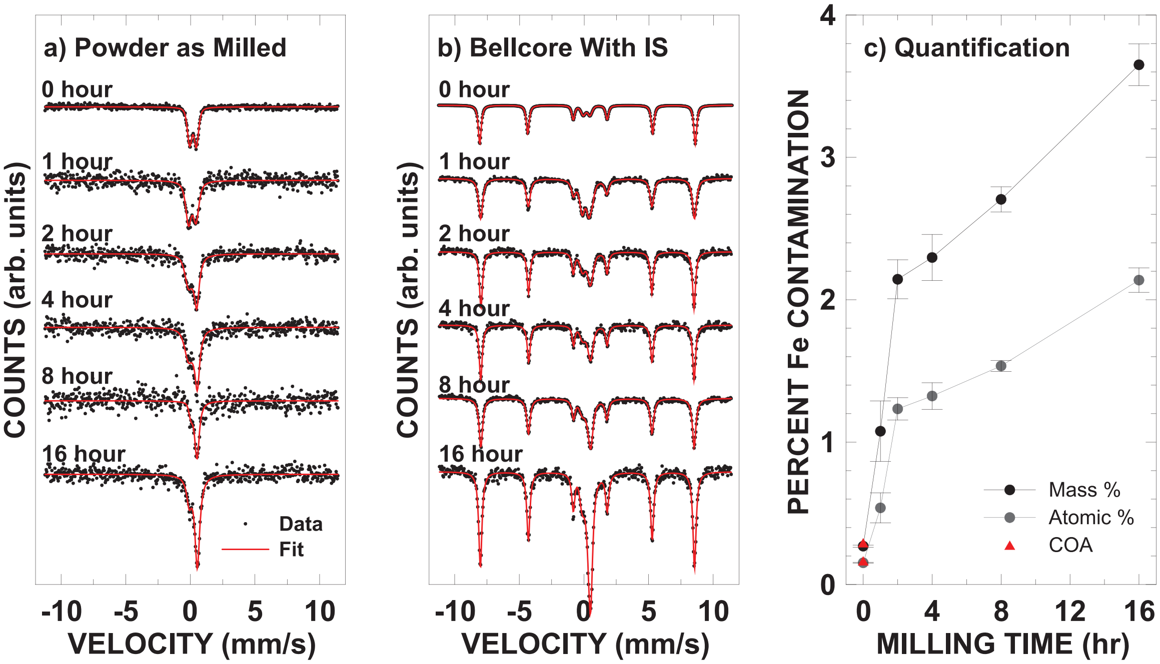

Figure 4.6 Pseudo-Voigt fit of Mössbauer spectra collected for the $V_{15}Si_{85}$ series a) as milled, b) in a Bellcore plastic film with Fe_2O_3 IS, and c) Fe contamination quantified as a function of milling time, where the red triangles represent the certificate of analysis from the supplier.

Though Fe contamination is not immediately detectable by XRD, its presence is implied. Figure 4.7 a) shows the XRD patterns collected for all $V_{15}Si_{85}$ alloys in this series, specifically focusing on the VSi_2 112 reflection. As milling time is increased a uniform shift of the 112 reflection to progressively higher angles is observed. This shift is consistent with a contraction of the crystal lattice as Fe is substituted for V in the crystal structure of VSi_2. Lattice constants of the VSi_2 crystal structure were refined and a linear relationship was found between the quantified Fe contamination and the lattice constant, a. This is shown in Figure 4.7 b) where the lattice constant, a, is plotted as a function of Fe contamination. The linear fit assumes a y-intercept of 4.5723 Å (lattice constant of pure VSi_2) and the linear relationship is maintained with a coefficient of determination, $R^2 = 0.993$. This does not, however, imply that all Fe contamination is stored as a substitutional impurity in VSi_2, rather, that as Fe contamination is increasing there is a proportional increase in the substitution of Fe for V in the VSi_2 structure.

Table 4.3 Mass of sample and Fe_2O_3 IS powders, as well quantified Fe content in and Fe_2O_3 IS in mmoles for all Bellcore plastic films used for quantitative Fe content determination.

			Fe-content (mmoles)	
	Sample (g)	Fe_2O_3 (g)	Sample	Fe_2O_3
$V_{15}Si_{85}$ 0 hr	0.60305	0.01327	2.908	3.373
$V_{15}Si_{85}$ 1 hr	0.60504	0.0402	11.66	13.48
$V_{15}Si_{85}$ 2 hr	0.58879	0.04546	22.60	26.85
$V_{15}Si_{85}$ 4 hr	0.59782	0.04495	24.58	28.76
$V_{15}Si_{85}$ 8 hr	0.60083	0.04878	29.10	33.88
$V_{15}Si_{85}$ 16 hr	0.60083	0.04878	39.27	45.71
$Cr_{15}Si_{85}$ 0 hr	0.31244	0.00998	1.813	4.059
$Cr_{15}Si_{85}$ 1 hr	0.31265	0.01264	8.650	19.35
$Cr_{15}Si_{85}$ 2 hr	0.29615	0.01145	8.740	20.64
$Cr_{15}Si_{85}$ 4 hr	0.29955	0.01428	10.22	23.88
$Cr_{15}Si_{85}$ 8 hr	0.60215	0.02445	23.91	27.77
$Cr_{15}Si_{85}$ 16 hr	0.29733	0.01194	16.67	39.21
$Ni_{15}Si_{85}$ 16 hr	0.31149	0.01144	12.07	27.11
$Ti_{15}Si_{85}$ 16 hr	0.29527	0.02360	7.006	16.59

Fe contamination was then evaluated for a series of ball milled $Cr_{15}Si_{85}$ alloys where milling time was 0, 1, 2, 4, 8, and 16 hours. Cr was chosen as the mechanochemistry of Cr and Si is drastically different than that of V and Si. This is shown in Figure 4.8 a) where an identical analysis of the XRD patterns to the $V_{15}Si_{85}$ series is performed. Figure 4.8 a) shows that even after 16 hours of milling some metallic Cr remains unreacted and the mechanochemical reaction does not reach a steady state. Additionally, the grain size of metallic Cr does not decrease as milling time is increased. The cause of Fe contamination in ball milled samples is often attributed to metal-metal abrasion; however, as shown in Figure 4.8 b), less Fe contamination is observed when milling $Cr_{15}Si_{85}$.

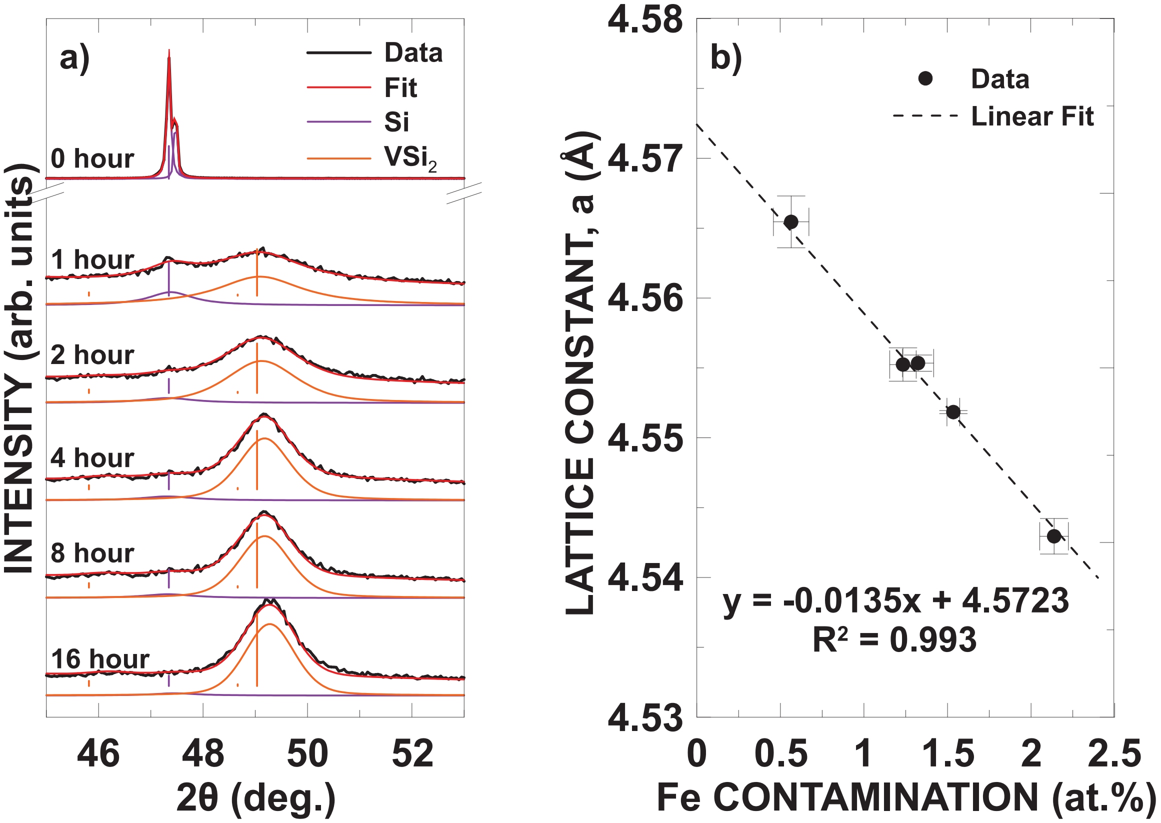

Figure 4.7 a) XRD pattern and pseudo-Voigt fit of VSi_2 112 reflection, and b) refined lattice constant, a, as a function of quantified Fe contamination.

Despite the presence of metallic Cr at every milling time, less Fe contamination is observed in the $Cr_{15}Si_{85}$ series when compared to $V_{15}Si_{85}$. After 16 hours of milling, Fe content was found to be 3.1 ± 0.1 wt. % Fe, that is 0.32 ± 0.03 wt. % Fe detected in the precursor, and 2.8 ± 0.1 wt. % Fe incorporated strictly as contamination from the milling tools. A similar trend in Fe content as a function of milling time is observed for both $V_{15}Si_{85}$ and $Cr_{15}Si_{85}$ where a large fraction of the Fe contamination is introduced in the first 2 hours and Fe contamination continually increases with milling time and does not reach a plateau.

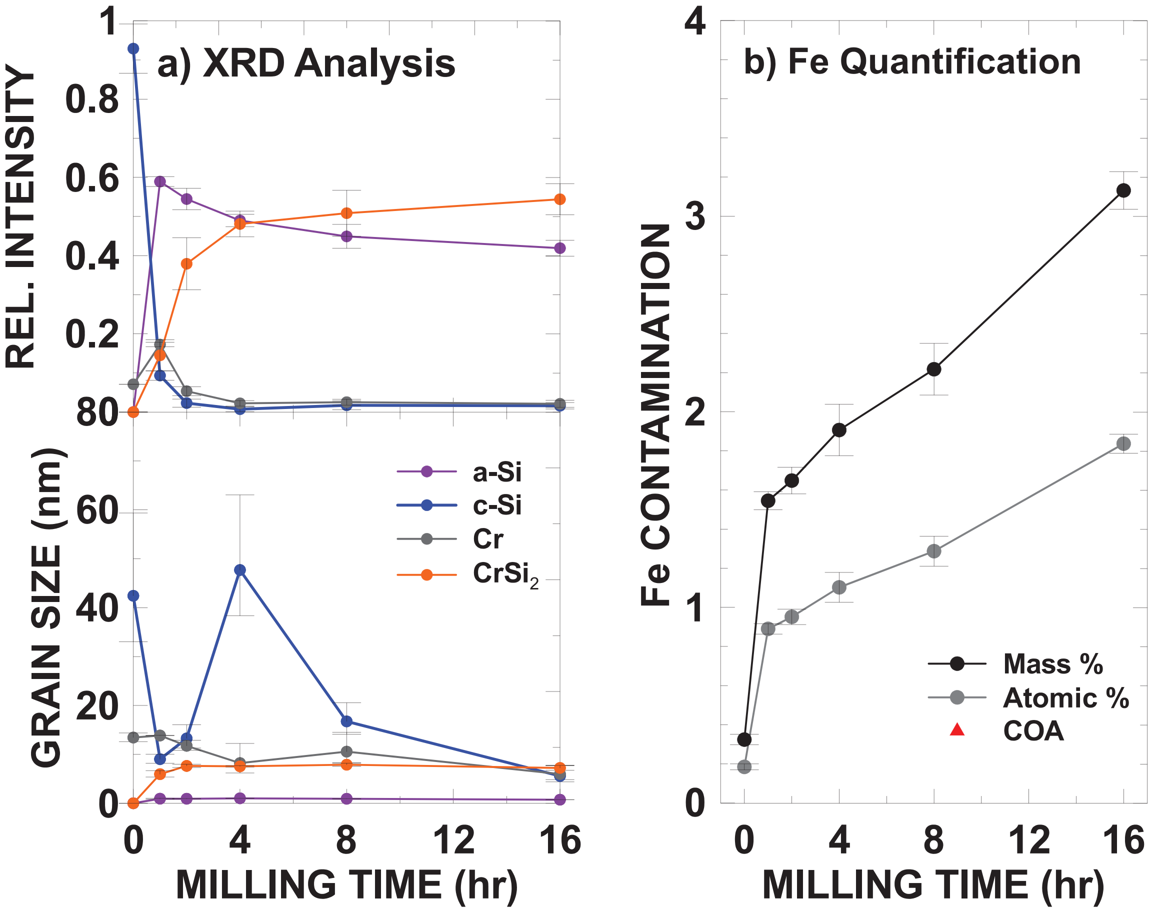

Figure 4.8 a) qualitative phase analysis of the $Cr_{15}Si_{85}$ series by XRD, and b) quantified Fe contamination as a function of milling time.

Since the TM, and $TMSi_2$ phases present in most Si-TM alloys are inactive in a Li-ion cell, the inactive phase can then be selected such that Fe contamination introduced from milling tools is minimized. A series of Si-TM alloys were produced at a composition of $TM_{15}Si_{85}$ and milled for 16 hours. Fe content was quantified by Mössbauer spectroscopy in order to determine the Fe contamination introduced from the milling tools. Total Fe content of each alloy is shown in Figure 4.9. Fe content is at a maximum when the inactive phase is V, at 3.7 ± 0.1 wt. % Fe, followed by Cr at 3.1 ± 0.1 wt. % Fe, then Ni at 2.16 ± 0.07 wt. % Fe, and finally Fe content is at a minimum when the inactive phase is Ti at 1.33 ± 0.04 wt. % Fe.

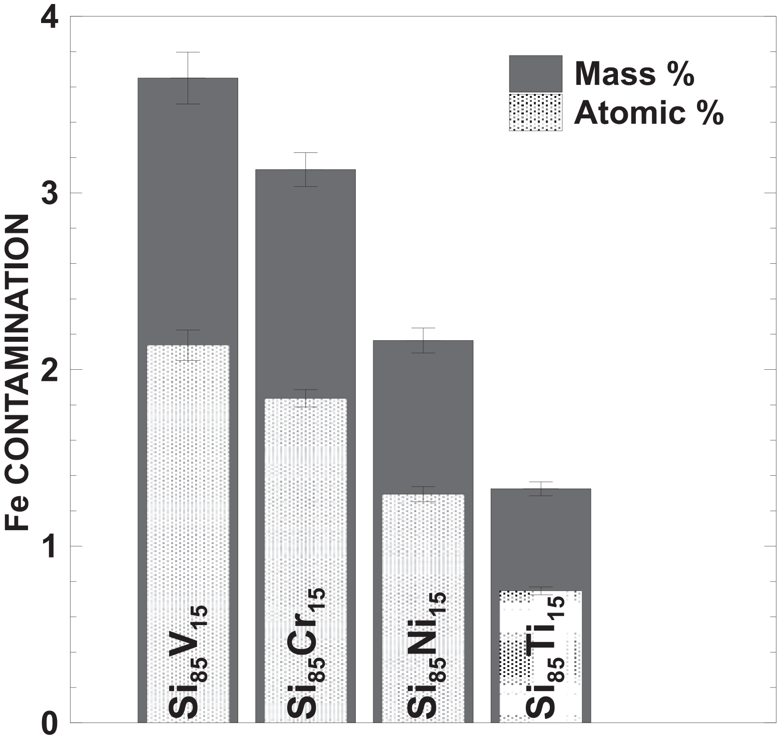

Figure 4.9 Quantified Fe contamination for a number of $TM_{15}Si_{85}$ alloys.

4.4 Conclusions

In this work a method for quantitative composition determination by Mössbauer spectroscopy of powder samples was developed. A response factor was determined, allowing for the calibration of Mössbauer spectral areas from one Fe containing species to another. Powder samples with IS were then formulated into Bellcore plastic films, resulting in homogeneous samples for Mössbauer measurement. Using this method, Fe contents as low as 0.201 at.% could be detected within an error of ±0.004 at.%.

Using this method, for the first time the amount of Fe contamination in ball milled Si was reported as a function of milling time. It was found that the amount of Fe increases and then reaches a steady state of 1.12 ± 0.04 at.% under the milling conditions used, the rate of Fe contamination roughly correlating with the Si grain size. These results are highly important for the development of practical Si-alloys for Li-ion batteries.

This method likely has many applications for the quantitative analysis of powder samples, especially where conventional ICP-OES is difficult, such as for carbons, boron nitride or other materials that are difficult to digest into solution. It should also be mentioned that while Fe-contents were measured in this study, the method should also be applicable to the quantitative detection of Sn or any other Mössbauer active element.

When ball milling Si, the addition of an inactive TM to the system was found to roughly double the Fe contamination as compared to Si precursor milled alone. Additionally, it was found that when the TM is Cr or V, Fe contamination continually increases with milling time and does not reach a plateau, highlighting the importance of determining a minimum milling time such that optimum performance of the resultant material is achieved with minimum Fe contamination.

By screening a number of Si-TM alloys, it was found that Fe contamination could be minimized by using Ti. When Ti was the TM used, Fe content was found to be considerably less than when any other TM was used at 1.33 ± wt. % Fe after 16 hours of high energy ball milling. These results are especially important for the development of practical Si-TM alloys for Li-ion batteries.

Chapter 5 **Outlook and Future Work**

5.1 Si-TM alloys

Presented in section 3.1.2.1, two phases appeared in the XRD pattern of $Si_{85}Fe_{15}$ in the initial stages of the mechanochemical reaction. These phases denoted a-FeSi and a-α-$FeSi_2$, shown in Figure 3.6, showed only a partial match to the reference diffraction patterns of either FeSi or α-$FeSi_2$; additionally, a Debye scattering calculation could not confirm the identity of either phase. The assumption was made that the crystal structure of these phases must, at the very least, be similar to the crystal structure of their crystalline counterparts. However, these may very well be completely new phases. These phases could potentially be identified using transmission electron microscopy and selected area electron diffraction (TEM-SAED). TEM-SAED is advantageous in that a single crystallite can be probed, generating an electron diffraction pattern. If a grain of either a-FeSi and a-α-$FeSi_2$ could be probed the electron diffraction pattern could potentially elucidate the crystal structure of that phase without the presence of the additional phases in the diffraction pattern. This, however, can be challenging as probing a single grain requires a single grain of the correct phase to be present and identifiable.

In Section 3.2.2 Cr was explored as a transition metal for Si-Cr alloy negative electrodes. It was found that given milling parameters that optimize impact frequency the mechanochemical reaction did not reach completion and some metallic Cr was present at every milling time. Because Cr is brittle, high frequency low impact collisions cannot exceed the yield strength of Cr, decreasing the efficiency of the mechanochemical reaction. By exploring milling parameters optimizing impact energy it is possible that a $Si_{85}Cr_{15}$

alloy with no metallic Cr could be generated. Exploring milling parameters that optimize impact energy could be as simple as using fewer milling balls of a larger diameter and increasing milling time. Additionally, by arc melting, a $Si_{85}Cr_{15}$ alloy could be generated with no metallic Cr present followed by a ball milling step to reduce grain size.

Based on the structural characterization and electrochemical analysis the conclusion was made that the presence of Cr in the electrode material catalyzes the decomposition of electrolyte, continuously generating SEI, increasing polarization and impedance. This result could be additionally confirmed by an electrolyte reactivity study.[106] Yan et. al showed that by blending inactive metallic powders that are commonly present in Li-ion batteries with a small quantity of graphite, binder, and conductive additive, the rate of electrolyte decomposition as a result of the metallic powder could be determined when cycled in a double half cells. The rate at which Cr catalyzes the reduction of electrolyte could then be quantified given a similar experiment.

In this thesis the research presented serves as a baseline for evaluating future Si-TM alloy materials. This is especially true in the case of Si-Fe alloys. Fe is inexpensive, abundant, and is therefore an ideal candidate for commercial Si-alloy negative electrodes. When evaluating Si-Fe alloys the best capacity retention and cycling performance was observed following 16 hours of milling; at this milling time irreversible capacity was large ~25%. Irreversible capacity is an important parameter to consider in full cell design, as the total quantity of lithium in the cell must be present in the positive electrode, and excess positive electrode is then required in order to balance the large irreversible capacity of the negative electrode therefore decreasing energy density.[23] This is especially challenging for Si-alloys generated by ball milling, as repeated collisions reduce particle sizes drastically increasing surface area[122]. Increases in surface area can be directly related to large initial irreversible capacities as decomposition of electrolyte forming SEI increases.

One method of decreasing surface area, therefore decreasing initial irreversible capacity, is carbon coating. By carbon coating the surface of the material, there is not only a decrease in electrolyte decomposition reactions, but a substantial decrease in surface area. Carbon coating by chemical vapor deposition requires heating the Si-alloy material to the decomposition temperature of ethylene gas ~1000 ºC at ambient pressure.[132] Heating Si-alloys to this temperature has a substantial impact microstructure. Ball milling is a successful processing technique as grain sizes are reduced forming a-Si, thereby preventing the pulverization of Si particles upon lithiation. High temperature treatment is counter productive in this respect as high temperatures promote grain growth and the formation of c-Si from a-Si. This is shown in Figure 5.1 where a $Si_{85}Fe_{15}$ alloy was heat treated for 8 hours at 800 ºC. The majority of a-Si is converted to c-Si and peak widths are considerably narrower. This ultimately leads to poor cycling performance of heat-treated Si-alloy electrodes. The poor thermal stability of $Si_{85}Fe_{15}$ alloys can be used as a baseline for the development of more thermally stable alloys, which could potentially maintain their microstructure following high temperature chemical vapor deposition; though at this point $Si_{85}Fe_{15}$ alloys are not an appropriate choice for carbon coating.

An alternative method of controlling initial irreversible capacity that does not require heat treatment is pre-lithiation. This is where some source of sacrificial lithium is added to the cell assembly either electrochemically, as an active reactant, as an electrolyte salt, or by placing the electrode in direct contact with Li-metal.[133] Though neither of these methods for controlling initial irreversible capacity were discussed in this work, it is important to note that before high Si content Si-alloy negative electrodes can be employed in commercial Li-ion cells, initial irreversible capacity must be addressed.

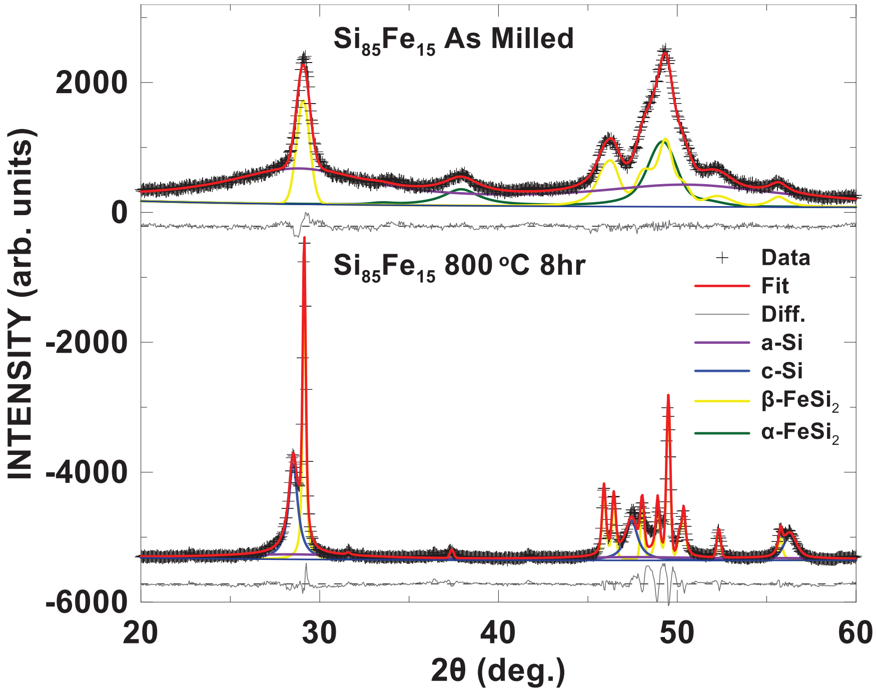

Figure 5.1 XRD comparison of ball milled $Si_{85}Fe_{15}$ alloy as milled and heat treated for 8 hours at 800 ºC.

Another important parameter in Si-alloy negative electrode design is CE. Average CE's reported here were ~99.4%. In a coin half-cell this is not a problem as the cell is flooded with electrolyte and contains a huge lithium reservoir in the form of the Li-metal counter/reference electrode. Therefore, parasitic reactions consuming electrolyte do not decrease half-cell capacity. In a full cell, however, there is a limited quantity of Li available and cell capacity is reduced as parasitic reactions occur. On a scale from 0% to 100%, a CE of 99.4% appears to be close to 100%; however, in a full cell format this corresponds to a 44.9% capacity fade over 100 cycles. Comparatively, using high precision coulometry, the CE of graphite in a coin cell was determined to be 99.93,[134] which over 100 cycles corresponds to a capacity fade of 6.7% in full cell format. Continuous SEI formation as a result of repeated expansion of Si particles upon lithiation leads to low CE. This problem has been addressed by using a pomegranate inspired Si-C core-shell nanostructures.[135] Si nano-particles are trapped within an amorphous carbon shell, with substantial void space to accommodate expansion and contraction, thereby preventing continuous SEI growth. The CE of this hierarchical nano-structured electrode was found to be 99.87%;[135] however, it was noted the cost associated with nano-Si must be reduced in order for core-shell nano-structures to become a commercially relevant Si negative electrode.[135] Though this was not addressed in this work, it is important to note that the low CE of Si-alloy negative electrodes must be addressed before high Si content Si-alloy negative electrodes can be implemented in commercial Li-ion cells.

Though substantial improvements in cycling performance have been shown in this work as compared to previous publications, this is entirely the result of using appropriate binders and electrolyte additives. An outlook on current challenges in developing Si-alloy negative electrodes was included to provide perspective. Though a high capacity electrode material with good capacity retention (>80% following 100 cycles) appears attractive, and implementation is seemingly facile, there remain several challenges that prevent the implementation of high Si content Si-alloy negative electrodes that must be addressed in future Si-alloy development.

5.2 Quantitative Composition Determination by Mössbauer Spectroscopy

By developing a method for quantitative composition determination by Mössbauer spectroscopy, for the first time, Fe contamination in ball milled Si and Si-alloys was quantified. Currently, this method is not suitable for high Fe content alloys and was therefore not used to quantify total Fe content in Si-Fe alloys. This was shown in section 4.3.1 proof of concept where increasing Fe content showed an exponential increase in error. Since error bars in Figure 4.3 c) are calculated according to the standard error from the quantification of 4 different sections of the same plastic film, this error is the result of non homogeneities in the film. The addition of slurry additives to increase viscosity could be explored to prevent separation of powders of differing densities as the film is being cast.

An additional method for decreasing error in high Fe content samples could be dilution. Graphitic carbon would make an excellent diluent as Fe contamination is typically low (ppm-ppb) in battery grade graphite, and the low atomic number of C would not contribute substantially to a decrease in count rates as a result on non-resonant mass absorption. An additional proof of concept would be required using a graphitic diluent to ensure that the presence of C in the plastic film slurry does not negatively impact the ability to form a homogenous slurry. Either method discussed here could be explored to enable the quantification of total Fe content when Fe content is >10% w/w.

The utility of this method can additionally be extended to any system made by ball milling where alternative means of quantifying Fe contamination are difficult. This is especially true for superalloys and metal matrix composite materials for powder metallurgy. Fe content of such materials, (e.g., Al/SiC composite powders) would be otherwise difficult to measure by ICP-OES. This method could additionally be applied to boron nitrides where acid digestion is difficult, and carbon where small sample quantities can limit the ability to quantify Fe content by ashing.

References

1. M. N. Obrovac, L. Christensen, D. B. Le, and J. R. Dahn: Alloy Design for Lithium-Ion Battery Anodes. *J. Electrochem. Soc.* **154**(9), A849 (2007).

2. M. N. Obrovac and L. Christensen: Structural Changes in Silicon Anodes during Lithium Insertion/Extraction. *Electrochem. Solid-State Lett.* **7**(5), A93 (2004).

3. L. Y. Beaulieu, T. D. Hatchard, A. Bonakdarpour, M. D. Fleischauer, and J. R. Dahn: Reaction of Li with Alloy Thin Films Studied by In Situ AFM. *J. Electrochem. Soc.* **150**(11), A1457 (2003).

4. M. T. McDowell, S. W. Lee, W. D. Nix, and Y. Cui: 25th anniversary article: Understanding the lithiation of silicon and other alloying anodes for lithium-ion batteries. *Adv. Mater.* **25**(36), 4966 (2013).

5. Agency for Natural Resources and Energy: Key World Energy statistics. *IEA Int. Energy Agency* (2017).

6. B. Dunn, B. Dunn, H. Kamath, and J. Tarascon: Electrical energy storage for the gridfor the Grid : A Battery of choices. *Sci. Mag.* **334**(6058), 928 (2011).

7. A. Sternberg and A. Bardow: Power-to-What? – Environmental assessment of energy storage systems. *Energy Environ. Sci.* **8**(2), 389 (2015).

8. D. Larcher and J. M. Tarascon: Towards greener and more sustainable batteries for electrical energy storage. *Nat. Chem.* **7**(1), 19 (2015).

9. M. Skyllas-Kazacos, M. H. Chakrabarti, S. A. Hajimolana, F. S. Mjalli, and M. Saleem: Progress in Flow Battery Research and Development. *J. Electrochem. Soc.* **158**(8), R55 (2011).

10. C. Liu, F. Li, L.-P. Ma, and H.-M. Cheng: Advanced Materials for Energy Storage. *Adv. Mater.* **22**(8), E28 (2010).

11. J. P. Deane, B. P. Ó Gallachóir, and E. J. McKeogh: Techno-economic review of existing and new pumped hydro energy storage plant. *Renew. Sustain. Energy Rev.* **14**(4), 1293 (2010).

12. J. Park: Principles and Applications of Lithium Secondary Batteries (Wiley, Weinheim, Germany, 2012).

13. T. Reddy: Linden's Handbook of Batteries, 4th ed. (McGraw-Hill Education, New York, 2010).

14. Y. Liang, C. Zhao, H. Yuan, Y. Chen, W. Zhang, J. Huang, D. Yu, Y. Liu, M. Titirici, Y. Chueh, H. Yu, and Q. Zhang: A review of rechargeable batteries for portable electronic devices. *InfoMat* **1**(1), 6 (2019).

15. City of Vancouver: (2018).

16. W. Kempton and J. Tomić: Vehicle-to-grid power fundamentals: Calculating capacity and net revenue. *J. Power Sources* **144**(1), 268 (2005).

17. W. Kempton and J. Tomić: *J. Power Sources* **144**, 280 (2005).

18. F. Mwasilu, J. J. Justo, E. K. Kim, T. D. Do, and J. W. Jung: Electric vehicles and smart grid interaction: A review on vehicle to grid and renewable energy sources integration. *Renew. Sustain. Energy Rev.* **34**, 501 (2014).

19. Emera Inc.: Annual Report (2017).

20. Statistics Canada: Nova Scotia (2017).

21. *Nova Scotia Power* (2017).

22. M. N. Obrovac: in *IUPAC 2017 Meeting / 46th World Chem. Congr.* (Sao Paulo, 2017).

23. M. N. Obrovac and V. L. Chevrier: Alloy negative electrodes for Li-ion batteries. *Chem. Rev.* **114**(23), 11444 (2014).

24. H. Kim, B. Park, H. J. Sohn, and T. Kang: Electrochemical characteristics of Mg-Ni alloys as anode materials for secondary Li batteries. *J. Power Sources* **90**(1), 59 (2000).

25. C. M. Park, Y. U. Kim, H. Kim, and H. J. Sohn: Enhancement of the rate capability and cyclability of an Mg-C composite electrode for Li secondary batteries. *J. Power Sources* **158**(2), 1451 (2006).

26. M. I. Purcell, T. D. Hatchard, R. J. Sanderson, and M. N. Obrovac: An Investigation of the C-Zn System as Lithium-Ion Battery Anode Materials. *J. Electrochem. Soc.* **161**(4), A643 (2014).

27. N. S. Hudak and D. L. Huber: Size Effects in the Electrochemical Alloying and Cycling of Electrodeposited Aluminum with Lithium. *J. Electrochem. Soc.* **159**(5), A688 (2012).

28. A. D. W. Todd, R. E. Mar, and J. R. Dahn: Tin–Transition Metal–Carbon Systems for Lithium-Ion Battery Negative Electrodes. *J. Electrochem. Soc.* **154**(6), A597 (2007).

29. M. N. Obrovac: in *Lecture Presented as Part of PHYC 5312, Adv. Batter. Fuel Cell, Supercapacitor Mater.* (Dalhousie University, 2017).

30. C. J. Wen and R. A. Huggins: Chemical diffusion in intermediate phases in the lithium-silicon system. *J. Solid State Chem.* **37**(3), 271 (1981).

31. P. Limthongkul: Electrochemically-driven solid-state amorphization in lithium-silicon alloys and implications for lithium storage. *Acta Mater.* **51**(4), 1103 (2003).

32. M. N. Obrovac and L. J. Krause: Reversible Cycling of Crystalline Silicon Powder. *J. Electrochem. Soc.* **154**(2), A103 (2007).

33. J. Li, A. Smith, R. J. Sanderson, T. D. Hatchard, R. A. Dunlap, and J. R. Dahn: In Situ ^{119}Sn Mössbauer Effect Study of the Reaction of Lithium with Si Using a Sn Probe. *J. Electrochem. Soc.* **156**(4), A283 (2009).

34. J. O. Besenhard, M. Hess, and P. Komenda: Dimensionally stable Li-alloy electrodes for secondary batteries. *Solid State Ionics* **40–41**(PART 2), 525 (1990).

35. J. O. Besenhard, P. Komenda, A. Paxinos, E. Wudy, and M. Josowicz: Binary and ternary Li-alloys as anode materials in rechargeable organic electrolyte Li-batteries. *Solid State Ionics* **18–19**, 823 (1986).

36. S. Komaba, N. Yabuuchi, T. Ozeki, Z. J. Han, K. Shimomura, H. Yui, Y. Katayama, and T. Miura: Comparative study of sodium polyacrylate and poly(vinylidene fluoride) as binders for high capacity Si-graphite composite negative electrodes in Li-ion batteries. *J. Phys. Chem. C* **116**(1), 1380 (2012).

37. K. Rhodes, N. Dudney, E. Lara-Curzio, and C. Daniel: Understanding the Degradation of Silicon Electrodes for Lithium-Ion Batteries Using Acoustic Emission. *J. Electrochem. Soc.* **157**(12), A1354 (2010).

38. A. M. Wilson and J. R. Dahn: Lithium Insertion in Carbons Containing Nanodispersed Silicon. *J. Electrochem. Soc.* **142**(2), 326 (1995).

39. M. Wachtler, M. R. Wagner, M. Schmied, and M. Winter: The effect of the binder morphology on the cycling stability of Li – alloy composite electrodes. *J. Electroanal. Chem.* **510**, 12 (2001).

40. S. Komaba, K. Shimomura, N. Yabuuchi, T. Ozeki, H. Yui, and K. Konno: Study on polymer binders for high-capacity SiO negative electrode of Li-Ion batteries. *J. Phys. Chem. C* **115**(27), 13487 (2011).

41. J. Li, D. B. Le, P. P. Ferguson, and J. R. Dahn: Lithium polyacrylate as a binder for tin-cobalt-carbon negative electrodes in lithium-ion batteries. *Electrochim. Acta* **55**(8), 2991 (2010).

42. A. Magasinski, B. Zdyrko, I. Kovalenko, B. Hertzberg, R. Burtovyy, C. F. Huebner, T. F. Fuller, I. Luzinov, and G. Yushin: Toward efficient binders for Li-ion battery Si-based anodes: Polyacrylic acid. *ACS Appl. Mater. Interfaces* **2**(11), 3004 (2010).

43. W.-R. Liu, M.-H. Yang, H.-C. Wu, S. M. Chiao, and N.-L. Wu: Enhanced Cycle Life of Si Anode for Li-Ion Batteries by Using Modified Elastomeric Binder. *Electrochem. Solid-State Lett.* **8**(2), A100 (2005).

44. B. Lestriez, S. Bahri, I. Sandu, L. Roué, and D. Guyomard: On the binding mechanism of CMC in Si negative electrodes for Li-ion batteries. *Electrochem. commun.* **9**(12), 2801 (2007).

45. N. S. Hochgatterer, M. R. Schweiger, S. Koller, P. R. Raimann, T. Wöhrle, C. Wurm, and M. Winter: Silicon/Graphite Composite Electrodes for High-Capacity Anodes: Influence of Binder Chemistry on Cycling Stability. *Electrochem. Solid-State Lett.* **11**(5), A76 (2008).

46. T. Li, Y. L. Cao, X. P. Ai, and H. X. Yang: Cycleable graphite/FeSi$_6$ alloy composite as a high capacity anode material for Li-ion batteries. *J. Power Sources* **184**(2), 473 (2008).

47. J. S. Bridel, T. Azaïs, M. Morcrette, J. M. Tarascon, and D. Larcher: Key parameters governing the reversibility of Si/carbon/CMC electrodes for Li-ion batteries. *Chem. Mater.* **22**(3), 1229 (2010).

48. J.-S. Bridel, T. Azaïs, M. Morcrette, J.-M. Tarascon, and D. Larcher: In Situ Observation and Long-Term Reactivity of Si/C/CMC Composites Electrodes for Li-Ion Batteries. *J. Electrochem. Soc.* **158**(6), A750 (2011).

49. M. Cerbelaud, B. Lestriez, D. Guyomard, A. Videcoq, and R. Ferrando: Brownian dynamics simulations of colloidal suspensions containing polymers as precursors of composite electrodes for lithium batteries. *Langmuir* **28**(29), 10713 (2012).

50. M. Winter and È. O. Besenhard: Electrochemical lithiation of tin and tin-based intermetallics and composites. *Electrochimica Acta* **45**(31) (1999).

51. N. Choi, K. H. Yew, H. Kim, S. Kim, and W. Choi: Surface layer formed on silicon thin-film electrode in lithium bis (oxalato) borate-based electrolyte. *J. Power Sources* **172**, 404 (2007).

52. Y. M. Lee, Y. Lee, H. Shim, K. Lee, and J. Park: SEI Layer Formation on Amorphous Si Thin Electrode during Precycling. *J. Electrochem. Soc.***154**(6), A515 (2007).

53. G. Han, M. Ryou, K. Young, Y. Min, and J. Park: Effect of succinic anhydride as an electrolyte additive on electrochemical characteristics of silicon thin-film electrode. *J. Power Sources* **195**(11), 3709 (2010).

54. K. W. Schroder, H. Celio, L. J. Webb, and K. J. Stevenson: Examining Solid Electrolyte Interphase Formation on Crystalline Silicon Electrodes: Influence of Electrochemical Preparation and Ambient Exposure Conditions. *J. Phys. Chem. C* **116**, 19737 (2012).

55. E. Markevich, K. Fridman, R. Sharabi, R. Elazari, G. Salitra, H. E. Gottlieb, G. Gershinsky, A. Garsuch, G. Semrau, M. A. Schmidt, and D. Aurbach: Amorphous Columnar Silicon Anodes for Advanced High Voltage Lithium Ion Full Cells : Dominant Factors Governing Cycling Performance. *J. Electrochem. Soc.* **160**(10), 1824 (2013).

56. V. Baranchugov, E. Markevich, E. Pollak, G. Salitra, and D. Aurbach: Amorphous silicon thin films as a high capacity anodes for Li-ion batteries in ionic liquid electrolytes. *Electrochem. Comm.* **9**, 796 (2007).

57. H. Nakai, T. Kubota, A. Kita, and A. Kawashima: Investigation of the Solid Electrolyte Interphase Formed by Fluoroethylene Carbonate on Si Electrodes. **158**(7), 798 (2011).

58. N. Choi, K. H. Yew, K. Y. Lee, M. Sung, H. Kim, and S. Kim: Effect of fluoroethylene carbonate additive on interfacial properties of silicon thin-film electrode. *J. Power Sources* **161**, 1254 (2006).

59. R. Elazari, G. Salitra, G. Gershinsky, A. Garsuch, A. Panchenko, and D. Aurbach: Li Ion Cells Comprising Lithiated Columnar Silicon Film Anodes , TiS_2 Cathodes and Fluoroethyene Carbonate (FEC) as a Critically Important Component. *J. Electrochem. Soc.* **159**(9), 1440 (2012).

60. M. Nie, D. P. Abraham, D. M. Seo, Y. Chen, A. Bose, and B. L. Lucht: Role of Solution Structure in Solid Electrolyte Interphase Formation on Graphite with $LiPF_6$ in Propylene Carbonate. *J. Phys. Chem. C* **117**, 25381 (2013).

61. I. A. Courtney and J. R. Dahn: Electrochemical and In Situ X-Ray Diffraction Studies of the Reaction of Lithium with Tin Oxide Composites. *J. Electrochem. Soc.* **144**(6), 2045 (1997).

62. T. D. Hatchard, J. M. Topple, M. D. Fleischauer, and J. R. Dahn: Electrochemical Performance of SiAlSn Films Prepared by Combinatorial Sputtering. *Electrochem. Solid-State Lett.* **6**(7), A129 (2003).

63. T. D. Hatchard, M. N. Obrovac, and J. R. Dahn: A Comparison of the Reactions of the SiSn, SiAg, and SiZn Binary Systems with L3i. *J. Electrochem. Soc.* **153**(2), A282 (2006).

64. J. Li and J. R. Dahn: An In Situ X-Ray Diffraction Study of the Reaction of Li with Crystalline Si. *J. Electrochem. Soc.* **154**(3), A156 (2007).

65. I. A. Courtney, W. R. Mckinnon, and J. R. Dahn: On the Aggregation of Tin in SnO Composite Glasses Caused by the Reversible Reaction with Lithium. *J. Electrochem. Soc.* **146**(1), 59 (1999).

66. V. L. Chevrier, L. Liu, D. B. Le, J. Lund, B. Molla, K. Reimer, L. J. Krause, L. D. Jensen, E. Figgemeier, and K. W. Eberman: Evaluating Si-Based Materials for Li-Ion Batteries in Commercially Relevant Negative Electrodes. *J. Electrochem. Soc.* **161**(5), A783 (2014).

67. Z. Du, R. A. Dunlap, and M. N. Obrovac: High Energy Density Calendered Si Alloy/Graphite Anodes. *J. Electrochem. Soc.* **161**(10), A1698 (2014).

68. V. A. Sethuraman, M. J. Chon, M. Shimshak, V. Srinivasan, and P. R. Guduru: In situ measurements of stress evolution in silicon thin films during electrochemical lithiation and delithiation. *J. Power Sources* **195**(15), 5062 (2010).

69. M. J. Chon, V. A. Sethuraman, A. McCormick, V. Srinivasan, and P. R. Guduru: Real-time measurement of stress and damage evolution during initial lithiation of crystalline silicon. *Phys. Rev. Lett.* **107**(4), 1 (2011).

70. L. MacEachern, R. A. Dunlap, and M. N. Obrovac: Mechanically Milled Fe-Si-Zn Alloys as Negative Electrodes for Li-Ion Batteries. *J. Electrochem. Soc.* **162**(12), A2319 (2015).

71. Z. Du, S. N. Ellis, R. A. Dunlap, and M. N. Obrovac: Ni_xSi_{1-x} Alloys Prepared by Mechanical Milling as Negative Electrode Materials for Lithium Ion Batteries. *J. Electrochem. Soc.* **163**(2), A13 (2016).

72. Z. Du, H. Liu, S. N. Ellis, R. A. Dunlap, M. Zhu, and M. N. Obrovac: Electrochemistry of Cu_xSi_{1-x} Alloys in Li Cells . *J. Electrochem. Soc.* **163**(7), A1275 (2016).

73. X. Zhao, R. J. Sanderson, M. A. Al-Maghrabi, R. A. Dunlap, and M. N. Obrovac: Electrochemistry of Sputtered and Ball Milled Si-Fe-O Alloys in Li Cells. *J. Electrochem. Soc.* **164**(6), A1165 (2017).

74. Y. Wang, S. Cao, M. Kalinina, L. Zheng, L. Li, M. Zhu, and M. N. Obrovac: Lithium Insertion in Nanostructured $Si_{1-x}Ti_x$ Alloys . *J. Electrochem. Soc.* **164**(13), A3006 (2017).

75. Y. Cao, B. Scott, R. A. Dunlap, J. Wang, and M. N. Obrovac: An Investigation of the Fe-Mn-Si System for Li-Ion Battery Negative Electrodes. *J. Electrochem. Soc.* **166**(2), A21 (2019).

76. Y. Liu, B. Scott, and M. N. Obrovac: Ball Milled Si-W Alloys: Part I. Microstructural and Phase Evolution during Ball Milling. *J. Electrochem. Soc.* **166**(6), A1170 (2019).

77. Y. Liu, J. C. Bennett, and M. N. Obrovac: Ball Milled Si-W Alloys: Part II. Thermal Behavior and Performance in Li Cells. *J. Electrochem. Soc.* **166**(13), A2791 (2019).

78. P. S. Gilman and J. S. Benjamin: Mechanical Alloying. *Ann. Rev. Mater. Sci* **13**, 279 (1983).

79. M. A. White: Physical Properties of Materials, 2nd ed. (CRC Press, Boca Raton, 2012).

80. D. L. Zhang: Processing of advanced materials using high-energy mechanical milling. *Prog. Mater. Sci.* **49**(3–4), 537 (2004).

81. T. D. Hatchard, A. Genkin, and M. N. Obrovac: Rapid mechanochemical synthesis of amorphous alloys. *AIP Adv.* **7**(4) (2017).

82. F. H. Allen, D. G. Watson, L. Brammer, A. G. Orpen, and R. Taylor: International Tables for Crystallography. Volume C: Mathematical Physical and Chemical Tables (1993).

83. S. Driscoll, M. Dowd, and P. D. Wentzell: Simulation of 1/fα noise for analytical measurements. *J. Chemom.* **Special Issue** 1 (2019).

84. J. L. Hoard: International Tables for X-Ray Crystallography. Volume III. Physical and Chemical Tables. *J. Am. Chem. Soc.* **85**(11), 1708 (1963).

85. P. Gütlich, E. Bill, and A. X. Trautwein: Mössbauer Spectroscopy and Transition Metal Chemistry (Springer, Berlin, Heidelberg, 2011).

86. J. W. Olesik: Elemental Analysis Using ICP-OES and ICP/MS. *Anal. Chem.* **63**(1), 12A (1991).

87. M. D. Fleischauer, J. M. Topple, and J. R. Dahn: Combinatorial Investigations of Si-M (M = Cr + Ni, Fe, Mn) Thin Film Negative Electrode Materials. *Electrochem. Solid-State Lett.* **8**(2), A137 (2005).

88. J. D. McGraw, M. D. Fleischauer, J. R. Dahn, and R. A. Dunlap: Mössbauer effect and X-ray diffraction investigation of Si-Fe thin films. *Philos. Mag.* **86**(32), 5017 (2006).

89. Z. Du, R. A. Dunlap, and M. N. Obrovac: Structural and Electrochemical Investigation of $Fe_{x}Si_{1-x}$ Thin Films in Li Cells. *J. Electrochem. Soc.* **163**(9), A2011 (2016).

90. H.-Y. Lee and S.-M. Lee: Graphite–FeSi alloy composites as anode materials for rechargeable lithium batteries. *J. Power Sources* **112**(2), 649 (2002).

91. H. Dong, X. P. Ai, and H. X. Yang: Carbon/Ba-Fe-Si alloy composite as high capacity anode materials for Li-ion batteries. *Electrochem. commun.* **5**(11), 952 (2003).

92. G. S. Collins, T. Kachnowski, N. Benczer-Koller, and M. Pasternak: Application of the Mossbauer effect to the characterization of an amorphous tin-oxide system. *Phys. Rev. B* **19**(3), 1369 (1979).

93. H. Yamane and T. Yamada: Effects of stacking fault on the diffraction intensities of β-FeSi2. *J. Alloys Compd.* **476**(1–2), 282 (2009).

94. B. E. Warren: X-RAY DIFFRACTION (Dover Publications, New York, 1990).

95. J. R. Dahn, I. A. Courtney, and O. Mao: Short-range Sn ordering and crystal structure of Li 4 . 4 Sn prepared by ambient temperature electrochemical methods. *Solid State Ionics* **111**, 289 (1998).

96. L. Y. Beaulieu, K. C. Hewitt, R. L. Turner, A. Bonakdarpour, A. A. Abdo, L. Christensen, K. W. Eberman, L. J. Krause, and J. R. Dahn: The Electrochemical Reaction of Li with Amorphous Si-Sn Alloys. *J. Electrochem. Soc.* **150**(2), A149 (2003).

97. E. P. Yelsukov and G. A. Dorofeev: Mechanical alloying in binary Fe-M (M = C, B, Al, Si, Ge, Sn) systems. *J. Mater. Sci.* **39**(16–17), 5071 (2004).

98. M. L. Trudeau and R. Schulz: High-resolution electron microscopy study of NiMo nanocrystals prepared by high-energy mechanical alloying. *Mater. Sci. Eng. A* **134**(C), 1361 (1991).

99. Z. Horita, D. J. Smith, M. Furukawa, M. Nemoto, R. Z. Valiev, and T. G. Langdon: Evolution of grain boundary structure in submicrometer-grained Al-Mg alloy. *Mater. Charact.* **37**(5), 285 (1996).

100. G. K. Wertheim, j. H. Wernick, and D. N. E. Buchanan: Mössbauer Effect in Co$_{1-x}$Fe$_{z}$Si. *J. Appl. Phys.* **37**(9), 3333 (1966).

101. J. Desimoni and F. H. Sánchez: Overview of the Mössbauer results obtained on silicon-rich iron silicide epitaxial phases on Si. *Hyperfine Interact.* **122**(3/4), 277 (1999).

102. I. Dézsi, C. Fetzer, L. Bujdosó, J. Brötz, and A. G. Balogh: Mechanical alloying of Fe – Si and milling of a- and B -FeSi2 bulk phases. **508**(1), 51 (2010).

103. E. A. Brandes, H. T. Greenway, and H. E. N. Stone: Ductility in Chromium. *Nature* **178**(4533), 587 (1956).

104. W. J. Weydanz, M. Wolfahrt-Mehrens, and R. A. Huggins: A room temperature study of the binary lithium – silicon and the ternary lithium – chromium – silicon system for use in rechargeable lithium batteries. *J. Power Sources* **81–82**, 237 (1999).

105. M. D. Fleischauer, J. M. Topple, and J. R. Dahn: Combinatorial Investigations of Si-M (M = Cr + Ni, Fe, Mn) Thin Film Negative Electrode Materials. *Electrochem. Solid-State Lett.* **8**(2), 137 (2005).

106. Z. Yan and M. N. Obrovac: Selecting inactive materials with low electrolyte reactivity for lithium-ion cells. *J. Power Sources* **397**, 374 (2018).

107. R. B. Ross: Metallic Materials Specification Handbook, 4th ed. (Springer US, Boston, MA, 1992).

108. L. D. Lafleur and C. Goodman: Characteristic Temperatures of the Mössbauer Fraction and Thermal-Shift Measurements in Iron and Iron Salts. *Phys. Rev. B* **4**(9), 2915 (1971).

109. D. J. Erickson, L. D. Roberts, J. W. Burton, and J. O. THomson: Precision Determinations of the Mössbauer Recoilless Fraction for Metallic Gold in the Temperature range 4.2=<T=<100 K. *Phys. Rev. B* **3**(7), 2180 (1971).

110. W. Keune: Lattice-dynamical study of SnTe by Mössbauer spectroscopy. *Phys. Rev. B* **10**(12), 5057 (1974).

111. I. Nowik, I. Jacob, and R. Moreh: Mössbauer study of crystallographic and magnetic phase transition, phonon softening, and hyperfine interactions in $Zr(Al_xFe_{1-x})_2$. *Phys. Rev. B* **47**(2), 723 (1993).

112. R. V. Pound and G. A. J. Rebka: Variation With Temperature of the Energy of Recoil-Free Gamma Rays From Solids. *Phys. Rev. Lett.* **4**(6), 274 (1961).

113. E. De Grave and R. Vochten: An ^{57}Fe Mössbauer Effect Study of Ankerite. *Phys. Chem. Miner.* **12**, 108 (1985).

114. E. De Grave and A. Van Alboom: Evaluation of ferrous and ferric Mössbauer fractions. *Phys. Chem. Miner.* **18**, 337 (1991).

115. S. G. Eeckhout and E. De Grave: Evaluation of ferrous and ferric Mössbauer fractions. Part II. *Phys. Chem. Miner.* **30**(3), 142 (2003).

116. M. Sorescu: A new method for direct determination of the recoilless fraction using a single room-temperature Mössbauer measurement of a two-foil absorber. *Mater. Lett.* **54**(4), 256 (2002).

117. M. Sorescu: Determination of the recoilless fraction in iron oxide nanoparticles using the two-lattice method. *J. Nanoparticle Res.* **4**(3), 221 (2002).

118. M. Sorescu: Evolution of the Mössbauer recoilless fraction during mechanochemical activation of iron oxides. *J. Mater. Sci. Lett.* **21**(22), 1759 (2002).

119. M. Sorescu: Structural effects on the recoilless fraction in iron silicides and borides. *Nucl. Instruments Methods Phys. Res. Sect. B Beam Interact. with Mater. Atoms* **275**, 16 (2012).

120. M. Allwes, M. Mekaoui, and M. Sorescu: Mutual solubility of scandium oxide-hematite magnetic nanocomposites : Mössbauer spectroscopy investigation. *Solid State Commun.* **261**(May), 46 (2017).

121. P. I. Arredondos, C. A. Barrero, K. E. Garcia, and J. M. Greneche: Enhancing the possibilities of 57Fe Mössbauer spectrometry to the study of chemical and physical properties of iron in medicines. *Polyhedron* **105**, 27 (2016).

122. C. Suryanarayana: Mechanical alloying and milling. *Prog. Mater. Sci.* **46**, 1 (2001).

123. J. De, A. M. Umarji, and K. Chattopadhyay: Origin of contamination and role of mechanochemistry during mechanical alloying: the case of Ag-Te alloys. *Mater. Sci. Eng. A* **448–451**, 1062 (2007).

124. F. E. Smith and E. A. Arsenault: Microwave-Assisted Sample Preparation in Analytical Chemistry. *Talanta* **43**, 1207 (1996).

125. R. Falciani, E. Novaro, M. Marchesini, and M. Gucciardi: Multi-element analysis of soil and sediment by ICP-MS after a microwave assisted digestion method. *J. Anal. At. Spectrom.* **15**(5), 561 (2000).

126. N. M. Hassan, P. E. Rasmussen, E. Dabek-Zlotorzynska, V. Celo, and H. Chen: Analysis of environmental samples using microwave-assisted acid digestion and inductively coupled plasma mass spectrometry: Maximizing total element recoveries. *Water. Air. Soil Pollut.* **178**(1–4), 323 (2007).

127. J.-M. Tarascon, A. S. Gozdz, C. Schmutz, F. Shokoohi, and P. C. Warren: Performance of Bellcore's plastic rechargeable Li-ion batteries. *Solid State Ionics* **86–88**(1), 49 (1996).

128. M. N. Richard: A Cell for In Situ X-Ray Diffraction Based on Coin Cell Hardware and Bellcore Plastic Electrode Technology. *J. Electrochem. Soc.* **144**(2), 554 (1997).

129. M. Gauthier, D. Mazouzi, D. Reyter, B. Lestriez, P. Moreau, D. Guyomard, and L. Roué: A low-cost and high performance ball-milled Si-based negative electrode for high-energy Li-ion batteries. *Energy Environ. Sci.* **6**(7), 2145 (2013).

130. G. M. Wang, S. J. Campbell, A. Calka, and W. A. Kaczmarek: Synthesis and structural evolution of tungsten carbide prepared by ball milling. *J. Mater. Sci.* **32**(6), 1461 (1997).

131. P. C. Norem and G. K. Wertheim: Mössbauer effect isomer shift of Fe57 in silicon and germanium. *J. Phys. Chem. So lids* **23**(8), 1111 (1962).

132. A. Becker and K. J. Hüttinger: Chemistry and kinetics of chemical vapor deposition of pyrocarbon - III pyrocarbon deposition from propylene and benzene in the low temperature regime. *Carbon N. Y.* **36**(3), 201 (1998).

133. F. Holtstiege, P. Bärmann, R. Nölle, M. Winter, and T. Placke: Pre-lithiation strategies for rechargeable energy storage technologies: Concepts, promises and challenges. *Batteries* **4**(1), 1 (2018).

134. A. J. Smith, J. C. Burns, S. Trussler, and J. R. Dahn: Precision measurements of the Coulombic efficiency of lithium-ion batteries and of electrode materials for lithium-ion batteries. *J. Electrochem. Soc.* **157**(2), 196 (2010).

135. N. Liu, Z. Lu, J. Zhao, M. T. Mcdowell, H. W. Lee, W. Zhao, and Y. Cui: A pomegranate-inspired nanoscale design for large-volume-change lithium battery anodes. *Nat. Nanotechnol.* **9**(3), 187 (2014).